ISSN 0915-633X

NATIONAL INSTITUTE FOR FUSION SCIENCE

Contributions to 31st European Physical Society Conference on
Plasma Physics
(London, UK, 28 June to 2 July, 2004) from NIFS

(Received - July 13, 2004)

NIFS-803 Aug. 2004

TOKI, JAPAN

Contributions to 31st European Physical Society Conference on Plasma Physics (London, UK, 28 June to 2 July, 2004) from NIFS

Abstract

18 contributed papers to the 31st European Physical Society Conference on Plasma Physics (London, UK, 28 June to 2 July, 2004) from the activities of NIFS and its collaborators are collected in this report.

Keywords : 31st European Physical Society Conference on Plasma Physics, NIFS, Large helical device, Compact helical system, contributed paper

Experimental Identification of Zonal Flows in CHS

A. Fujisawa, K. Itoh, H. Iguchi, K. Matsuoka, S. Okamura, A. Shimizu, T. Minami, Y. Yoshimura, K. Nagaoka, C. Takahashi, M. Kojima, H. Nakano, S. Ohshima, S. Nishimura, M. Isobe, C. Suzuki, T. Akiyama, K. Ida, K. Toi, [1]S.-I. Itoh and [2]P. H. Diamond

National Institute for Fusion Science, Oroshi-cho Toki, Japan

[1]RIAM, Kyushu University, Kasuga 816-8580 Japan

[2]University of California, San Diego, La Jolla, California, 92093-0319 USA

Zonal flow in toroidal plasmas is a band-like structure that has poloidal and toroidal symmetry (m=n=0) with a finite radial wavelength (k_r)[1,2]. The study of zonal flow is now becoming a central issue in both fusion research and plasma physics, since it is a mechanism that determines turbulent level and the resultant transport through nonlinear interaction of turbulence. A number of simulation works (e..g., [3,4]) have shown the existence of zonal flow and its important role in determination of the turbulence characteristics. On the other hand, only indirect signs of zonal flow have been obtained in several experiments [5,6]. This paper reports the first direct measurement of zonal flows in a toroidal plasma.

The experiments were performed in a toroidal helical device of medium size, Compact Helical System (CHS); major radius ~1 m, averaged minor radius ~0.2 m. In CHS, a heavy ion beam probe (HIBP) has been used to investigate physics of radial electric field, bifurcation and transport barrier [7]. Recently, another HIBP has been installed, and these double HIBP systems have begun to work to study plasma turbulence and spatio-temporal evolution of plasma structure.

Two HIBPs are located apart from each other approximately by 90 degrees in the toroidal direction. Each one is capable of measuring potentials, denoted as θ_1, θ_2 θ_3, at three adjacent positions (~1.5cm apart from each other) in the plasma. The potential difference between the neighboring channels, e.g., $\theta\theta_1=-\theta_1+\theta_2$, can represent a local electric field.

The first trials to identify the zonal flow are performed in electron cyclotron resonance heated (ECRH) plasmas [8]. The plasma parameters are; magnetic field strength B=0.88T, density n_e~$5x10^{12}cm^{-3}$, electron temperature T_e~1keV, ion temperature T_i~ 0.1keV, ion Larmor radius θ_i~0.1mm, and energy confinement time θ_E ~ 2-3 ms (or characteristic frequency of global confinement $\theta_E^{-1}/2\theta$ ~ 0.1 kHz).

Figure 1(a) shows spectra of the *electric field* fluctuation (or perpendicular flow to the magnetic field) at radial position of r_{obs}~12 cm (or θ~0.6) in the frequency of <30 kHz. The spectra are obtained with the Fast Fourier Transform (FFT) technique applied on the stationary period of ~ 80ms for the discharge duration of ~ 100ms; here the data sampling rate of 2 μs gives the Nyquist frequency of 250 kHz. The spectrum is an average of more than a dozen shots, and the result is significantly above the noise level. The *electric fields* between two toroidal location shows a high coherence (~0.6) in the region of low frequency (f<1 kHz). The phase difference between these two electric fields shows no difference if the observation points are on the same magnetic flux surface. Accordingly, the *electric field* in this range of frequency is the zonal flow.

A clear sharp peak at ~17kHz is found in electric field spectrum; the width of this mode is evaluated as ~0.5kHz with a Gaussian fitting. Figure 1(b) is the expanded view of the peak. A long-range correlation of the fluctuation at the frequency is also confirmed in potential that has a larger signal-to-noise ratio. This mode can be the Geodesic Acoustic

Mode (GAM). The definite conclusion is left in future. Figure 1(c) is the same power spectrum in linear scale as a function of the frequency normalized by ion Larmor frequency. Note that the essential characteristics of the spectrum are found to be very similar to those of simulation results in Ref. [4].

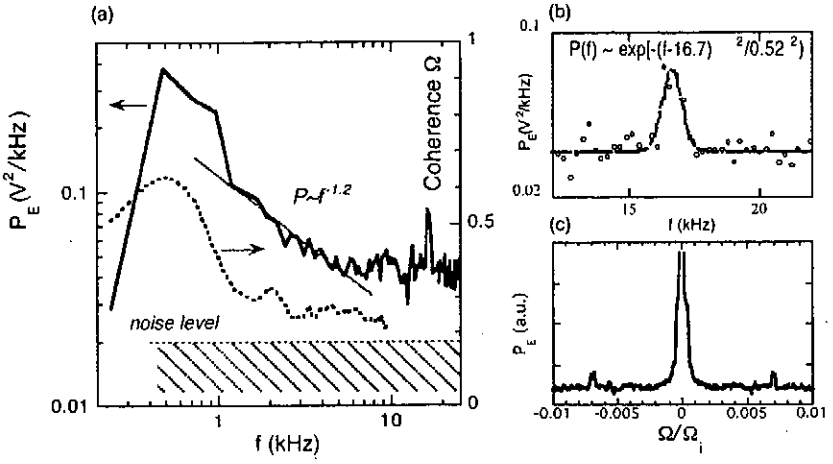

Figure 1: (a) Power spectrum and coherence of electric field fluctuation in CHS. (b) An expanded view of a peak around 17kHz, which is inferred as GAM. (c) The same spectrum in linear scale. The frequency is normalized by ion gyro-frequency.

The radial structure of the zonal electric field (or flow) is inferred by the phase difference between electric fields in two locations. The phase variation of zonal flow activity in radial direction can be evaluated by varying the observation position of the second HIBP, r_2, while fixing the observation point of the first HIBP. The FFT analysis of cross-power spectrum allows us to estimate the phase variation. The analysis demonstrates a radial structure changing sinusoidally with the wavelength of ~1.5 cm, that corresponds to ~$15\theta_i$. Our measurements clearly demonstrate both a long-range correlation and rapidly varying radial structure. Therefore, these studies identify the zonal flow for the first time.

Finally, zonal flows are ubiquitous in nature; the Jovian belts and zones, the

terrestrial atmospheric jet stream, the Venusian atmosphere and the solar tachocline. Now, the presence of zonal flows in toroidal plasmas is confirmed. This study of zonal flows in toroidal plasmas in a laboratory can give a new insight on the thermal evolution and structural formation in the universe.

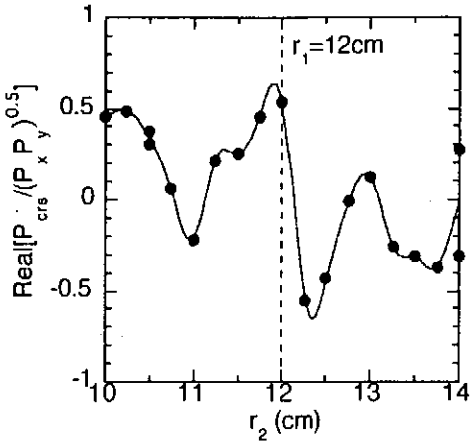

Figure 2. Phase difference of zonal flow in radial direction. The plotted points are the real part of the normalized cross power spectrum (θcosθ) between electric fields from the two HIBPs. In the measurements, the observation point of an HIBP is radially varied with the other fixed

Acknowledgements

This work is partially supported by Grant-in-Aids for Scientific Research (No. 15360497), and Specially Promoted Research (No. 16002005) of MEXT.

References

[1]A. Hasegawa, C. G. Maclennen, and Y. Kodama, Phys. Fluids **22**, 2122 (1979)

[2]P. H. Diamond, et al. in Proceedings of the 17th IAEA fusion energy conference, Yokohama,1998 vol. **4** 1421-1428. (International Atomic Energy Agency, Vienna, Austria, 1999).

[3] K. Hallatschek, Phys. Rev. Lett. 84, 5145 (2000).

[4] T S Hahm , K H Burrell, Z Lin, R Nazikian and E J Synakowski, Plasma Phys. Control. Fusion **42** (2000) A205.

[5] M. G. Shats, W. M. Solomon, Phys. Rev. Lett. **88**, 045001 (2002).

[6] G. R. McKee, et al., Plasma Phys. Control. Fusion **45**, A477 (2003).

[7] A. Fujisawa et al., Phys. Plasma **7** 4152 (2000)

[8] A. Fujisawa et al., submitted to Phys. Rev. Lett.

MHD Activities in high-β regime of LHD

S.Sakakibara[1], K.Y.Watanabe[1], H.Funaba[1], H.Yamada[1], Y.Narushima[1], T.Yamaguchi[2], S.Ohdachi[1], K.Narihara[1], I.Yamada[1], K.Tanaka[1], K.Kawahata[1], O.Kaneko[1], A.Komori[1], O.Motojima[1] and LHD Experimental Group[1]

1. National Institute for Fusion Science, Toki 509-5292, Japan
2. Graduate University for Advanced Studies, Hayama, Japan

1. Introduction

An understanding of MHD characteristics in high-β plasma is a main subject in toroidal devices for a realization of a fusion reactor. Net-current free plasmas in stellarator-heliotrons are free from current-driven instabilities unlike in tokamaks, and characterization of pressure-driven modes and control of them in the high-β regime are one of crucial issues towards for a helical fusion reactor. Since the heliotron configuration has a magnetic hill in the peripheral region, violation of stability of ideal and resistive interchange modes are concerned. With regard to the modes with the resonance in the core region, stabilization due to spontaneous generation of magnetic well has been verified in the experiment [1]. In contrast, theoretical prediction suggests that low-n mode such as $m/n = 1/1$ which has a resonance around $\rho = 0.9$ limits the pressure gradient in the peripheral region and consequently determines the beta limit [2]. In previous experiments in LHD, MHD modes excited in the peripheral region have been observed even in the low-β regime, and amplitudes of the modes such as m/n = 2/3 mode are considerably enhanced in the H-mode plasma with steep edge pressure gradient [3]. Since there are the several low-n rational surfaces in the peripheral region, activities of their resonant modes are a key issue for higher-β plasma production.

Since Large Helical Device (LHD) experiments were started in 1998, plasma parameters have been improved with progress of heating power systems during every experimental campaign. In recent experiments, the maximum averaged beta value $<\beta_{dia}>$ of 4 % was obtained by high power neutral beam heating of up to 12 MW in the configuration with R_{ax} = 3.6 m, B_t = 0.45 T and $n_e \sim 2.5 \times 10^{19}$ m^{-3}, where R_{ax} and B_t are magnetic axis position and toroidal magnetic field at R_{ax}, respectively. The $<\beta_{dia}>$ is the diamagnetic beta value defined as $4\mu_0/3 \cdot W_{dia}/(B_{av0}{}^2 V_{p0})$, where W_{dia} is the diamagnetic energy. The B_{av0} and V_{p0} are averaged toroidal magnetic field inside the plasma boundary and plasma volume,

respectively, and both of them are estimated under vacuum condition. This article presents MHD characteristics in the extended β regime.

2. Typical high-β discharge and MHD analysis

Figure 1 shows typical MHD activities in typical high-β discharge. The R_{ax} and Bt are set at 3.6 m and 0.5 T, respectively. The pitch parameter of helical coil γ is 1.22, which has high aspect ratio compared with the standard configuration with γ = 1.25. Three neutral beams are injected to this plasma and the deposition power is about 6.9 MW at 1.725 s. The m/n = 1/1, 2/3 and 2/5 modes excited in the edge region are dominantly observed in this discharge. The m/n = 1/1 and 2/3 modes grow from 0.7s and their amplitudes increase with $<\beta_{dia}>$. However, when $<\beta_{dia}>$ exceeds a certain value at 1 s, the m/n = 1/1 mode is frequently interrupted and the amplitude of m/n = 2/3 mode starts to decrease. Then $<\beta_{dia}>$ starts to increase suddenly, and the amplitude of the m/n = 2/5 mode increases after that. At 1.73 s, the degradation of $<\beta_{dia}>$ occurs with the growth of the m/n = 2/3 mode and the reduction of the m/n = 2/5 amplitude, although the heating and the supply of H_2 gas are still maintained. The equilibrium reconstruction and stability analysis are done for this discharge by 3-D MHD equilibrium code VMEC, and the result on m/n = 1/1 mode is shown in fig.1 as the example. While the pressure gradient around the m/n = 1/1 resonant surface increases with $<\beta_{dia}>$ and saturates at 1.1 s, the peaking

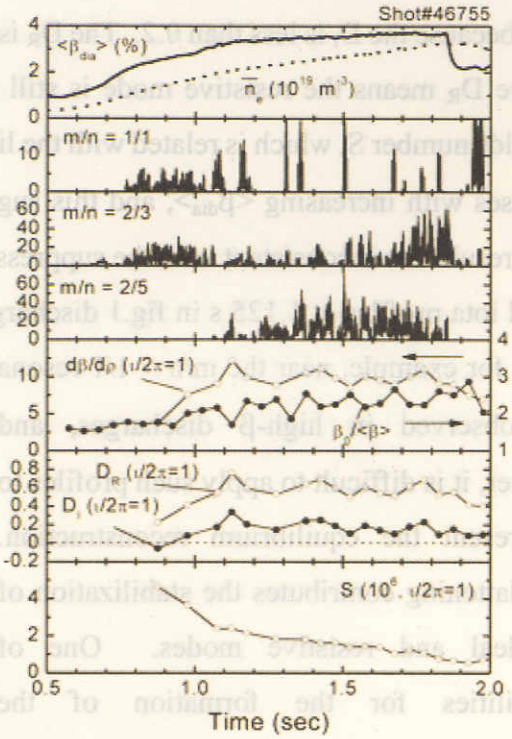

Figure 1 Temporal changes of plasma parameters in high-β discharge.

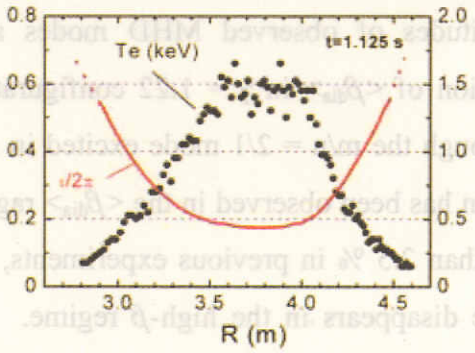

Figure 2 Te and iota profiles at 1.125 s in fig.1 discharge.

factor of pressure profile increases till one NBI is turned off. The Mercier parameter D_I, which is well used as the index of high-n ideal stability, indicates the mode is unstable because of the reduction of magnetic shear due to finite-β effect. The low-n ideal mode is expected to be stable because the D_I is less than 0.2. The D_R is the index of resistive interchange stability, and positive D_R means the resistive mode is still unstable during the discharge. The magnetic Reynolds number S, which is related with the linear growth rate of resistive interchange mode, decreases with increasing $<\beta_{dia}>$, and this suggests the rise of the growth rate of the mode. These results are inconsistent with the suppression of the m/n = 1/1 mode. Figure 2 shows the Te and iota profiles at 1.125 s in fig.1 discharge. The flattening structures of Te profiles are found, for example, near the m/n = 1/1 resonant surface. These asymmetrical structures are well observed in high-β discharges, and however, it is difficult to apply such profiles to the present the equilibrium reconstruction. This flattening contributes the stabilization of the ideal and resistive modes. One of possibilities for the formation of the asymmetrical profile in periphery is due to variation of magnetic surfaces due to finite-β effect such as the generation of the magnetic island.

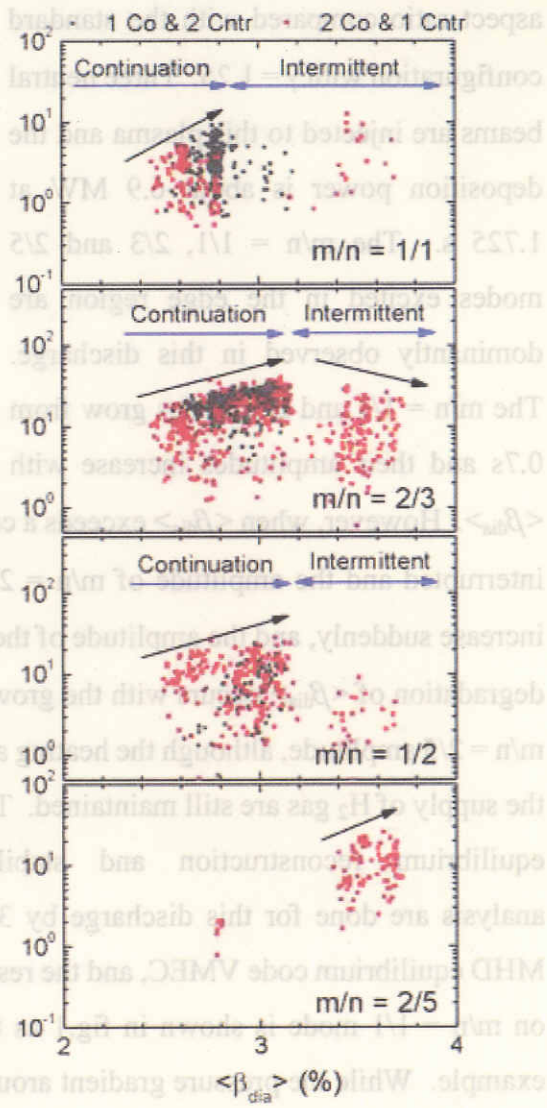

Figure 3 β dependence of MHD modes

2. β dependence of MHD modes and plasma shift due to finite-β effect

Figure 3 shows changes of the amplitudes of observed MHD modes as a function of $<\beta_{dia}>$ in γ = 1.22 configuration. Although the m/n = 2/1 mode excited in core region has been observed in the $<\beta_{dia}>$ rage of less than 2.5 % in previous experiments, this mode disappears in the high-β regime. The resonant surfaces with $\iota/2\pi \geq 1$ are located at $\rho \geq 0.9$ and their resonant modes are dominantly

observed in the $<\beta_{dia}>$ range with more than 2.5 %. While the amplitude of the m/n = 1/1 mode increases with $<\beta_{dia}>$, it disappears or is intermittently observed when $<\beta_{dia}>$ exceeds 2.8 %. Although the changes of the amplitudes of m/n = 2/3 and 1/2 modes are similar to the case of m/n = 1/1 mode, the threshold $<\beta_{dia}>$ where the mode disappears is higher. The m/n = 2/5 mode appears when $<\beta_{dia}>$ exceeds 3.4 %, the amplitudes still increase with $<\beta_{dia}>$ in the present $<\beta_{dia}>$ range. These phenomena suggest that the *stable* region is expanded from inner region to outer one. The destabilization of the MHD mode just outside the "*stable*" region may be caused by the steep pressure gradient outside the profile flattening as shown in fig.2.

The magnetic axis shift ΔR_{ax} identified by Te profile measured with Thomson scattering system is about 0.25 m at 1.725 s in fig.1 discharge, and this corresponds to $\Delta R/a \sim 0.25$. The statistical analyses indicate that this shift is smaller by about 50 % than the standard configuration with $\gamma = 1.25$. One of the reasons is that the rotational transform in $\gamma = 1.22$ is higher than the standard case, which leads to a restriction of Shafranov shift. Central rotational transforms in $\gamma = 1.22$ and $\gamma = 1.25$ in vacuum are 0.33 and 0.45, respectively. Although the reduction of the shift restricts the formation of magnetic well from the centre of plasma, it takes advantage from a viewpoint of beta-limit due to MHD equilibrium. Also, it contributes to prevent the reduction of the heat deposition of neutral beams because the direction of NBI is optimized to magnetic configuration with $R_{ax} = 3.6\sim3.7$ m. Therefore, the high-aspect-ratio configuration may be suitable for high-β plasma production from viewpoints of the power deposition. On the other hand, the variation of magnetic field structure may be an essential issue for the production of higher-β plasma rather than the R_{ax} shift itself from a viewpoint of equilibrium β-limit.

As a summary, several MHD modes in periphery are excited and spontaneously stabilized in turn when β increases, which may suggest an expansion of the MHD *stable* region of the plasma. The profile flattening has been observed in high-β regime, and it contributes the stabilization of MHD modes. The careful reconstruction of the equilibrium with applying asymmetrical profile is required for understanding of the mechanism of the mode stabilization.

References

[1] S.Sakakibara *et al.*, *Plasma Phys. Control Fusion* **44** (2002) A217.

[2] H.Yamada *et al.*, *Plasma Phys. Control Fusion* **44** (2002) A245.

[3] K.Toi *et al.*, *Nucl. Fusion* **44** (2004) 217.

Observation of DED–induced Magnetic Islands by a Tangentially Viewing Soft X–ray Camera on the TEXTOR Tokamak

S. Ohdachi[1], G. Fuchs, G. Bertschinger, K. H. Finken, K. Toi[1] and Textor Team

Institut für Plasmaphysik, Forschungszentrum Jülich GmbH,
EURATOM Association, D–52425 Jülich, Germany
[1] *National Institute for Fusion Science, Toki–shi 509–5292, Japan*

1 Introduction

Generation and evolution of the magnetic islands in magnetically confined plasmas attract wide interests. Magnetic islands play an important role in the confinement and stability of fusion plasmas. For example, the neo–classical tearing mode grows from seed islands, which are produced by small disturbances, and may limit the performance of tokamak plasmas. A tangentially viewing camera is suitable to study the dynamics of the magnetic islands. Since the magnetic islands extend toroidally along the magnetic field lines, they can be visualized better when they are observed tangentially. Thereby, we can study the evolution of structures of islands with higher spatial resolution.

A fast framing tangentially viewing soft X–ray camera system [1] used in Large Helical Device was installed on the TEXTOR-94 tokamak in the last experimental campaign. It can record soft X-ray (E > 1keV) images of the plasma with a framing rate of 4.5kHz (full–frame mode) and 13.5kHz (half–frame mode).

In this study, we describe a practical way to treat this kind of two-dimensional fluctuation data using singular value decomposition (SVD) . To investigate coherent modes, e.g. MHD instabilities, FFT based analysis acts as a tool that expands signals by trigonometric functions. The SVD method works similar, however, it uses an expansion to orthogonal but otherwise arbitrary functions. By SVD, a matrix A made up of n time series of m frames is decomposed into three matrices U, V and a diagonal matrix W such that $A = UWV^t$. The columns of U and V are spatial and temporal orthogonal vectors and are called Topos and Chronos, respectively. A time series $\boldsymbol{a}_i$ can be written by a combination of orthogonal components of the Topos and the Chronos type

$$\boldsymbol{a}_i = w_1 \times v_{i1} \times \boldsymbol{u}_1 + w_2 \times v_{i2} \times \boldsymbol{u}_2 + \cdots + w_m \times v_{im} \times \boldsymbol{u}_m. \tag{1}$$

Here, w_i^2 is a measure of the contribution from a particular component to the total fluctuation power. In practice, a few of the larger components suffice to describe the nature of the fluctuations, meaning that we may interpret the data using a small number of orthogonal components only.

To analyze two–dimensional line–integrated data, we might proceed as follows; first we perform tomographic reconstructions of the images, then we analyze the result with the SVD method. However, this requires much CPU power and noise is amplified by the inversion process. Therefore, we adopt another strategy; first we make a SVD analysis, then we do reconstruction to arrive at the result. As SVD and Radon transform are both linear operations, they commute and one can reconstruct the local pictures from the Topos only [2]. In the following section, we will perform the direct SV decomposition of the images. We will analyze the images obtained in 3/1 mode DED experiments on TEXTOR tokamak [3] in the section 3.

2 Tomographic reconstruction for tangentially viewing camera system

From one tangential view of the plasma, it is not possible to reconstruct a three-dimensional radiation profile. We assume that radiation along the magnetic field lines is constant and try to re-

construct a two-dimensional profile on a poloidal plane. A column vector $\boldsymbol{S}(S_i = 1, 2, \ldots, M)$ representing measured signals or Topos can be expressed as a linear combination of the radiation profile $\boldsymbol{E}$ $(E_i = 1, 2, \ldots, K)$ and the residual error vector $\boldsymbol{e}$, $\boldsymbol{S} = L\boldsymbol{E} + \boldsymbol{e}$.

The geometrical weight matrix L (M×K)) can be determined from integration along the line of sight (Fig. 1). We assume that the magnetic flux surfaces are circular and are shifted by $\Delta = \Delta_0(1-\rho^2)$, $(\rho = r/a)$ (Fig.1.(c)). Thereby all elements along a line of sight can be connected to elements in the reference poloidal plane (P2 in Fig. 1) by magnetic field lines(Red / Blue lines in Fig. 1). We assume the q–profile to be, $q(\rho) = \rho^2/(1-(1-\rho^2)^{(q_a+1)})\,q_a$. In this study, M ~ 2500 (effective channels looking at plasma within 64 ×64 pixels in the detector) and K = 1024 (poloidal cross section of the plasma is divided by 32 × 32). Since the reconstruction from the tangential view is an ill–posed problem, the least square solution of the equation is rather unstable; we need some smoothing mechanism or regularization. We make use of two methods. One is standard Fourier-Bessel (FB) expansion [4]. The radiation profile $\boldsymbol{E}$ is assumed to be in the form $\sum_{m=0}^{\infty}\sum_{l=0}^{\infty} a_{ml}\exp(im\theta)J_m(\lambda_m^l\rho)$. The coefficients a_{ml} will be determined by a least square fit. Here, J_m is the m th order Bessel function and λ_m^l is the l th zero–point of J_m. If we cut higher modes, this fitting will act as smoothing. The other method is Phillips-Tikhonov (PT) regularization[5, 6]. In this scheme, minimization of

$$Q = \gamma\sum|C\boldsymbol{E}|^2 + \frac{1}{M}\sum|\boldsymbol{S} - L\boldsymbol{E}|^2. \tag{2}$$

is considered rather than minimizing $\sum|\boldsymbol{S} - L\boldsymbol{E}|^2$ itself. The matrix C acts as Laplacian operator. The first term of the Eq. 2 decreases when the radiation profile is smoothed; parameter γ acts as the control parameter of the profile smoothness. After the matrix $C^{-1}L$ is SV decomposed as UWV^t,

$$\boldsymbol{E}(\gamma) = \sum_{j=1}^{p} w_j(\gamma)\frac{\boldsymbol{u}_j\cdot\boldsymbol{S}}{\sigma_j}(C^{-1}\boldsymbol{v}_j). \tag{3}$$

$\boldsymbol{E}$ is now written as combination of orthogonal patterns $C^{-1}\boldsymbol{v}_j$ (Fig. 2) with weighing factors $w_j(\gamma) = 1/(1 + M\gamma/\sigma_j^2)$. w_j is a decreasing function of j and the destabilizing effect from the small-scale structure (higher j components) is suppressed by proper choice of γ. Each of the schemes has its own merits and drawbacks. In BF expansion, radiation at the last closed flux surface is automatically set to zero. It is useful to avoid 'GHOSTS' near the plasma edge. With the PT method, we do not need to make assumptions about the shape of the flux surfaces; this will be useful when we want to analyze relaxation phenomena, e.g. sawteeth in tokamaks.

The reconstructions by both methods are shown in Fig. 3. Quite similar radiation profiles are obtained from the measurements. In FB inversion, poloidal mode $0 \le m \le 6$ and radial mode $0 \le l \le 9$ are included. In PT inversion, $\gamma = 1.0$ is used. In the references, the minimum of Akaike's Information Criterion (AIC) for FB and Generalized Cross Validation (GCV) for PT was used to determine the number of the free parameters. However, in our case, no clear minimum has been found. We took the point where the gradient of AIC / GCV starts to decrease as the number of the parameter increases.

3 DED experiments and the m=2 island structures

A dynamic ergodic divertor has been implemented on TEXTOR tokamak to control the heat fluxes in the edge region. The DED coil system is located on the high-field side of TEXTOR; external perturbation fields with poloidal / toroidal mode numbers m/n = 12/4, 6/2, 3/1 can be applied. When a co-rotating (1kHz) 3/1 perturbation field, which penetrates deeper into the plasma than a 12/4 field, is used, a rotating structure with the same frequency as the applied field is detected. Four SVD components are shown in Fig. 4. Obviously, the first Topo (A0) represents the global change of the whole

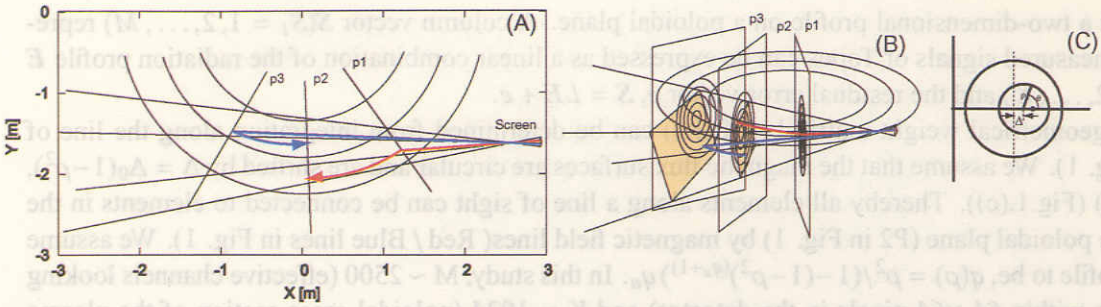

Fig.1: Geometry of the tangentially viewing camera system. On the equatorial plane (A) and the bird-view diagram (B) are shown. To project images on the plane (p2) we assume a magnetic flux shifted by $\Delta(\rho) = \Delta_0(1-\rho^2)$ shown in (C).

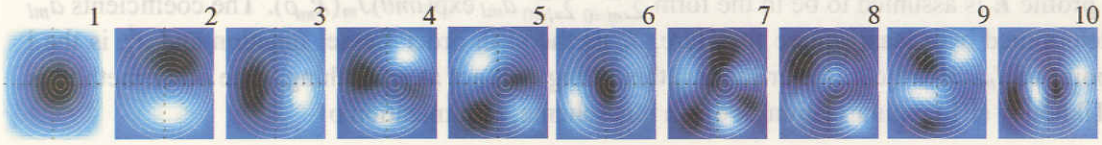

Fig.2: First ten orthogonal patterns of TP method in this geometry.

plasma shape. Choronos B2, B3 are synchronized with the external DED coil currents, the phases are different. For Topos A2, A3, we recognize that it is a rotation of the structure. Reconstructed images for B2, B3 are shown in C2, C3. There are m = 2 structures around $\rho \sim 0.5$ in both components and m = 3 structure around $\rho \sim 0.7$ can be seen in C3. The radial width of these structure is about 10 ~ 15 % of the minor radius. These rotating modes can be seen when the DED current exceeds a certain threshold. In some cases m = 2 structures remain after the DED current is terminated (cf [7]). The shape of these structures is similar to those during the external perturbation.

4 Conclusion

With SVD based analysis, we can effectively detect island-like structures in DED 3/1 mode experiments. Because the data of our diagnostics are incomplete in two aspects; outer part of the plasma cross section– mainly on the low field side– is not seen, and we have a 2–dimensional view only. The inversion is prone to errors, therefore, there is a need to compare with other diagnostics. We started this comparison, however, more detailed work will be needed

References

[1] S. Ohdachi *et al.*, Rev. Sci. Instrum **74**, (2003).

[2] G. Fuchs, Y. Miura, and M. Mori, Plasma Phys. Control. Fusion **36**, 307 (1994).

[3] K. H. Finken, Nucl. Fusion **37**, 583 (1997).

[4] Y. Nagayama, J. Appl. Phys. **62**, 2702 (1987).

[5] N. Terasaki, N. Iwama, and Y. Hosoda, The Transaction of the Institute of Electronics, Information and Communication Engineers D-II (in Japanese) **81**, 93 (1998).

[6] N. Iwama *et al.*, Appl. Phys. Lett. **54**, 502 (1989).

[7] Y. Liang, These proceeding .

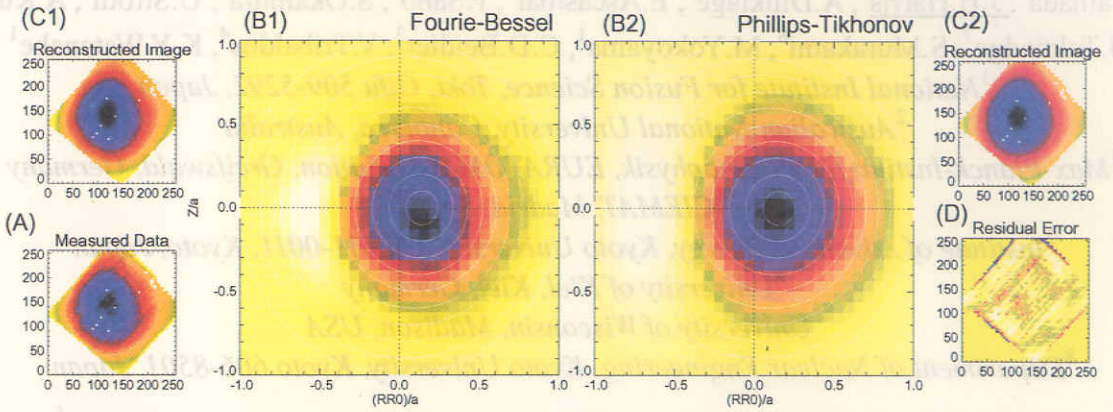

Fig.3: Tomographic reconstruction using two methods. (A) measured data. (B1) and (B2) reconstructed radiation profiles by FB and PT, respectively, (C1) and (C2) tangentially viewing image assuming radiation profile (B1) and (B2). (D) gives the residual error obtained by (A) and (C2).

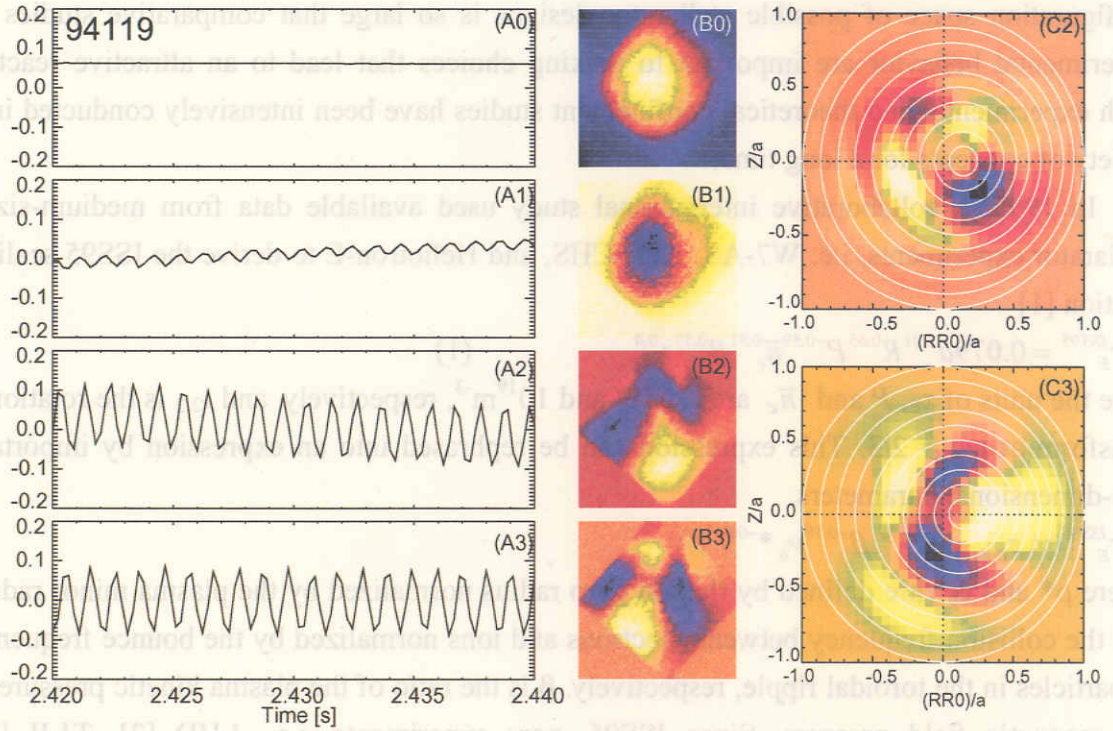

Fig.4: Choronos(A0-A3) and Topos(B0-B3) for the DED experiments. Tomographic reconstruction using FB expansion of (B2) and (B3) are also shown in (C2) and (C3), respectively.

Study on energy confinement time of net-current free toroidal plasmas based on extended international stellarator database

H.Yamada[1], J.H.Harris[2], A.Dinklage[3], E.Ascasibar[4], F.Sano[5], S.Okamura[1], U.Stroth[6], A.Kus[3], J.Talmadge[7], S.Murakami[8], M.Yokoyama[1], C.D.Beidler[3], V.Tribaldos[4], K.Y.Watanabe[1]

[1]*National Institute for Fusion Science, Toki, Gifu 509-5292, Japan*

[2]*Australian National University, Canberra, Australia*

[3]*Max-Planck-Institut für Plasmaphysik, EURATOM Association, Greifswald, Germany*

[4]*CIEMAT, Madrid, Spain*

[5]*Institute of Advanced Energy, Kyoto University, Uji 611-0011, Kyoto, Japan*

[6]*University of Kiel, Kiel, Germany*

[7]*University of Wisconsin, Madison, USA*

[8]*Department of Nuclear Engineering, Kyoto University, Kyoto 606-8501, Japan*

1. Introduction

Stellarators are widely recognized as the alternative to the tokamak as a toroidal fusion reactor. Large experiments have advanced parameters, and theoretical and design studies have developed advanced configurations for the next generation of experiments. The configuration space of possible stellarator designs is so large that comparative studies of experimental behavior are important to making choices that lead to an attractive reactor. Both experimental and theoretical confinement studies have been intensively conducted in a variety of concepts for a long time.

In 1995, a collaborative international study used available data from medium-sized stellarator experiments, i.e. W7-AS, ATF, CHS, and Heliotron-E to derive the ISS95 scaling relation [1]

$$\tau_E^{ISS95} = 0.079 a^{2.21} R^{0.65} P^{-0.59} \bar{n}_e^{0.51} B^{0.53} \iota_{2/3}^{0.4} \qquad (1)$$

Here the units of τ_E, P and $\bar{n}_e$ are s, MW and 10^{19}m^{-3}, respectively, and $\iota_{2/3}$ is the rotational transform at r/a = 2/3. This expression can be rephrased into an expression by important non-dimensional parameters,

$$\tau_E^{ISS95} \propto \tau_{Bohm} \rho^{*-0.71} \beta^{-0.16} \nu_b^{*-0.04},$$

where ρ^* and ν_b^* are defined by the ion gyro radius normalized by the plasma minor radius and the collision frequency between electrons and ions normalized by the bounce frequency of particles in the toroidal ripple, respectively. β is the ratio of the plasma kinetic pressure to the magnetic field pressure. Since ISS95, new experiments, i.e., LHD [2], TJ-II [3], Heliotron J [4], and HSX [5], most with different magnetic configurations, have started. Device improvement with divertor also has been taken into operation in W7-AS which has developed an improved confinement mode [6,7]. Extension of the confinement database aims at confirmation of our previous understanding of ISS95 and examination of possible new trends in confinement performance of stellarators. We have started to revise the international stellarator database incorporating these new data to improve assessment of a stellarator reactor and deepen understanding of the underlying physics of confinement.

2. Extension of International Stellarator Confinement Database

More than 2500 data have been compiled in the database to date and 1747 data representing typical discharges have been used for this study. The largest device, LHD (R/a = 3.9 m/ 0.6 m) has extended the parameter regime to substantially lower ρ^* and ν_b^* regimes which are 3-10× closer to the reactor regimes than those of the mid-size devices (Fig .1). Data from the flexible heliac TJ-II allows us to investigate the ι dependence over a much larger variation ($1.3 < \iota < 2.2$) than is available in the other experiments.

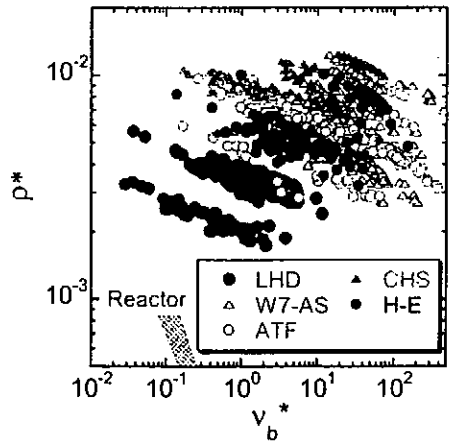

Fig.1. Parameter regime of data in the international stellarator database on the space of normalized gyro radii ρ^* and collisionality ν_b^*.

3. Towards a Unified Scaling

A simple regression analysis of the entire data set using the same parameters as in ISS95 yields

$$\tau_E^{REG} = 0.30 a^{2.07} R^{1.02} P^{-0.60} \bar{n}_e^{0.58} B^{1.08} \iota_{2/3}^{-0.16} \propto \tau_{Bohm} \rho^{*-1.95} \beta^{0.14} \nu_b^{*-0.18} \quad (2)$$

with root-mean-square error (RMSE) = 0.101. This expression is characterized by strong gyro-Bohm as a similar analysis of heliotron lines has suggested [8]. However, application of expression (1) to data from a single device leads to contradictory results. For example comparison of dimensionally-similar discharges in LHD indicates that the transport lies between Bohm and gyro-Bohm scalings [9]. Rotational transform scans in TJ-II also show that τ_E is proportional to the power of 0.35-0.6, which contradicts the weak ι dependence of Eq.2 [10].

We conclude that while Eq. 2 is useful for unified data description as a reference, its application is limited to the available data set alone and is not valid for extrapolation. Data inspection and experience from inter-machine studies suggest necessity to introduce a magnetic configuration dependent parameter in order to supplement the set of regression parameters and resolve this seemingly contradictory result. A systematic gap between W7-AS and heliotron/torsatrons was noted during the earlier studies on the ISS95 scaling. A recent example showing the pronounced effect of magnetic configuration

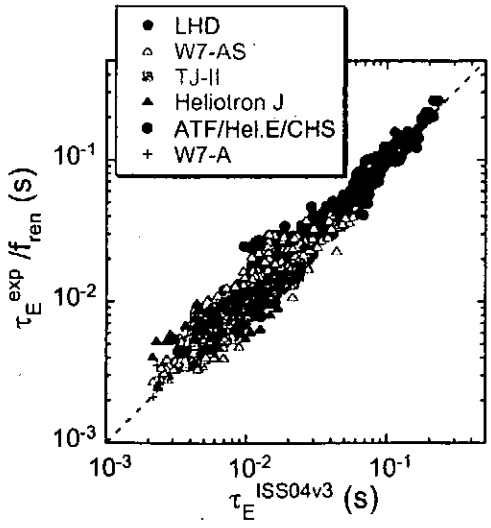

Fig.2. Comparison of energy confinement in experiments and predicted by ISS04v3. Experimental data is corrected by a renormalization factor f_{ren}.

variation even in a single device has come from comparison of the performance of configurations with shifted magnetic axes in LHD. A discharge with an inward shift of the magnetic axis from R_{ax}=3.9 m to R_{ax}=3.6 m, results in a doubling of τ_E for similar operational parameters a, P, $\bar{n}_e$, B and ι [9]. Therefore, acceptance of a systematic difference in different magnetic configurations is a prerequisite for derivation of a useful unified scaling law. A deterministic parameter characterizing the magnetic configuration has not been identified yet, but certainly involves the details of the helically corrugated magnetic fields, so an enhancement factor on ISS95 is used for renormalization to describe the magnetic configuration effect. One renormalization factor is defined by the averaged value of experimental enhancement factors for each configuration (subset). Iteration of a regression analysis of data normalized by these factors specific to configurations tends to converge into the following expression :

$$\tau_E^{ISS04v3} = 0.148 a^{2.33} R^{0.64} P^{-0.61} \bar{n}_e^{0.55} B^{0.85} \iota_{2/3}^{0.41} \propto \tau_{Bohm} \rho^{*-0.90} \beta^{-0.14} \nu_b^{*-0.01} \qquad (3)$$

with RMSE =0.026 (see Fig.2). In this process, weighting of the square root of the number of each subset is applied. This expression appears more comprehensive than Eq. 2. The leading coefficient is determined so as to give an renormalization factor of 1 for the case with ι<0.48 in W7-AS, and Fig. 3 shows the resultant renormalization factor for subsets f_{ren} with different configuration.

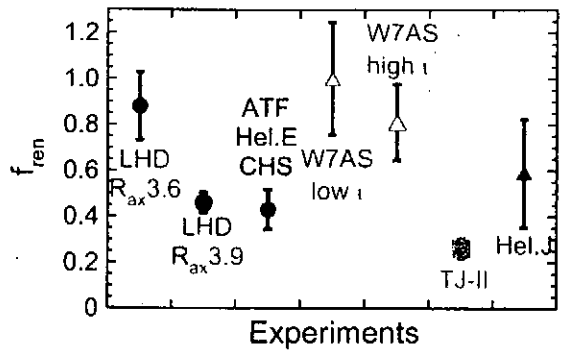

Fig.3. Renormalization factors for devices considered. Data of W7-AS are divided into two groups with low ι (<0.48) and high ι (≥0.48).

3. Discussions and Conclusions

The above mentioned results lead to a task for the immediate future of these studies. The first step is clarification of the hidden physical parameters to interpret the renormalization factor shown in Fig.3. It is reasonable to suppose that this renormalization factor is attributed to specific properties of the helical field structure of the devices. One possible leading parameter is an effective helical ripple, ε_{eff} [11] although there exist other potential configuration factors such as fractions of direct-loss orbits and trapped particles and the plateau factor, etc. The values of ε_{eff} have been calculated accurately by the numerical codes, DCOM [12], DKES[13] and MOCA[14]. Validation of results from the codes has been proven for several configurations. Figure 4 shows the correlation of ε_{eff} with the enhancement of confinement times with respect to the unified scaling law ISS04v3. The upper envelope resembles an $\varepsilon_{eff}^{-0.4}$ dependence, however, detailed studies on ε_{eff} behaviour are required as the data indicate, e.g. large scattering of W7-AS data. Also the expression of a power law of ε_{eff} diverges to infinity when it approaches zero. Hence, a simple power law

is expected to fail. Although all data in the database are not located in the collisionless regime where the neoclassical transport is enhanced, ε_{eff} can be related to effective heating efficiency through the neoclassical-like losses of high energetic particles and anomalous transport through flow dumping due to neoclassical viscosity. Due to the aforementioned reasons, an incorporation of that factor to a unified scaling is premature at present. Nonetheless, the correlation encourages a more systematic study of other potential configuration -dependent factors to project a path to the optimal configuration.

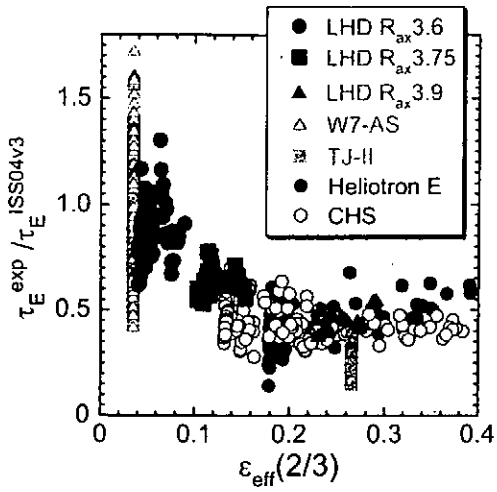

Fig.4 Confinement enhancement factor as a function of ε_{eff} at r/a=2/3.

The web page of the international stellarator confinement database is jointly hosted by National Institute for Fusion Science and Max-Planck-Institut für Plasmaphysik, EURATOM Association, and available at http://iscdb.nifs.ac.jp/ and http://www.ipp.mpg.de/ISS.

Acknowledgements

We are grateful to the LHD, W7-AS, TJ-II, and Heliotron-J experimental groups for their contribution to the international stellarator database. In particular, discussions and communications with Drs. R.Brakel, V.Dose, K.Ida, Y.Igithkhanov, H.Maassberg, D.Mikkelsen, Y.Nakamura, R.Preuss, F.Wagner, A.Weller and K.Yamazaki are appreciated. The activity of the international stellarator database is organized under the auspices of IEA Implementing Agreement for Cooperation in Development of the Stellarator Concept.

References

[1] U.Stroth et al, Nucl. Fusion **36** (1996) 1063.
[2] H.Yamada et al., Plasma Phys. Control. Fusion **43** (2001) A55.
[3] C.Alejaldre et al., Plasma Phys. Control. Fusion **41** (1999) A539.
[4] T.Obiki et al., Nucl. Fusion **41** (2001) 833.
[5] F.S.B.Anderson et al., Fusion Technol. **27** (1995) 273.
[6] K.McCormick et al., Phys. Rev. Lett. **89** (2002) 015001.
[7] A.Weller et al., Plasma Phys. Control. Fusion **45** (2003) A285.
[8] K.Yamazaki et al., in proc. 30th EPS Conf. on Contor. Fusion and Plasma Phys. (St.Petersburg, 7-11 July 2003) ECA Vol.27A, P-3.16.
[9] H.Yamada et al., Nucl. Fusion **41** (2001) 901.
[10] E.Ascasibar et al., to appear in Nucl. Fusion.
[11] C.D.Beidler and W.N.G.Hitchon, Plasma Phys. Control. Fusion **36** (1994) 317.
[12] S.Murakami et al., Nucl. Fusion **42** (2002) L19.
[13] W.I. van Rij, S.P.Hirshman, Phys. Fluids B **1** (1989) 563.
[14] V.Tribaldos, Phys. Plasmas **8** (2001) 1229.

Intermittent Fluctuation Property of Edge Plasmas in JT-60U and LHD

H. Miyoshi[1], N. Ohno[2], S. Takamura[1], V. P. Budaev[3], Y. Uesugi[4], N. Asakura[5], Y. Miura[5], S. Masuzaki[6], A. Komori[6]

1. Department of Energy Engineering and Science, Graduate School of Engineering, Nagoya University, Nagoya 464-8603, Japan
2. Eco Topia Science Institute, Nagoya University, Nagoya 464-8603, Japan
3. Nuclear Fusion Institute, RRC Kurchatov Institute, 123182, Kurchatov Sq.1, Moscow, Russia
4. Department of Electrical and Electronic Engineering, Graduate School of Engineering, Kanazawa University, Kanazawa 920-8667, Japan
5. Japan Atomic Energy Research Institute, Naka Fusion Research Establishment, Naka 311-0193, Japan
6. National Institute for Fusion Science, Toki 509-5292, Japan

1. Introduction

From experiment on fusion devices there is a lot of evidences that plasma turbulence is highly intermittent[1]. Intermittent events are well-known to play a crucial role in transport dynamics. Intermittent transport resulted from rare, large events is due to coherent structures, leading to losses above one predicted by neo-classical heat diffusive scaling. The cross-field transport in the scrape-off layer is directly related to the heat deposition width on the divertor target plate and the first wall, which is crucial to determine the averaged heat flux on it. Recently, intermittent convective plasma transport, so-called "blobs" has been observed in the edge plasmas of several fusion devices, which is thought to play a key role for cross-field plasma transport. Intermittent bursty fluctuations of ion saturation currents (I_{sat}) and/or floating potentials measured with probes are analyzed to obtain a basic property of the blobs[2]. Detailed comparison of the fluctuation properties in the edge plasmas of tokamak and helical fusion devices is expected to give an understanding of the blobby plasma transport, because the blobby plasma transport is thought to be strongly influenced by the magnetic configuration.

In this presentation, we will report the statistical analysis of the intermittent edge plasma fluctuations in the JT-60U tokamak and the Large Helical Device (LHD). The fluctuation property has been analyzed with probability distribution function (p.d.f.).

2. Analysis of edge fluctuation in ELMy H-mode plasma in JT-60U

Fig. 1 shows the plasma cross-section and locations of the reciprocating Mach probes installed at the high field side (HFS) baffle, low field side (LFS) mid-plane and just below the X-point in JT-60U. We have mainly analyzed the time evolution of the ion saturation

current I_{sat} with the Mach probe installed in the mid-plane at the low-field side and divertor probe array. The sampling time of I_{sat} is 5μs. Cross- and parallel- transports of the intermittent density bursts including ELM events are also discussed by comparing the spatiotemporal behaviour of the fluctuations in I_{sat}. Fig. 2 shows the typical time evolution of I_{sat} measured near the separatrix with the mid-plane reciprocating probe. Fluctuations of I_{sat} with intermittent bursts including ELM are observed. The measurement of I_{sat} with high time resolution reveals that one ELM is composed of many spikes. Fig. 3(a) shows radial profile of the peak amplitude of ELM defined as I_{sat} (ELM) in Fig. 2 as well as averaged I_{sat} between ELMs (I_{sat} (btw. ELM)). It is found that the peak amplitude of ELM decreases much slower than the averaged I_{sat} between ELMs. The effective radial decay length of I_{sat} (ELM) is estimated to 87mm which is about three times larger than 28 mm for I_{sat} (btw. ELM). This experimental result indicates that ELM can be convectively transported across the magnetic field much easier in comparison with bulk plasmas.

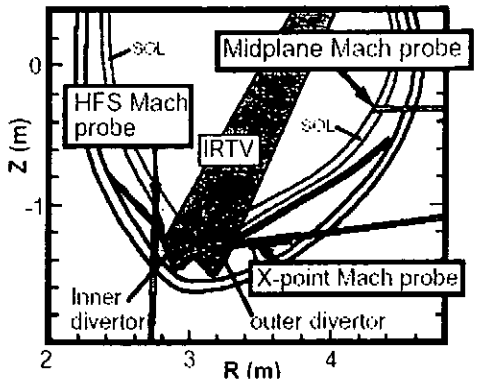

Fig 1. Plasma cross-section and location of reciprocating probe in JT-60U.

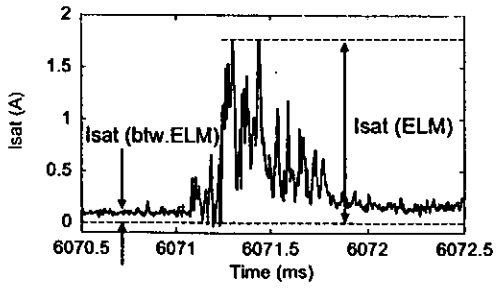

Fig 2. Typical time evolution of ion saturation currents measured with the mid-plane probe.

Next, we analyze fluctuation property of the time evolution of I_{sat} between ELMs based on probability distribution function (p.d.f.). The p.d.f. is an important statistical quantity for turbulence research. In order to obtain the p.d.f. function, we construct a histogram of the fluctuation signal. For fully random signal, the p.d.f. has a Gaussian profile. In edge plasmas of fusion devices, p.d.f.'s of density fluctuations are non-Gaussian and positively skewed, meaning that large positive fluctuations are much greater than expected values from fully random distributions. The fluctuations are sometimes negatively skewed. The deviation from the Gaussian distribution function can be characterized by flatness and skewness. The skewness $S=\langle x^3\rangle/\langle x^2\rangle^{3/2}$ describes the asymmetry of the p.d.f., and the flatness $F=\langle x^4\rangle/\langle x^2\rangle^2$ measures the tail's weight with respect to the core of the distribution, where

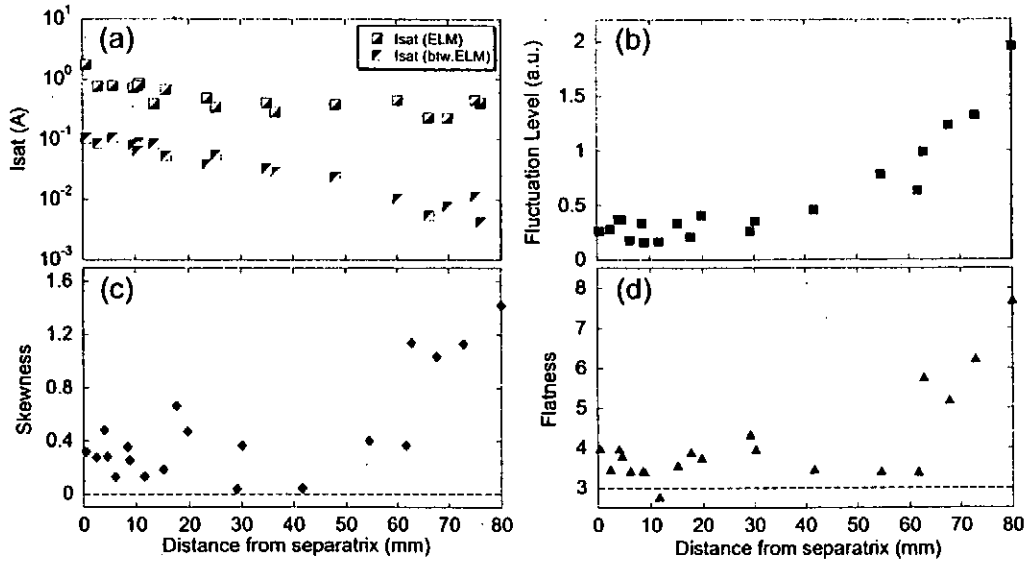

Fig 3. Radial profiles of (a):the peak amplitude of ELM and averaged ion saturation current of I_{sat} between ELMs, (b) normalized fluctuation level of I_{sat} between ELMs, (e)skewness and (f)flatness.

x is the deviation from averaged quality. In the Gaussian distribution function, the skewness and flatness are 0 and 3, respectively. Fig. 3(b) shows that the fluctuation level of I_{sat} between ELMs, corresponding to standard deviation of the p.d.f., is monotonically increasing with the distance from the separatrix d. On the other hand, the skewness and flatness also increase with d, deviating from 0 and 3 respectively. This means that the bursty positive spikes become dominant in the fluctuation of the I_{sat} at the positions near $d \sim 80$ mm, which could be related to the blobby plasma transport.

3. Fluctuation property in the edge plasma of LHD

Recent theory[3] predicts that the blobs propagate toward low field side in tokamaks because the blob motion is driven by charge separation in the scrape-off layer due to gradient B effect. On the other hand, in the LHD, the direction of the gradient in B is not uniform because the helical system has a complex magnetic configuration. Comparison between the intermittent bursty fluctuations in the edge plasma of tokamaks and helical devices makes it possible to understand the essential physics of the blob transport.

In the LHD, I_{sat} is measured by a Langmuir probe array (16 channels) embedded in the divertor plate, which is installed at inboard, outboard and bottom board. Fig. 4 shows the radial profiles of averaged I_{sat}, skewness and flatness. The averaged I_{sat} peaks near the probe

position of 40 mm, which corresponds to the striking point where magnetic line of force with long connection length are concentrated. On the other hand, it is found that large positive spikes of I_{sat}, characterized by large skewness and flatness, are strongly localized near the striking point (~55mm) on the divertor plate. Away from the probe position of 55mm, the skewness and flatness decrease. This tendency is completely different from the observation in the JT-60U. Moreover, it should be noted that the absolute values of the skewness and flatness are much higher than those in Fig. 3, which means that the p.d.f. of the I_{sat} fluctuation in the LHD strongly deviate from the Gaussian distribution in comparison with that of JT-60U. Careful observation of the I_{sat} at the probe position of 55mm shows that time evolution of I_{sat} are mainly composed of the spiky signals without the dc level. These fluctuation properties could be related to the complex magnetic structure in the edge region of the LHD.

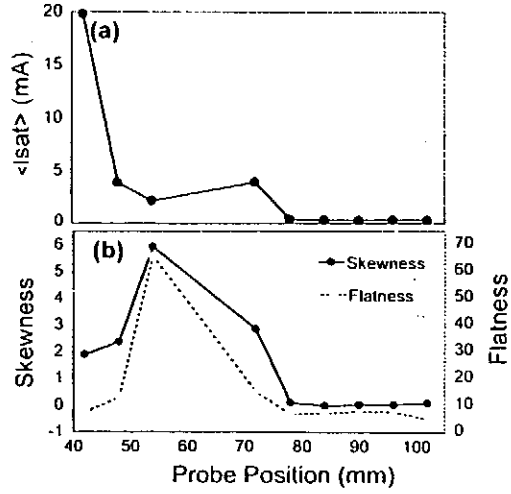

Fig 4. Radial Profiles of (a): averaged ion saturation current measured by the divertor probe array, (b): skewness and flatness.

4. Summary

The properties of the intermittent bursty fluctuation observed in the tokamak device JT-60U and helical device LHD have been investigated by p.d.f. analysis. In JT-60U, intermittent density fluctuations including ELMs are transported in radial direction. The fluctuation level, skewness and flatness of I_{sat} increase away from separatrix. On the other hand, in LHD, intermittent bursty signals are localized and skewness and flatness of I_{sat} are much larger than that of JT-60U.

References

[1] G. Y. Antar *et al.* Phys. Rev. Lett. **87**, 065001-1 (2001).

[2] J. A. Boedo, D. Rudakov *et al.* Phys. Plasmas, **8**, 4826 (2001).

[3] S. I. Krasheninnikov, Phys. Lett. A, **283**, 368 (2001).

[4] N. Asakura *et al.* Nucl. Fusion **44** (2004) 503-512

[5] S. Masuzaki *et al.* Nucl. Fusion **42** (2002) 750-758

A study of impurity transport in hydrogen and helium plasmas on LHD

H. Nozato[1], S. Morita[2], M. Goto[2], Y. Takase[1], A. Ejiri[1], T. Amano[3], K. Tanaka[2], S. Inagaki[2] and LHD Experimental Group[2]

1. Frontier Sciences, The University of Tokyo, Bunkyo-ku, Tokyo 113-0033, Japan

2. National Institute for Fusion Science, Toki, Gifu 509-5292, Japan

3. Goshikien 1-1706, Nisshin, Aichi 470-0105, Japan

I. Introduction

A combination of impurity pellet injection [1, 2] and spectroscopic method has been applied on the Large Helical Device (LHD) in order to understand the particle transport behavior in core plasmas. For this purpose, carbon pellets were injected into NBI-heated plasmas, and the transport coefficients D and V were inferred by a bremsstrahlung measurement with high-spatial resolution. The information on the impurity transport from the plasma center to the edge has been successfully obtained by the parallel arrays with 2×40 channels.

In hydrogen plasmas, the magnitude of spatially constant diffusion coefficient D is typically an order of magnitude larger than the neoclassical value, and dependences of the D on the impurity ion charge state and the electron density were weak. The inward convective velocity V of impurity ions, on the other hand, had strong dependences on both the impurity ion charge state and the electron density, of which the gradient was significant [3]. In this paper, the dependences of transport coefficients D and V on the charge state of bulk ions are compared in the collisional regime of hydrogen and helium plasmas on LHD.

II. Experimental Setup

The impurity pellet injector is installed for the purpose of direct deposition of impurity particles inside the last closed flux surface (LCFS) [4]. The impurity pellet is directed towards the plasma center on the equatorial plane from an outboard side of the torus. In order to investigate the behavior of injected carbon ions, the visible bremsstrahlung diagnostic using an interference filter and PMTs having high spatial (5cm) and temporal (0.1ms) resolutions was installed on LHD [5]. The filter has a central wavelength of λ=536.6nm and a full width at half maximum of 6.2nm. No strong emission line emitted near the wavelength region. As shown in Fig.1, the poloidal cross-section of LHD plasma is fully covered by 40 horizontal viewing chords of the bremsstrahlung diagnostic. As another diagnostic, a visible spectrometer with CCD detector is used to eliminate the contribution of emission lines at the same time. A single scan of the CCD frame requires 40ms interval. The contribution of emission lines to the PMT signal detected through the interference filter can be evaluated taking into account the spectrum recorded with the CCD.

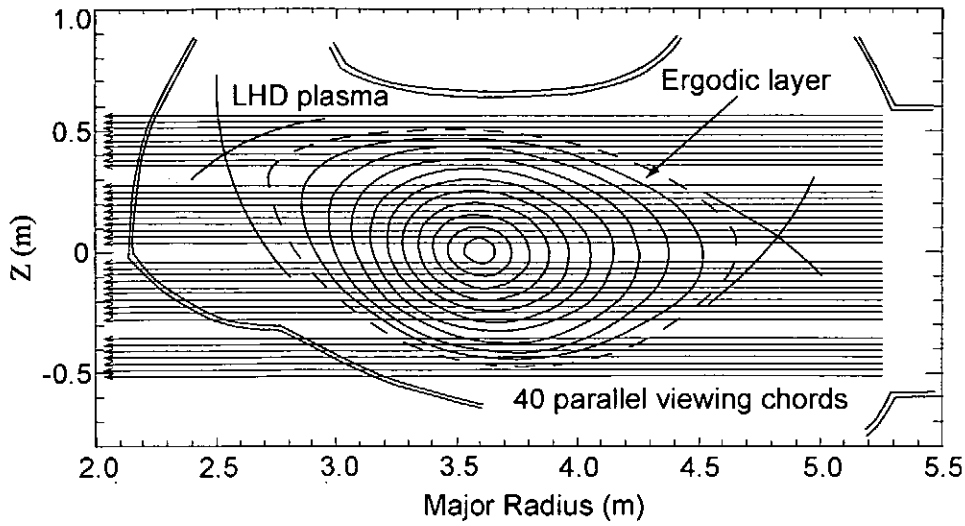

Fig. 1 Cross-sectional view of 40 chords per one poloidal section for the visible bremsstrahlung measurement and the configuration of LHD plasma with R_{ax}=3.6 (m).

III. Experimental Results

Cylindrical pure carbon pellets with (2.3-7.2)×10^{19} particles/pellet were injected into a steady phase of hydrogen and helium discharges with R_{ax}=3.6m. The plasmas are heated by NBI (P_{NBI}~7MW), and the carbon pellets are mostly ablated in the vicinity of ρ=0.65. Using a diffusive/convective model with a cylindrical approximation, the carbon transport was analyzed using one-dimensional impurity transport code [6] with a time step of 0.5ms. In the simulation, time evolutions of electron temperature were given by the data of ECE diagnostic. The transport coefficients D and V were determined by minimizing the total residual error between the measured and calculated intensities from z=-2.6 to z=-39.1cm. Here, it is assumed that the changes in electron density and effective charge profiles are brought only by the carbon ion transport with unchanged bulk ion transport. The analysis shows that, in hydrogen plasmas with R_{ax}=3.6m, the D have a spatially constant value and the inward V is required only in the region ρ>0.6 where electron density gradient exists. The same spatial structure of the transport coefficients in hydrogen plasmas was also adapted to the analysis for helium plasmas. Figure 2 shows the comparison of time evolutions between measured and calculated bremsstrahlung intensities in hydrogen and helium plasmas. The D and V were examined for various sizes of the injected carbon pellets in hydrogen plasmas. No difference in the obtained D and V was observed for different carbon pellet sizes. The density dependences of the inferred D and V at ρ=0.8 are summarized in Fig.3 for both discharges. Uncertainties of the obtained D and V are estimated to be 0.05m^2/s and 0.2m/s. It is found that the inward V in helium plasmas is lower than that in hydrogen plasmas by a factor of two, as seen in Fig.3 (b), whereas D is independent of the species of bulk ions (see Fig. 3(a)).

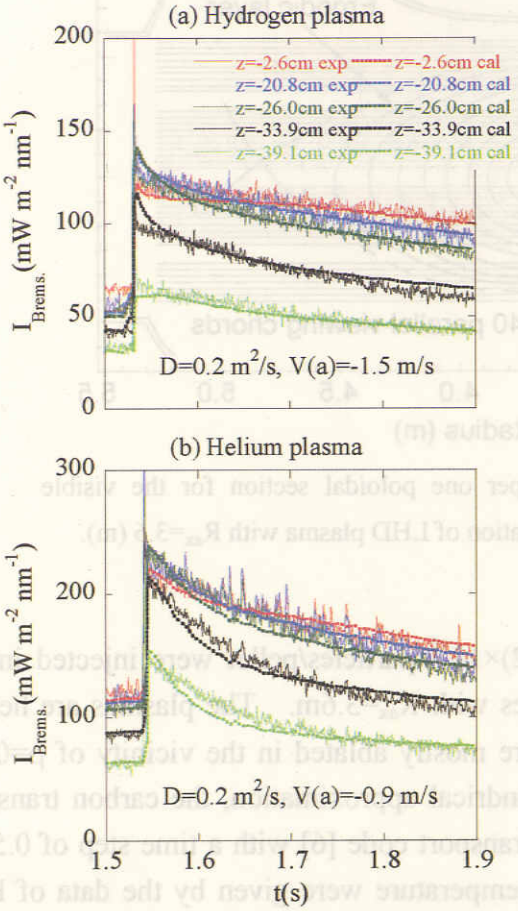

Fig. 2 Comparison of time evolutions between measured (solid lines) and calculated (dotted lines) bremsstrahlung intensities in (a) hydrogen and (b) helium plasmas.

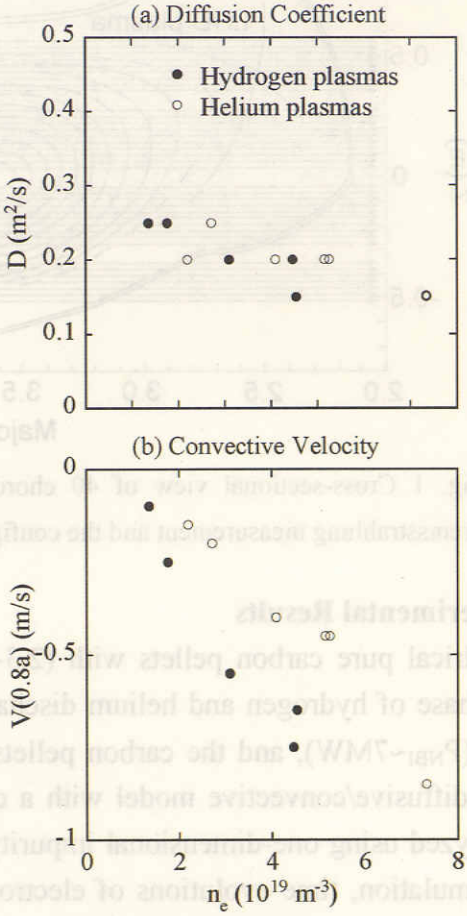

Fig. 3 Comparison of (a) diffusion coefficient and (b) inward velocity at ρ=0.8 as a function of line-averaged electron density in hydrogen (●) and helium plasmas (○).

VI. Discussions

According to neoclassical theory in collisional regime, the impurity ion flux Γ_{imp} is given by the following equation, if the impurity ion temperature gradient is negligible;

$$\Gamma_{imp} = -D_{imp}\frac{\partial n_{imp}}{\partial r} + n_{imp}V_{imp} = -D_{imp}\frac{\partial n_{imp}}{\partial r} + \frac{D_{imp}}{T_{imp}}\left(\frac{q_{imp}n_{imp}}{q_i n_i}\right)\frac{\partial p_i}{\partial r}, \quad (1)$$

where n, q and p stand for the density, charge state and pressure, respectively. The subscript *imp* and *i* denote impurity and bulk ions. Furthermore, although the inward flux (V<0) in the impurity ion flux is expected to be driven by the bulk ion density gradient, the bulk ion temperature gradient term contributes to the outward flux (V>0). Then, the inward flux of impurity ions can be replaced as follows [7];

$$V_{imp} = D_{imp}\left(\frac{q_{imp}}{q_i n_i}\right)\frac{\partial n_i}{\partial r}. \qquad (2)$$

The Eq. (2) indicates that the inward flux is appeared by the density gradient of bulk ions. If the $n_i(r)$ is reflected by $n_e(r)$, the inferred spatial structure of the inward V shows a good agreement with the bulk ion profile, as shown in Fig. 4(a). Figure 4(b) shows the relation between the inward V and the electron density gradient at ρ=0.8 in hydrogen plasmas. It is clearly seen that the inward V is a strong function of the $\partial n_e/\partial r$.

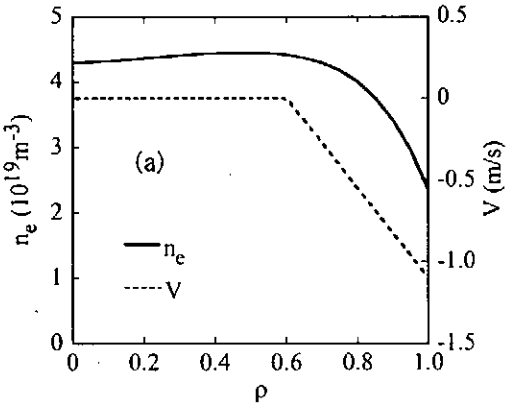

Fig. 4(a) Spatial structure of inward V and electron density profile in typical hydrogen plasma.

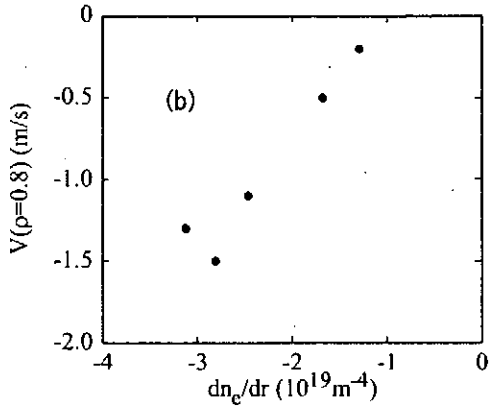

Fig. 4(b) Relation between inward V and electron density gradient at ρ=0.8 in hydrogen plasmas.

The Eq. (2) also suggests that the inward flux is inversely proportional to the charge state of bulk ions q_i. Seeing the present results in Fig.3 (b), the inward V in helium plasmas has roughly a half value of hydrogen plasmas. The difference of the inward V between both plasmas can be possibly explained by the neoclassical effect.

References

[1] Y. Shirai, S. Morita, M. Goto *et al.*, J. Plasma Fusion Res. **1**, 302 (1998).

[2] S. Morita, Y.Shirai, M.Goto *et al.*, Nucl. Fusion **42**, 876 (2002).

[3] H. Nozato, S. Morita, M. Goto *et al.*, Phys. Plasmas **11**, 1920 (2004).

[4] H. Nozato, S. Morita, M. Goto *et al.*, Rev. Sci. Instrum. **74**, 2032 (2003).

[5] H. Nozato, S. Morita, M. Goto *et al.*, J. Plasma Fusion Res. **5**, 442 (2002).

[6] T. Amano, J. Mizuno and J. Kako, Int. Rep. IPPJ-616, Institute of Plasma Physics, Nagoya University (1982).

[7] K. Miyamoto, "*Plasma physics for nuclear fusion*", MIT Press, Cambridge, Mass. (1976).

Characteristics of H-mode-like discharges in LHD under the presence of 1/1 rational surface at ergodic layer

S.Morita[1], T.Morisaki[1], K.Tanaka[1], M.Goto[1], S.Masuzaki[1], S.Sakakibara[1], S.Inagaki[1], Y.Nagayama[1], K.Narihara[1], H.Nozato[2], M.Osakabe[1], R.Sakamoto[1], K.Toi[1], T.Tokuzawa[1] and LHD experimental group

1. National Institute for Fusion Science, Toki 509-5292, Gifu, Japan
2. Science and Technology Center for Atoms, Molecules and Ions Control, Osaka University, Osaka 565-0871, Japan

1. Introduction

The plasma behavior is affected by the rational surface existing at the plasma boundary. H-mode-like discharge is one of the typical examples. In W7-AS [1] the H-mode-like discharge was obtained only when the major rational surface was produced at the plasma boundary in net-current-free ECH plasmas. In CHS [2,3] a similar discharge was also obtained by additionally introduced ohmic current in NBI plasmas, which changed an edge rotational transform, $\iota(a)/2\pi$. Recently, the H-mode-like discharges have been successively obtained in CHS NBI plasmas [4] and Heliotron-J ECH plasmas [5] by varying the $\iota/2\pi(a)$ values without externally induced plasma current.

In LHD, on the other hand, an H-mode-like discharge appeared in high-β plasmas (β~2%) with a low magnetic field (B_t<0.75T) at R_{ax}=3.60m ($\iota/2\pi(a)$=1.56) [6]. The growth of m/n=2/3 modes appeared at the edge barrier region with the saturation of plasma performance. Recently, an H-mode-like discharge has been newly obtained in a full B_t field (B_t=2.5T) by shifting the R_{ax} outwardly (R_{ax}=4.00m) [7]. In this paper characteristics of the H-mode-like discharges are briefly reported.

2. Edge rotational transform and connection length of magnetic field

Edge rotational transform at ρ=1 and averaged plasma minor radius in LHD are plotted in Fig.1 (a) and (b) as a function of magnetic axis position, R_{ax}. The edge rotational transform ranges in $0.7< \iota/2\pi(a) <1.6$. The 1/1 surface is located at ρ=0.88 in a standard vacuum configuration of R_{ax}=3.60m and located at ρ=1.0 near R_{ax}=3.90m. The plasma size becomes small, but the thickness of ergidic layer surrounding the core plasma becomes large when the R_{ax} is shifted outwardly.

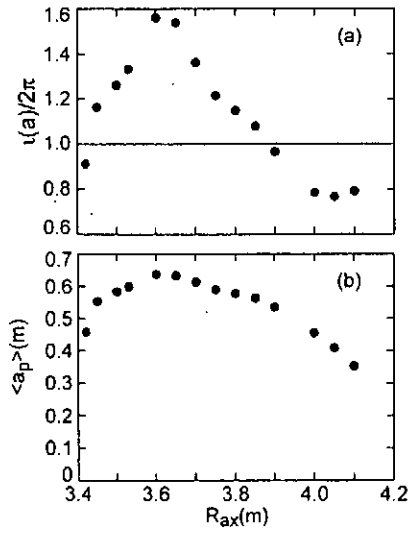

Fig.1 Edge rotational transform (a) and averaged plasma radius (b) as a function of magnetic axis, R_{ax}.

Figure 2 shows edge radial profiles of magnetic field connection length, L_c, and $\iota/2\pi$ at a horizontally elongated position in R_{ax}=3.90, 4.00 and 4.10m. It is seen that the thickness of the ergodic layer becomes

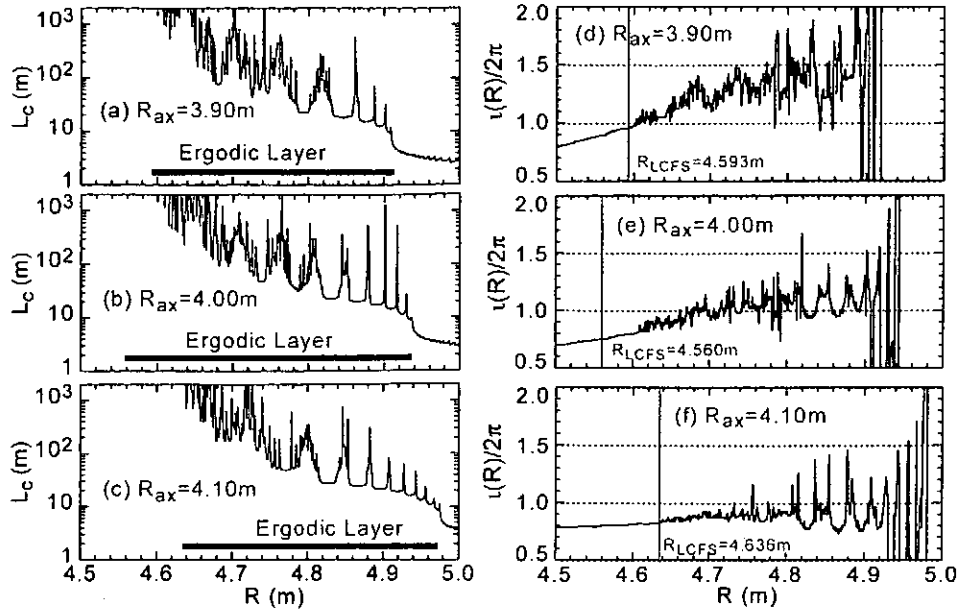

Fig.2 Edge radial profiles of magnetic field connection length ((a) R_{ax}=3.90m, (b) 4.00m, (c) 4.10m) and rotational transform ((d) R_{ax}=3.90m, (e) 4.00m, (f) 4.10m). The positions of LCFS are indicated with vertical solid lines.

large at the X-point and closes to 40cm. The X-point exists at the outside of LCFS in the figure. Real outside boundary of the plasmas is determined by the competition between heat input and heat loss inside the ergodic layer, although it is, of course, a strong function of the connection length. The positions of the 1/1 surface in R_{ax}=3.90 and 4.00m are located near the LCFS and outside of ergodic layer, respectively. No 1/1 surface exists substantially in R_{ax}=4.10m. Thus, it is understood that the pressure gradient of the 1/1 surface is very sensitive to the heat flux in the case of R_{ax}=4.00m.

In LHD, at present, the LCFS positions indicated in the figure are defined by the outermost flux surface on which the deviation of the magnetic field line is less than 4mm while it travels 100 turns along the torus [8]. Then, the position of the LCFS is affected considerably by the presence of small islands near LCFS, as did appear in the case of R_{ax}=4.00m. The distance between the 1/1 rational surface and the LCFS defined in this manner is about 12cm at the horizontally elongated plasma position in the case of R_{ax}=4.00m.

3. H-mode-like discharges

Experimental trials have been made regarding such three configurations. As a result, the H-mode-like transition was appeared in R_{ax}=4.00m by changing the NBI input power while maintaining a relatively high density. No transition was obtained in R_{ax}=3.90 and 4.10m. This result strongly suggests the importance of the 1/1 surface at the plasma edge for the H-mode-like discharge.

A typical waveform is shown in Fig.3. One of three NBIs is turned off at t=1.25s. After turning off the beam line, the Hα emission quickly drops and the density gradually rises, showing a clear turning point. ELM-like bursts appear in the Hα signal. Similar bursts are

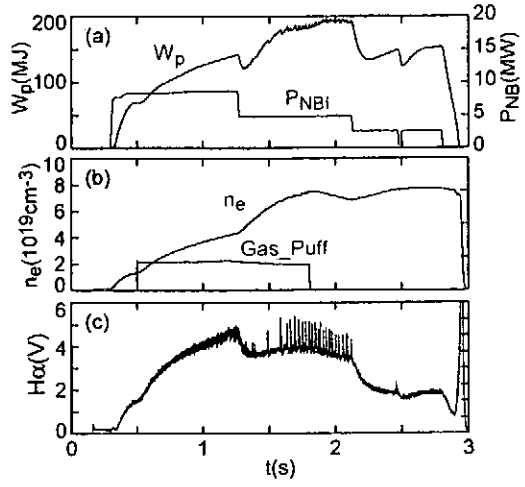

Fig.3 H-mode-like discharge after P_{NBI} decrease; (a) W_p, (b) n_e (c) Hα.

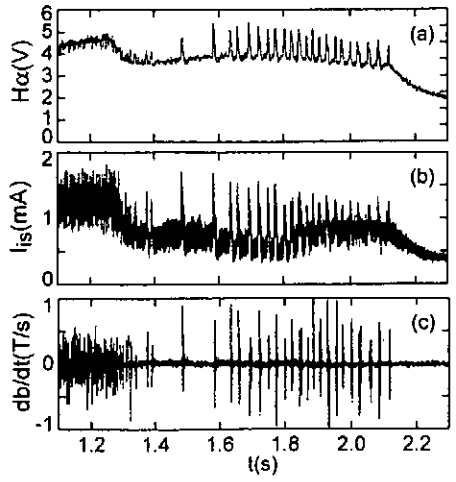

Fig.4 Enlarged signals of Fig.3; (a) Hα, (b) I_{is}, (c) db/dt.

also observed in an electrostatic probe on the divertor plate (I_{is}) and a magnetic probe (db/dt). They are also traced in the expanded time scale in Fig.4. Reduction of the magnetic fluctuation is seen after the H-mode-like transition.

This H-mode-like feature, however, disappears after turning off the second NBI at t=2.1s. It strongly suggests that a relatively narrow power window exists for appearance of the H-mode-like phase. In order to confirm the existence of power window the P_{NBI} was increased from one beam to two beams, as shown in Fig.5. The H-mode-like phase was obtained only in the time interval of the P_{NBI} increase during t=1.8-2.8s.

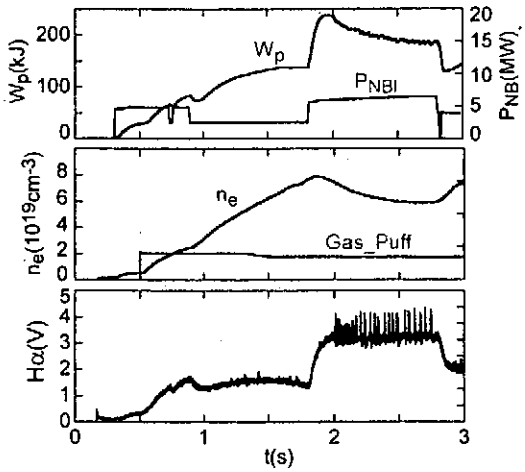

Fig.5 H-mode-like discharge after P_{NBI} increase.

In addition, the H-mode-like discharges cannot be obtained in low- and high-density ranges, appearing only in a density range of 4-8x10^{13}cm^{-3}. This fact strongly suggests that this phenomenon is sensitive to plasma conditions around $\iota/2\pi(a)=1$ surface. The pressure gradient at the position of 1/1 surface could be a driving force for appearance of the Hα bursts.

The edge density behaviors were analyzed from signals of multichannel interferometer, which measures vertical chord-integrated densities (n_eL) at vertically elongated plasma cross-section. Temporal behaviors of two chord-integrated densities from edge region at inboard side are traced in Fig.6 (b) and (c) with the connection length in Fig.6 (a). The ergodic layer becomes thick at the inboard side in such outwardly shifted configuration of R_{ax}=4.00m. The position of LCFS is R=3.529m at the inboard side. Then, both signals in Fig.6 (b) and (c) show the density from the ergodic layer. One of the densities (R=3.489m) in Fig.6 (c) is close

to the LCFS. Relatively high density exists even in R=3.399m where the L_c is roughly 100m.

The density bursts become remarkable in the inboard side as seen in Fig.6 (b) and can be well correlated with the Hα bursts. The density from R=3.489m in Fig.6 (c), however, indicates an inverse temporal behavior. A density collapse toward the plasma boundary from the inside is seen. It is calculated that the 1/1 surface in this position exists near R=3.46m located between two interferometer chords of R=3.399 and 3.489m. The position of the 1/1 surface possibly corresponds to the inversion radius of the density collapse. This density collapse appeared inside the ergodic layer suggests that some part of the ergodic layer having a relatively long L_c behaves like a core plasma with well-defined magnetic surface. In other words, the perpendicular diffusion becomes important in such a region. Then, the presence of the 1/1 surface at the ergodic layer can play an important role in terms of the confinement improvement, e.g, formation of a sharp boundary.

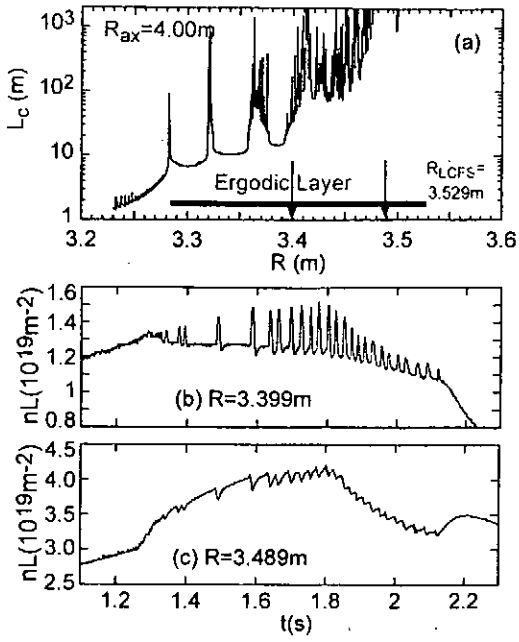

Fig.6 L_c at vertical-inside of R_{ax}=4.00m (a) and enlarged n_eL of Fig.3 (b), (c). Two arrows indicate positions of measured n_eL.

4. Concluding remarks

Since the tangency radius of the present NBI is R=3.70-3.75m, the energy confinement in such an outwardly shifted configuration is always much smaller than in ISS-95 scaling due to less central heat deposition. The energy confinement times obtained in the discharge shown in Fig.3 are 17ms (τ_{E_ISS95}=36ms) and 41ms (τ_{E_ISS95}=65ms) at t=1.2 and 2.0s, respectively. A clear confinement improvement has not been observed at present. However, the H-mode-like discharges mentioned above, at least, provide us interesting data related to the edge physics. For this purpose edge plasma diagnostics becomes more important in LHD, because we have now no exact information on the density and temperature profiles in the ergodic layer.

[1] V.Erckmann *et al.*, Phys.Rev.Lett **70**, 2086 (1993).
[2] K.Toi *et al.*, Proc. 14th International Conference on Plasma Physics and Controlled Nuclear Fusion Research Vol.2, 461 (Vienna, 1993).
[3] K.Toi *et al.*, Plasma Physics and Controlled Fusion **38**, 1289 (1996).
[4] S.Okamura *et al.*, Journal of Plasma Fusion Research **79**, 977 (2003).
[5] F.Sano *et al.*, Journal of Plasma Fusion Research **79**, 1111 (2003).
[6] K.Toi *et al.*, Nucl. Fusion **44**, 217 (2004).
[7] S.Morita *et al.*, Journal of Plasma Fusion Research **80**, 279 (2004).
[8] T.Morisaki *et al.*, J.Nucl.Mater. **313-316**, 548 (2003).

Magnetic Island Generation in Nonlinear Evolution of Interchange Mode

K.Ichiguchi[1], B.A.Carreras[2]

[1]*National Institute for Fusion Science, Oroshi-cho 322-6, Toki 509-5292, Japan*
[2]*Oak Ridge National Laboratory, Oak Ridge, Tennessee 37831, USA*[A]

Abstract : Generation of the magnetic islands in the nonlinear evolution of the resistive interchange mode is investigated numerically based on the reduced magnetohydrodynamics (MHD) equations. The islands are generated by the interchange flow of the instability without current concentration at the resonant surface. The deformation of the contour of the perturbed poloidal flux is essential in the island generation.

1. Introduction

In the linear analysis of the resistive interchange mode in the slab geometry, the mode structure of the poloidal magnetic flux is an odd function with respect to the resonant surface. Therefore, it is generally considered that magnetic islands are hardly generated by the interchange mode. On the other hand, significant magnetic islands were obtained in the nonlinear calculation of the interchange mode[1-3]. The common feature of these islands is that the number of the island in the poloidal cross section is twice of the poloidal mode number of the dominant component. This feature is quite different from that of the tearing mode. Thus, the mechanism of the island generation is discussed in the present paper.

2. Basic Equation and Configuration

The nonlinear evolution of the resistive interchange mode is examined by using the NORM code[3]. This code solves the reduced MHD equations for stream function Φ, poloidal flux Ψ and plasma pressure P. We employ the cylindrical geometry (r, θ, z) to avoid the stochasticity attributed to the toroidicity. In this case, the magnetic field $\mathbf{B}$ and the perpendicular velocity $\mathbf{v}_\perp$ are given by $\mathbf{B} = B_0\mathbf{e}_z + \mathbf{e}_z \times \nabla\Psi$ and $\mathbf{v}_\perp = \nabla\Phi \times \mathbf{e}_z$, respectively, where $\mathbf{e}_z$ denotes the unit vector in z direction.

In the present analysis, we employ the no net current equilibrium with the pressure profile of $P_{eq} = P_0(1 - r^4)$ at $\beta_0 = 2\%$. The average curvature of the magnetic field line is calculated by using the cylindrical component of the LHD configuration, which drives the interchange mode with the pressure gradient. In this equilibrium, the rational surface with $\iota_{eq} = 1/2$ exists in the plasma column. Therefore, we investigate the perturbation with a single helicity of $n/m = 1/2$. Here, m and n denote the poloidal and the toroidal mode numbers, respectively. The perturbations are expanded in the Fourier series in the ways of $\tilde{\Psi} = \sum_n \tilde{\Psi}_{mn}(r)\cos(m\theta - n\zeta)$,

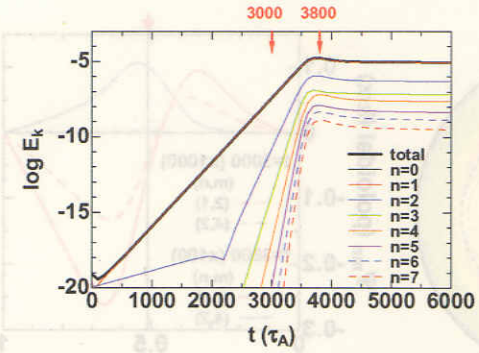

Fig.1. Time evolution of kinetic energy.

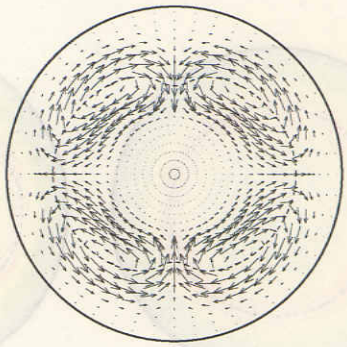

Fig.2. Flow pattern at $t = 3800\tau_A$ for $r \leq 0.8$.

$\tilde{\Phi} = \sum_n \tilde{\Phi}_{mn}(r)\sin(m\theta - n\zeta)$ and $\tilde{P} = \sum_n \tilde{P}_{mn}(r)\cos(m\theta - n\zeta)$, where $\zeta = z/R_0$. To clarify the reconnection process, we use a fairly large resistivity of $S = 10^4$, where S denotes the magnetic Reynolds number. The fluid viscosity and the perpendicular heat conductivity are introduced so that the $(m,n) = (2,1)$ component has the largest growth rate in the linear phase.

3. Island generation and reconnection mechanism

Figure 1 shows the time evolution of the kinetic energy, which is defined by $E_k = \sum_n E_k^n$, $E_k^n = \frac{1}{2}\int |\nabla_\perp \tilde{\Phi}_{mn}\sin(m\theta - n\zeta)|^2 dV$. The kinetic energy saturates at $t = 3700\tau_A$ and the $(m,n) = (2,1)$ mode is dominant in the whole time evolution, where τ_A denotes the poloidal Alfvén time. Figure 2 shows the flow pattern on the poloidal cross section of $z = 0$ at $t = 3800\tau_A$. We also plot the position of the resonant surface where the total rotational transform ι_T equals to 1/2, which is defined by $\iota_T(r,\theta,z) = \frac{1}{r}\frac{\partial}{\partial r}[\Psi_{eq}(r) + \tilde{\Psi}(r,\theta,z)]\frac{R_0}{B_0}$. Four vortices are seen around the resonant surface. This pattern corresponds to the typical linear eigenfunction of the interchange mode with $m = 2$. The surface with $\iota_T = 1/2$ is deformed by the radial component of the flow.

Since we treat the single helicity perturbation, the structure of the magnetic island can be observed by plotting the helical magnetic flux Ψ_h, which is defined by $\Psi_h(r,\theta,z) = \tilde{\Psi}(r,\theta,z) + \Psi_{eq}(r) - \frac{1}{2}r^2\frac{n}{m}\frac{B_0}{R_0}$. Figure 3 shows the contour of the helical flux on the poloidal cross section at $t = 3000\tau_A$ (linear phase) and $t = 3800\tau_A$ (nonlinear saturation phase). At $t = 3000\tau_A$, two thin islands are observed. The island structure is consistent with the linear eigenfunction of the $m = 2$ resistive interchange mode shown in Fig.4. In this case, $\tilde{\Psi}_{21}$ is an odd function with finite value at the resonant surface. These islands are considered to be generated spontaneously due to the cylindrical geometry and the large resistivity. The X-points of the spontaneous islands are maintained through the whole time evolution. We call them major X-points.

At $t = 3800\tau_A$, new X-points are generated at the positions of the O-points of the sponta-

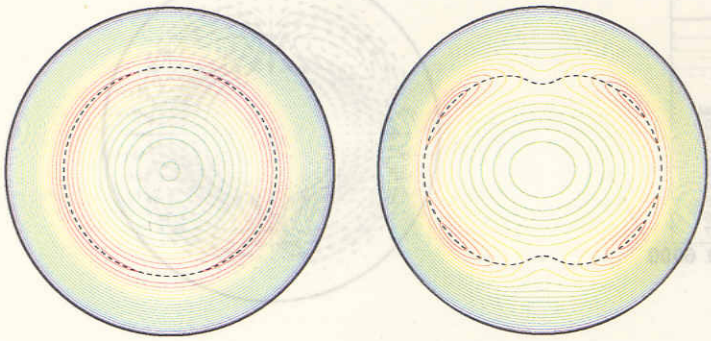

Fig.3. Contour of Ψ_h at $t = 3000\tau_A$ (left) and $t = 3800\tau_A$ (right) for $r \leq 0.8$. Dashed lines show the position of the surfaces with $\iota_T = 1/2$.

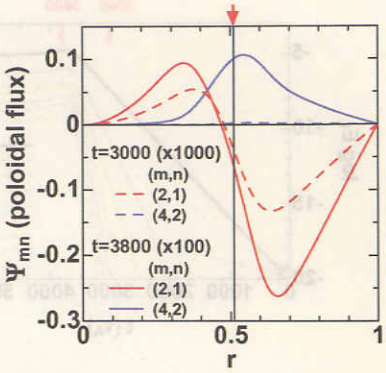

Fig.4. Profiles of perturbed poloidal flux. Red arrow indicates the position of $\iota_{eq} = 1/2$.

neous islands ($\theta = 0$ and $\theta = \pi$) , as shown in Fig.3(right). We call them minor X-points. As a result, the $m = 4$ islands exist inside the $m = 2$ islands. This island structure corresponds to the mode structure of $\tilde{\Psi}_{mn}$ shown in Fig.4. The component of $\tilde{\Psi}_{42}$, which is an even function, has a comparable value with that of $\tilde{\Psi}_{21}$ at the resonant surface.

The appearance of the even function of $\tilde{\Psi}_{42}$ can be explained analytically. For simplicity, we employ the slab geometry around the resonant surface, $r = r_s$. We introduce an ordering that the Fourier components $\tilde{\Phi}_{mn}(x)$ and $\tilde{\Psi}_{mn}(x)$ should be the order of $O(\delta^n)$ with small parameter δ, where $x = r - r_s$. The lowest order of $\tilde{\Phi}_{mn}$ is $\tilde{\Phi}_{21}$ in $O(\delta)$. As the structure of the mode can be approximated by the linear eigenfunction, $\tilde{\Phi}_{21}$ can be written as $\tilde{\Phi}_{21} = \overline{\Phi}\exp[-x^2/(2w_{21}^2)]$, where $\overline{\Phi}$ is a constant and w_{21} denotes the mode width. Then, the function of $\tilde{\Psi}_{21}$ can be obtained from the Ohm's law in the order of $O(\delta)$. By substituting $\tilde{\Phi}_{21}$ and $\tilde{\Psi}_{21}$ into the Ohm's law in the next order, we can obtain the function of $\tilde{\Psi}_{42}$, which are given by $\tilde{\Psi}_{42} = \overline{\Psi}\{1 + (A/S)[4 - 5(x^2/w_{21}^2)]\}\exp[-x^2/(w_{21}^2)]$. Here $\overline{\Psi}$ and A are constant. The resistive term is included successively up to $O(1/S)$ here. The expression of $\tilde{\Psi}_{42}$ shows an even function with the width of $w_{21}/\sqrt{2}$, which corresponds to the structure shown in Fig.4.

The mechanism of the minor X-point generation can be explained with the change of the radial magnetic component $\tilde{B}_r$. To change O-point to X-point with the poloidal component of the helical magnetic field fixed, the direction of $\tilde{B}_r$ has to be reversed around the point. This is shown in Fig.5 where we have plotted $\tilde{B}_r$ along the resonant surface in the poloidal cross section. In the region of $0 \leq \theta \leq 0.2\pi$, $\tilde{B}_r$ is negative for $t \leq 3500\tau_A$ while it is positive for $t \geq 3600\tau_A$ in the present case.

The perturbed magnetic field vector is tangential to the surface of $\tilde{\Psi} = const.$ Hence, the reversal of B_r direction is concerned with the structure of the $\tilde{\Psi} = const.$ surface. Figure 6

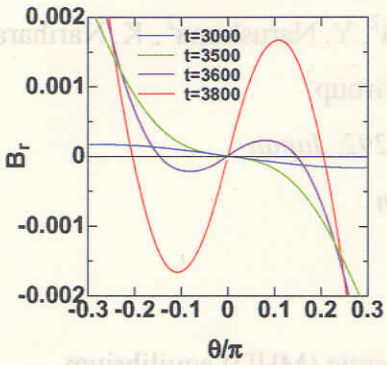

Fig.5. Time evolution of $\tilde{B}_r$ profile along the resonant surface.

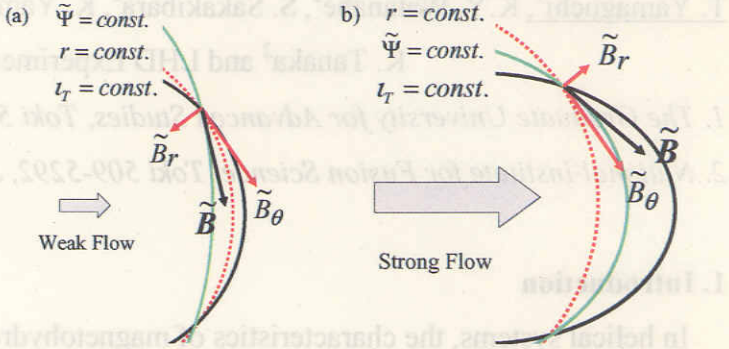

Fig.6. Schematic pictures of $\tilde{\Psi}$ around $\theta = 0$ at (a) $t = 3000\tau_A$ and (b) $t = 3800\tau_A$.

schematically shows the surfaces of $\tilde{\Psi} = const.$, $r = const.$ and $\iota_T = 1/2$ on the $z = 0$ poloidal cross section, which cross at $\theta = 0.1\pi$. The numerical result shows that the radial curvature of the $\tilde{\Psi} = const.$ surface is smaller than $1/r$ at $t = 3000\tau_A$. This indicates that $\tilde{B}_r$ is negative at the cross point as shown in Fig.6(a). On the other hand, at $t = 3800\tau_A$, the radial curvature of the $\tilde{\Psi} = const.$ surface is larger than $1/r$ at the same position. This indicates that $\tilde{B}_r$ is positive. Therefore, the curvature enhancement of the $\tilde{\Psi} = const.$ surface results in the generation of the minor X-point. This curvature enhancement is caused by the increase of the outward radial flow shown in Fig.2.

4. Conclusions

In the nonlinear saturation phase of the resistive interchange mode, magnetic islands can be generated by the flow across the resonant surface. In this case, the poloidal number of the island is twice that of the poloidal mode number of the dominant component. The curvature enhancement of the perturbed poloidal flux contour due to the increase of the radial flow is essential in the reconnection process. This mechanism is different from that of the standard driven reconnection because current concentration at the resonant surface is not observed.

Acknowledgments

This work was partially supported by the Grant-in-Aid for Scientific Research (C) 13680572 of Japan Society for the Promotion of Science.

References

[1] M.Wakatani, et al., Nucl. Fusion **24** (1984) 1407.

[2] B.A.Carreras, et al., Phys. Plasmas **10** (1998) 3700.

[3] K.Ichiguchi, et al., Nucl. Fusion **43** (2003) 1101.

Magnetic Measurements for MHD Equilibrium Reconstruction in LHD

T. Yamaguchi[1], K.Y. Watanabe[2], S. Sakakibara[2], K. Yamazaki[2], Y. Narushima[2], K. Narihara[2], K. Tanaka[2] and LHD Experimental Group[2]

1. The Graduate University for Advanced Studies, Toki 509-5292, Japan

2. National Institute for Fusion Science, Toki 509-5292, Japan

1. Introduction

In helical systems, the characteristics of magnetohydrodynamic (MHD) equilibrium, stability and transport with the high plasma pressure and the large toroidal current are quite different from those in vacuum. Then, it is one of the important issues to establish a method of MHD equilibrium reconstruction consistent with experimental observations. Though magnetic measurements are known to be powerful tools for the MHD equilibrium reconstruction, the MHD equilibrium reconstruction method using magnetic measurements has not established in helical devices. However, the magnetic measurements have a capability to measure the important equilibrium parameters like beta, its profile and the pressure anisotropy[1, 2]. To estimate beta value, two types of magnetic diagnostics, the diamagnetic flux loop and saddle flux loops, are installed in LHD. The diamagnetic flux loop is sensitive to the total plasma energy but it is not sensitive to the pressure profile. On the contrary, saddle flux loops are sensitive to both of them. As another difference, the diamagnetic flux loop measures the diamagnetic current induced by the perpendicular pressure ($p_\perp$), while saddle loops measure Pfirsch-Schlüter (P.S.) current induced by the sum of the perpendicular and parallel pressures ($p_\perp+p_{//}$). In this paper, we focus the effect of anisotropic beam pressure on the total pressure based on magnetic measurements.

2. Experimental setup

LHD is a heliotron device with L=2 and M=10 super-conducting helical coils and three pairs of poloidal coils[3]. Here L is a pole number and M is the field period of helical coil system. The machine major radius is 3.9 m, and the plasma minor radius is 0.64 m in a typical operation. The diamagnetic loop is installed inside vacuum vessel. The eddy current in structures are measured with Rogowski coils. The current increment of the helical coils and poloidal coils during discharges are also measured. They are used for calibrations of the diamagnetic flux. Saddle loops have been installed along helical coils inside vacuum vessel. Figures 1 and 2 show locations of saddle loops in a top-view and a poloidal cross section. They are not sensitive to the magnetic field from helical coil currents and eddy currents in structures,

because they flow in the parallel direction of them. In LHD, there are 24 saddle loops whose toroidal and poloidal angles are different. The saddle loops whose positions are top or bottom of plasmas are used for this study because they are suitable to measure magnetic field from P.S. current.

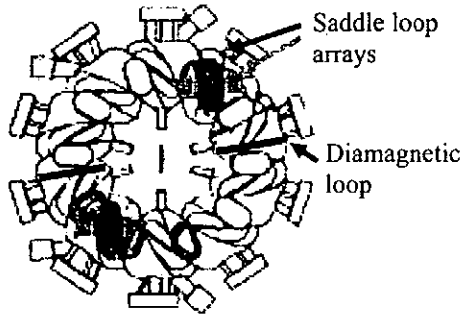

Fig.1 The location of saddle flux loops and diamagnetic loops.

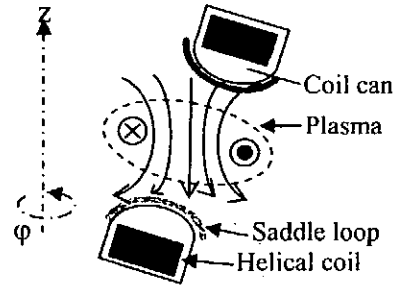

Fig.2 Saddle flux loops location and P.S. current.

3. Equilibrium analyses

The fluxes of magnetic diagnostics are estimated by using 3-D MHD equilibrium analysis code VMEC[4] and DIAGNO[5] under the asummption of isotropic pressure. Figure 3 shows the estimation of the saddle loop flux Φ_{SL} and the diamagnetic flux Φ_{dia} with no toroidal current. Pressure profiles shown in Fig.3(a) and the toroidal flux Φ_0=3.144 (Weber) at 3T operation are used for calculations. As the pressure profile becomes more peaked, the saddle loop signal is larger, because P.S. current is larger as the gradient of pressure is larger. While the diamagnetic loop is not sensitive to the pressure profile.

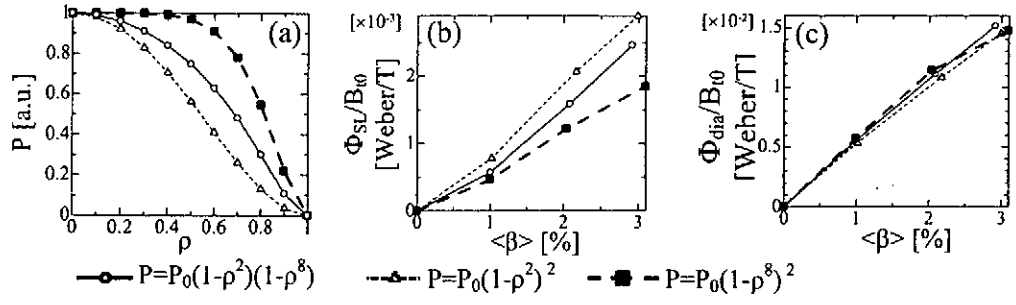

Fig. 3 (a)Pressure profile used this analysis. (b)The dependence of Φ_{SL} on pressure profiles with Φ_0=3.144 [Weber], where ρ is a normalized minor radius and B_{t0} is magnetic field strength at magnetic axis in the vacuum filed. (c) The dependence of Φ_{dia} on that.

4. Experimental result

Figure 4 shows time evolutions of Φ_{dia}, Φ_{SL}, the electron stored energy W_{pe} by profile measurements which are Thomson scattering and FIR laser interferometer, the line averaged electron density $\bar{n}_e$ and NBI power. In Fig. 5, we show the electron pressure profile measured by profile measurements at 1075, 1625, 2025 (msec) and the model pressure profile with the parabola $P=P_0(1-\rho^2)(1-\rho^8)$ and the broad $P=P_0(1-\rho^6)^2$. Figure 6 shows the experimental time

trace of Φ_{dia} and Φ_{SL}. Green lines denote the relationships between Φ_{dia} and Φ_{SL} by calculations. From these figures, the experimental pressure profiles are between a parabolic model and a broad model and do not change so much on the time, but the ratio of Φ_{dia} and Φ_{SL} experimentally observed changes significantly. In the density-increase phase (a → b), we can see that Φ_{SL}/Φ_{dia} decreases. In the density-decrease phase(b → c), it increases. After NBI #1 off (c→d), W_{pe} and Φ_{dia} do not change so much while Φ_{SL} decreases. Φ_{SL}/Φ_{dia} has a strong correlation with $\bar{n}_e$.

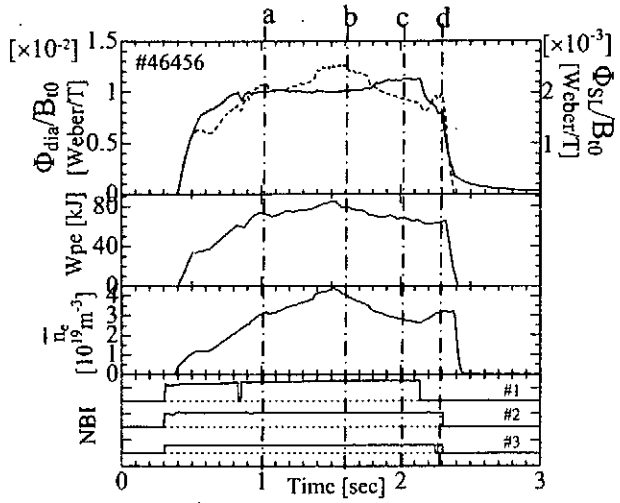

Fig. 4 Time evolutions of Φ_{dia}, Φ_{SL} and key parameters.

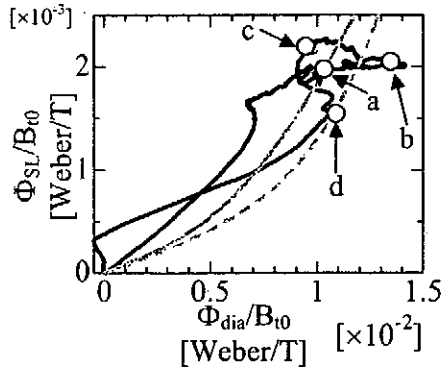

Fig.6 The time trace of measured Φ_{dia}, Φ_{SL} and isotropic estimations.

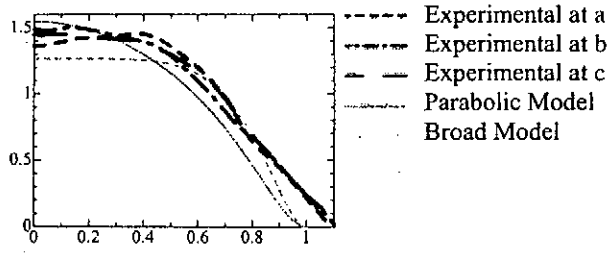

Fig. 5 The time evolution of pressure profile.

Figure 7 shows the relationship of measured Φ_{dia} and Φ_{SL} in many discharges where $\bar{n}_e$ are lager than $1\times10^{19}m^{-3}$ and B_{t0} are 0.5, 0.75 and 1.5T. And, the Φ_{dia} and Φ_{SL} calculated by VMEC-DIAGNO are shown under the assumption of parabolic and broad pressure profile models. We can see the strong correlation between Φ_{dia}/Φ_{SL} and $\bar{n}_e$, a higher density leads to a low value of Φ_{dia}/Φ_{SL}, in many discharges. In Fig.8, we show the comparison between the pressure anisotropy estimated by saddle loop fluxes and that by beam calculations due to NBI. Here we consider the following parameters; the pressure anisotropy estimated by saddle loops, $\Phi_{SL}^{exp}/\Phi_{SL}^{iso}$, and that estimated based on the beam calculation and diamagnetic measurements, W^{total}/W_{dia}. Here Φ_{SL}^{exp} is the measured saddle loop flux, Φ_{SL}^{iso} is VMEC-DIAGNO estimation under the assumption of parabolic pressure profile model, W_{dia} is the stored energy measured by the diamagnetic flux loop and W^{total} is the total energy. We assume $W_{dia}=W^{thermal}+1.5\,W_{\perp}^{beam}$, where $W^{thermal}$ is the

thermal energy and $W_{\perp}^{beam}$ is the perpendicular component of the beam energy. Then, W^{total} is given by

$$W^{total} = W^{thermal} + W_{\perp}^{beam} + W_{\parallel}^{beam} = W_{dia} - 0.5W_{\perp}^{beam} + W_{\parallel}^{beam} \quad (1)$$

where $W_{\parallel}^{beam}$ is the parallel component of the beam energy. $W_{\perp}^{beam}$ and $W_{\parallel}^{beam}$ are calculated by a three-dimensional Monte Carlo simulation code [6]. The dependence of $\Phi_{SL}^{exp}/\Phi_{SL}^{iso}$ on $\bar{n}_e$ is consistent with that of W^{total}/W_{dia}. We consider that $\Phi_{SL}^{exp}/\Phi_{SL}^{iso}$ detects the pressure anisotropy, because the parallel component of NBI power is dominant in LHD and the beam contribution to pressure is large anisotropy in low density.

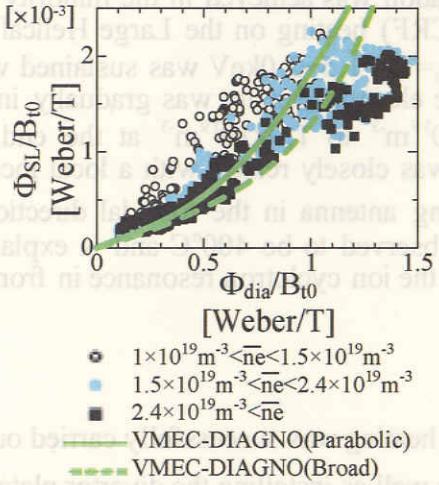

Fig. 7 The dependence of Φ_{dia} and Φ_{SL} on $\bar{n}_e$.

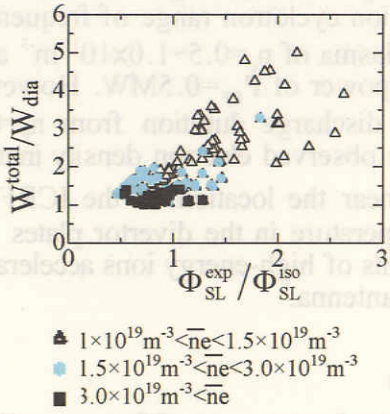

Fig. 8 The comparison between $\Phi_{SL}^{exp}/\Phi_{SL}^{iso}$ and W^{total}/W_{dia}.

5. Summary

The experimental time trace of Φ_{dia} and Φ_{SL} is not consistent with VMEC-DIAGNO calculation when the isotropic pressure is assumed. The ratio between experimental saddle loop flux and isotropic estimation depends on $\bar{n}_e$ and it is consistent with the beam energy calculation due to NBI. We have confirmed that the diamagnetic loop and the saddle loop has a capability to measure the pressure profile and the pressure anisotropy in LHD. We need more analyses to quantitatively evaluate the pressure profile and the pressure anisotropy.

References

[1] S. Morimoto, et al., Nucl. Fusion **28**, 1491 (1988).

[2] J. Qin, et al., Nucl. Fusion **36**, 381 (1996).

[3] A. Iiyoshi et al., Nucl. Fusion **39**, 1245 (1999).

[4] S. P. Hirshman and W. I. van Rij, Comput. Phys. Commun. **43**, 143 (1986).

[5] H. J. Gardner, Nucl. Fusion **30**, 1417 (1990).

[6] S. Murakami, N. Nakajima and M. Okamoto, Trans. Fusion Technol., 27, 256 (1995).

Density Increase during Steady-state Plasma Discharge on the Large_Helical Device

R.Kumazawa[1], S.Sakakibara[1], K.Saito[1], T.Mutoh[1], T.Seki[1], T.Watari[1], Y.Nakamura[1], M.Sakamoto[2], T.Watanabe[1], N.Takeuchi[3], Y.Torii[4], F.Shimpo[1], G.Nomura[1], M.Yokota[1], A.Kato[1], H.Okada[4], Y.Zao[5] and LHD Experimental Group

[1]*National Institute for Fusion Science, Toki 509-5292, Japan*
[2]*Kyusyu University, Research Institute for Applied Mechanics, Kasuga, 816-8580, Japan*
[3]*Nagoya University, Faculty of Engineering, Nagoya 464-8601, Japan*
[4]*Kyoto University, Institute of Advanced Energy, Uji, 611-0011, Japan*
[5]*Academia Sinica Plasma Physics Institute, Hefei, 230031, People's Republic of China*

The long pulse plasma discharge with 150sec operation was achieved in the minority heating method of an ion cyclotron range of frequency (ICRF) heating on the Large Helical Device (LHD). The plasma of n_e=0.5~1.0x10^{19}m^{-3} and T_{e0}=T_{i0}=1.5~2.0keV was sustained with the ICRF heating power of P_{RF}=0.5MW. However the electron density was gradually increased after the half discharge duration from n_e=0.5x10^{19}m^{-3} to 1.0x10^{19}m^{-3} at the end of the discharge. The observed electron density increase was closely related with a local increase in Hα intensity near the location of the ICRF heating antenna in the toroidal direction. The maximum temperature in the divertor plates was observed to be 400°C and is explained by calculating orbits of high-energy ions accelerated at the ion cyclotron resonance in front of the ICRF heating antenna.

Introduction

The ion cyclotron range of frequency (ICRF) heating was successfully carried out on the LHD employing the inward-shifted magnetic axis as well as installing the divertor plates [1~3]. It is experimentally proved that the optimized heating mode is obtained when the ion cyclotron resonance layer is located at the saddle point of the mod B surface. In this heating mode, minority ions absorb most of the injected RF power to form a high-energy ion tail and its energy is efficiently transferred to the bulk plasma [4]. A trial of a long pulse plasma discharge using an ICRF heated plasma was started in 1999. A long discharge of 68sec was achieved in the plasma with n_e=1.0x10^{19}m^{-3} and the electron temperature on the axis T_{e0}=2.0keV with P_{RF}=0.7MW [5, 6]. The pulse length was limited by the RF generator problem. Then it was gradually prolonged from 68sec to 127sec in 2001 [7, 8]. The plasma duration time was seemed to be limited to the electron density increase up to the critical density depending the heating power; however data were not enough to analyze the cause of the density increase.

In this paper a long pulse plasma discharge sustained by ICRF heating only is reported. In Sec.2 the typical plasma discharge of the long pulse operation is described. Reasons limiting the plasma duration are analyzed. Then experimental data are compared with results obtained from an orbit calculation of high-energy ions accelerated at the ion cyclotron resonance layer. Then we summarize.

2. Experimental results

Time evolutions of plasma parameters of the long pulse plasma discharge are plotted in Fig. 1(a); this is the longest plasma discharge so far achieved in the ICRF heated plasma. The plasma with the electron density n_e=5~6x$10^{18}m^{-3}$, and the electron temperature and the ion temperature on the magnetic axis $T_{e0}=T_{i0}$=2.0keV was sustained with the ICRF heating power of P_{RF}=0.5MW. After 90 seconds the electron density was observed to be increase with the time accompanied an increase in the radiated power (P_{rad}) and to end up to n_e=1x$10^{19}m^{-3}$ with P_{rad}=250kW before the plasma suddenly disappeared at 150 seconds. The power supply from the RF generator was automatically ceased monitoring an increased reflected-power due to shrinking the plasma radius, when the plasma was collapsed. Besides several plasma parameters time evolutions of the vacuum pressure, the visible emission of Hα and HeI normalized by the electron density, and the temperatures increase in the divertor plates and in the vacuum wall are plotted in Fig. 1(b): The vacuum pressure is increased by 3x10^{-5}Pa from P_V=2x10^{-4}Pa after 90s. The intensity of Hα signal (3-O vacuum port, which is near the ICRF heating antenna) was doubled. The temperature of the divertor plate (3-I, 3rd inboard section) was increased to 400°C; as the time constant of the divertor plate is an order of 100s, the measured temperature is almost saturated. On the other hand the vacuum vessel temperature was increased by 3°C; however as the time constant of the vacuum vessel is about 1 hour, the temperature increase was found to be small.

An electron density limit of the ICRF heated plasma was examined in the series of the experiments as shown in Fig. 2. Experimental data are plotted in P_{ICH}(MW)-n_e($10^{19}m^{-3}$) plane. The critical electron density n_{ecr} at the heating power range of 0.2MW< P_{ICH} <1.5MW is given in the following relation; $n_{ecr}(10^{19}m^{-3}) = 1.8P_{RF}(MW)$. When the electron density is increased up to n_{ecr}, a radiated power fraction P_{rad}/P_{RF} is proportionally increased with a ratio of n_e/n_{ecr}, which is plotted by open circles in Fig. 3. When the electron density was increased to n_e=1x$10^{19}m^{-3}$ at 150s as shown in Fig. 1(a), P_{rad}/P_{RF} reaches 50% and then the plasma was terminated. In Fig. 3 the behavior of P_{rad}/P_{RF} of this long pulse discharge is depicted against the normalized electron density n_e/n_{ecr}.

A toroidal asymmetry in Hα intensity [9] is plotted with open circles in Fig. 4. This is an increased ratio, which is the value at t=150sec normalized by that at t=90sec. It is easily found that the increase in Hα is prominent in 3-O and is about 2.5 times larger than that in 8-O. The ICRF heating antennas are installed at 3.5, that is between 3-O and 4-O. This increase in the Hα intensity is assumed to be attributed to the temperature increase in the graphite plates located near 3-O in the toroidal direction. A toroidal asymmetry in the temperature increase in the inboard side divertor plate is also shown in Fig. 4. It is found that the temperature increase

in the 3-I (No.3 of inboard side divertor plate) is prominent. The 3-I divertor plate of 400°C is thought to be a candidate of a hydrogen out-gassing source. This local temperature increase is compared with a calculation result of a particle orbit analysis. Two cyclotron resonance layers are separately located on the mod B surface in the employed magnetic configuration. The behavior of high-energy ions started at the cyclotron resonance layer (CRI) was examined using a full orbit calculation code [10, 11] under the RF electric field strength of 20kV/m [12]. About two thousands of high-energy ions with a low initial energy were started from the upper (referred to as UICR) and the lower (referred to as LICR) ion cyclotron resonance layers in various initial phase difference against the RF electric field. The starting position was selected in 100 positions from R=4.15m to =4.20m (the last magnetic closed surface is at R=4.14m) along the ion cyclotron layer. Some of them hit the divertor plates within one circulation along the toroidal direction. The toroidal distribution of loss energy of high-energy ions is plotted in Fig.5 to compare the measured temperature increase as shown in Fig.4. This orbit calculation suggests that the local temperature increase in divertor plates can be mitigated in two ICRF heating scenarios, in which the ion cyclotron resonance is located on the magnetic axis in the minority heating or is located near the low magnetic field region in the mode conversion heating; there exists no ion cyclotron resonance layer in front of the ICRF heating antennas.

Summary

The long pulse plasma with 150sec operation was achieved on the LHD. The plasma of n_e=0.5~1.0x$10^{19}m^{-3}$ and $T_{e0}=T_{i0}$=1.5~2.0keV was produced with the ICRF heating power of P_{ICH}=0.5MW. More than 70MJ of the heating energy was injected. However the density increase limited the plasma pulse length. The local temperature increase in the divertor plates is thought to be a cause of the increase in the electron density. It can be understood counting loss energy of high-energy ions accelerated at the ion cyclotron resonance layers on the outer board side of the torus in front of ICRF heating antennas in the orbit calculation.

Acknowledgement

The authors would like to thank the scientists and the technical staff at the National Institute for Fusion Science who enables us to conduct these experiments.

References

[1] Saito K et al Nucl. Fusion **41** 1021
[2] Mutoh T et al Phys. Rev. Lett. **85** 4530
[3] Kumazawa R et al Phys. Plasmas **8** 2139
[4] Kumazawa et al., Plasma Phys. Controlled Fusion **43** 1191
[5] Kumazawa R, et al., J. Plasma and Fusion Research SERIES, Vol. 3 352
[6] Watari T et al., Nucl. Fusion **41** 325
[7] Seki et al., Proc. 14th Top. Conf. on RF power in Plasmas 595(2001) 334
[8] Mutoh T et al., Nucl. Fusion **43** 738
[9] Goto M., et al., Physics of Plasmas **5** 1402
[10] Matsumoto Y et al., Japanese Journal of Applied Physics 43 (2004) 332
[11] Watanabe T, et.al., to be published in 20th IAEA paper
[12] Saito K et al., to be published in J. Nucl. Mater.

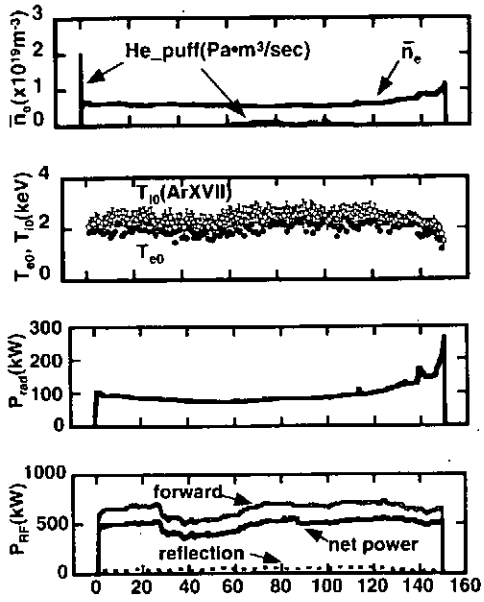

Fig.1(a) Time evolutions of plasma parameters, the electron density n_e, the electron T_{e0} and the ion temperature T_{i0} on the magnetic axis and the radiated power P_{rad} with the He gas puffing rate and the ICRF heating power P_{RF}.

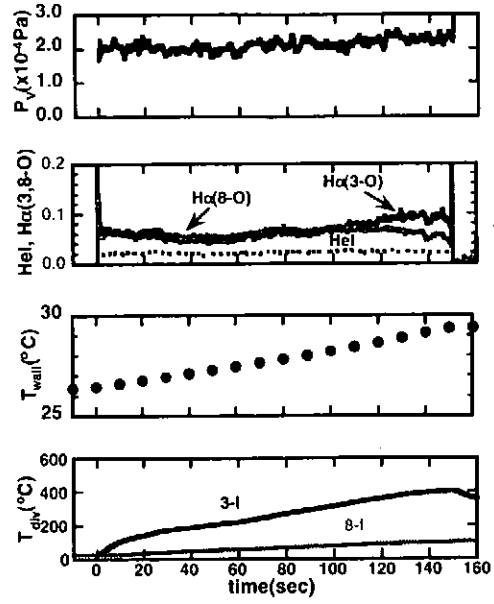

Fig.1(b) Time evolutions of the vacuum pressure P_v, the visible light emission of Hα and HeI, the temperature increase at the vacuum wall and at the divertor plates.

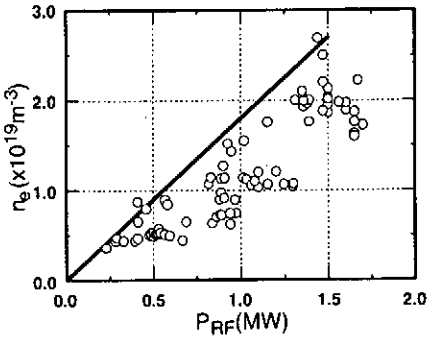

Fig.2 The relation between the critical electron density and the ICRF heating power.

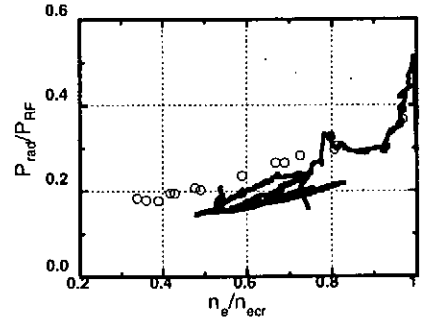

Fig.3 The fraction of the radiated power to the ICRF heating power vs. the ratio of the electron density to the critical electron density.

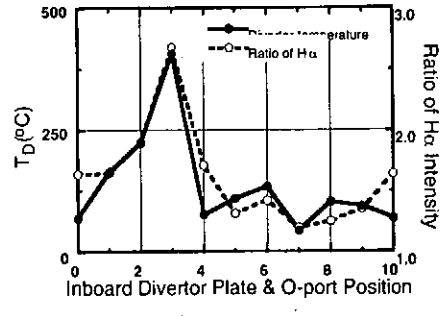

Fig.4 Toroidal distribution of temperature of the inboard divertor plates and ratio of Hα.

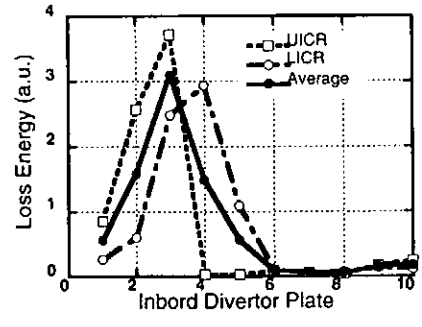

Fig.5 Toroidal distribution of loss energy of high-energy ions to divertor plates.

Fast Neutral Particle Spectra in Different Pitch Angles in Large Helical Device

T.Ozaki[1], P.Goncharov[1], S.Murakami[2], S.Sudo[1], H.Sanuki[1], T.Notake[3], K.Ida[1], K.Tanaka[1], Y.Oka[1], M.Osakabe[1], Y.Takeiri[1], K.Tsumori[1], K.Ikeda[1], O.Kaneko[1], K.Narihara[1], S.Okamura[1], S.Kubo[1], T.Shimozuma[1], K.Ohkubo[1], K.Sato[1], N.Tamura[1], A.Matsubara[1], D.Kalinina[4], M.Shoji[1], S.Kato[1], K.Yamauchi[1], H.Nakanishi[1], M.Kojima[1], Y. Narushima[1] K.Kawahata[1] and LHD Experimental Group

1. National Institute for Fusion Science, Toki, Gifu 509-5292, Japan
2. Department of Nuclear Engineering, Kyoto University, Kyoto, Japan
3. Department of Energy and Science, Nagoya University, Nagoya, 464-8603, Japan
4. Graduate Univ. for Advanced Studies, Hayama, Kanagawa, 240-0193, Japan

Introduction

It is not easy directly nor experimentally to observe the loss cone itself. The loss cone is strongly depended on the pitch angle and it is especially observed at higher pitch angle. In the Large Helical Device (LHD), the device design is devised so that the loss cone at ρ (radial position on the magnetic surface) <1/2 may not exist. Moreover, most of the particles heated by tangential NBI (Neutral Beam Injection) do not have a pitch angle perpendicular to a magnetic field. However, if the slowing down of the incident particle by electron collision occurs in NBI heating, the particle with a large pitch angle actually will be generated due to the scattering between the particle and plasma ion at several times the plasma temperature. These particles cause drift motion and rotate poloidally. They can almost be confined in the plasma because the energy of these particles is not so large. However part of them are not confined by balance with the electric field E. It is known for helical devices that the particle with a specific energy is lost by cancellation of the *grad B* drift and the *ExB* drift resulting from the electric field E [1]. This phenomenon occurs at the negative radial electric field. The reason why we are interested in the resonant loss is that we can find it from the dip in the high-energy particle spectra measured by the neutral particle analyzer.

The neutral particle analyzer in LHD has an ability of wide range scanning as a feature [2]. We have obtained various data in horizontal scan of the analyzer until now. Recently in addition of the horizontal scan, the high-speed perpendicular scan has become

possible, and new information on the poloidal direction can be acquired [3]. We can obtain the pitch angle dependence of the resonant loss by horizontal and continuous scanning of the analyzer during long steady-state discharges [4]. The somewhat large resonant loss can be observed in higher pitch angle, however it is not remarkable. The vertical scan has been also tried in order to obtain the radial information. The resonant loss is varied by the poloidal position although the pitch angle is not so different. This may be originated due to the spatial variety of the electric field. According to the experimental results, the dependence of the pitch angle is not so remarkable. The typical time scale of the pitch angle scattering is estimated to be a few milliseconds for the actual LHD plasma although the NPA detection duration is several tens of milliseconds [4]. Since pitch angle scattering is dominant and reaches equilibrium at the energy of 5 keV, the number of particles with lower pitch angle also decrease if the particle with higher pitch angle are lost.

Fig.1 Horizontal scan results and the simulation.
(a) (Upper center) Sight lines, (b) (Upper left) Tangential scan spectra, (c) (Lower right) Perpendicular scan spectra, (d) (Lower left) Simulation. Lower right in the figure is the effective particle generation region.

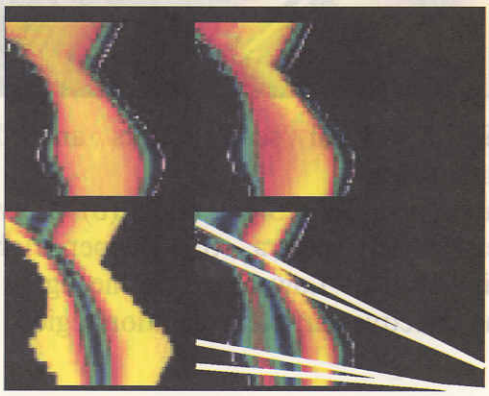

The Results from Horizontal Scan

The horizontal scan of NPA was performed by remote motor drive of the NPA stage. The scanning speed is 0.17 degree per second. The scanning center pitch angle, which is defined as the angle between the magnetic axis and the sightline, ranges from 40 degrees to

100 degrees. The experiments have performed in two middle duration discharges of 30 seconds. Figure 1(a) shows the experimental arrangement and the sight lines. During discharge, the analyzer was scanned horizontally. Figure 1(b) and (c) are the spectra in pitch angle of 30-40 and 70-80 degrees (the angle between the sight line and the magnetic axis). The resonant loss can be seen from 5 keV-15keV in the spectra. The dips at both pitch angles are not so different in spite of the different pitch angle.

To study the reason, we calculate the particle behavior in plasma using the simulation. The background neutral profile in the plasma parameter is obtained from the Aurora code. By considering the atomic process in plasma, we can obtain the generated particle profile with the energy of 5-15 keV including the particle loss from the source to the analyzer as shown in Fig. 1(d). The potential profile $\phi(\rho)$ in NBI plasma can be assumed to be $\phi(\rho)= -|\phi(0)|\{1-e^{(\rho 2-1)}\}$ from the data in Compact Helical System and LHD [5,6]. The electric field can be assumed to be $E_r=-|\phi(0)|\{2\rho\, e^{(\rho 2-1)}\}$. Therefore we can specify the position and the electric field of the observed particle. In calculation, the electric field at the generated point was not so varied by the horizontal scanning. The small variety of the dip can be explained by this reason.

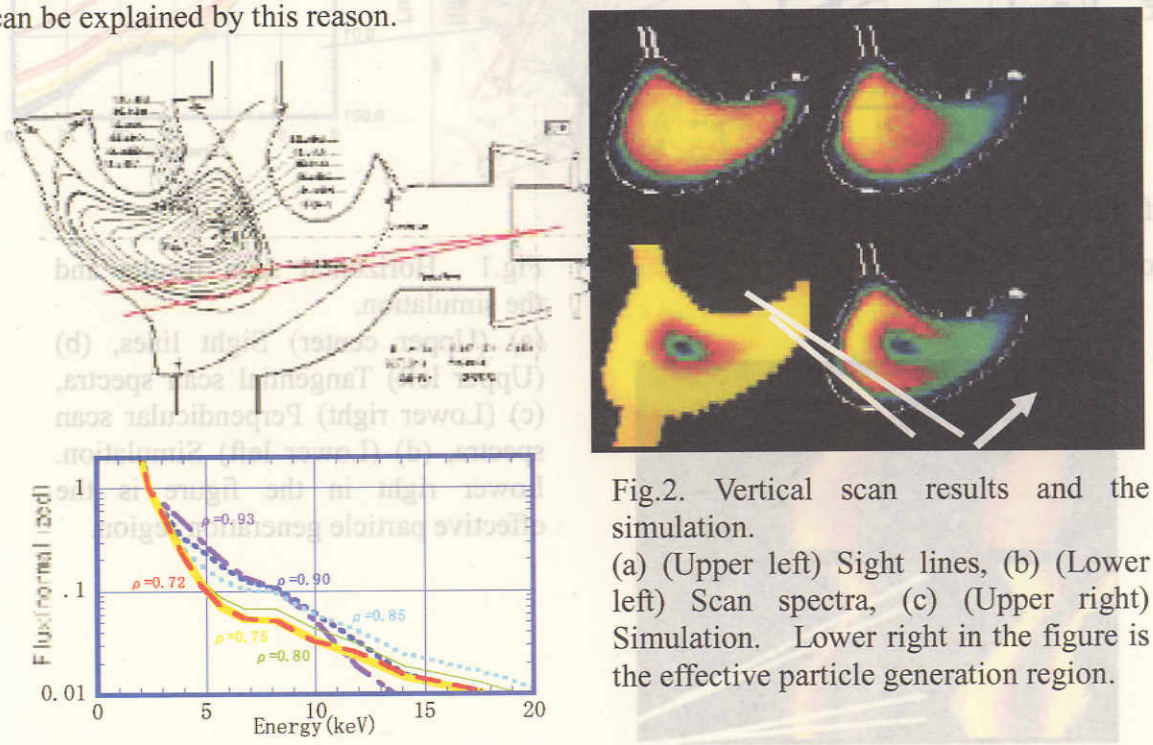

Fig.2. Vertical scan results and the simulation.
(a) (Upper left) Sight lines, (b) (Lower left) Scan spectra, (c) (Upper right) Simulation. Lower right in the figure is the effective particle generation region.

Vertical Scanning Results

The vertically scanning system is realized by adding a movable mechanism to a current horizontally scanning system. The analyzer slides along three stainless steel rails, which are arcs with radii of 4 m. One of the rails defines the accurate position of the

analyzer. Another rail, which is set at the front of this rail, fixes the vertical position and the other rail, which is set at the side, fixes the side position. Therefore, a smooth and non-vibrating vertical driving can be obtained. Two chains and the gears, which are connected with the motor, support the analyzer. Two stainless blocks are set on the opposite sides of the chain in order to balance the weight (700kg) of the analyzer and reduce the load in the motor. Therefore a very high scan speed of one degree per second can be obtained.

In horizontal scan the pitch angle dependence of the dip was not clear because the resonance loss depends on the electric field at the generation point. In the radial scan, the electric field and the generation points are obviously different by the radial position. Therefore the radial dependence of the dip can be expected. During steady-state operation of NBI plasma, the analyzer has been scanned continuously from ρ=0.9 to 0.7 as shown in Fig. 2(a). The typical spectra are shown in Fig. 2(b). The dips are varied in spite of the similar pitch angle. The inner region of plasma, larger dip can be observed. According to references [5,6], the large negative electric field at ρ=0.7 can be expected than at ρ=0.9. Figure 2(c) shows the simulation results. The bright color means much particle fluxes which are affected by the strong electric field in the observing energy range. The simulation results reflect the experimental results.

Summary

The 2-dimensional scanning neutral particle measurement system has been completed in order to investigate high-energy particle confinement. In the horizontal scan, the small variety of the dip can be expected because the electric field at the generated point was not so varied by the horizontal scanning. By adding the vertical scan, the radial variation of the signal loss associated with the resonant loss due to magnetic ripple was obtained in preliminary experimental results. The profile of the dip depth may reflect the electric field profile according to the comparison with the simulation.

References

[1] K. Hanatani, *et al.*, Nucl. Fusion 25 (1985) p.259.

[2]T.Ozaki, V.Zanza, *et al.*, Rev.of Sci. Instrum., **71** (7), 2698-2703 (2000).

[3]T.Ozaki, P.Goncharov, *et al.*, Rev. of Sci. Instrum., (to be published).

[4]T.Ozaki, *et al.*, Plasma Phys.and Fus. Res. SERIES(to be published).

[5]A. Fujisawa, *et al.*, IAEA-CN-64/C1-5 (1996).

[6]K. Ida, *et al.*, IAEA-CN-77/EX9/4 (2000).

Hybrid Probe Measurement of Peripheral Plasma on CHS

Kenichi Nagaoka, Masaki Osakabe, Masaki Nishiura, Chihiro Takahashi,
Mitsutaka Isobe, Tsuyoshi Akiyama, Akihiro Shimizu, Kazuo Toi,
Keisuke Matsuoka, Shoichi Okamura and CHS group
National Institute for Fusion Science, 322-6 Oroshi, Toki, Japan

1. Introduction

Recently, an edge transport barrier (ETB) formation with clear transition of H_α intensity has been observed in an NBI heated plasma on CHS [1], and understanding the mechanism underlying such phenomena is important and key issue for nuclear fusion research from the viewpoint of confinement improvement. The increase of plasma density in the edge region after the drop of H_α intensity has been observed by Thomson scattering, beam emission spectroscopy (BES), and Lithium beam probe measurements. In order to investigate in detail peripheral plasma near the last closed flux surface (LCFS), a multi-channel probe has been installed with a two-dimensional probe drive in outer edge region of horizontally elongated cross-section in CHS. Each probe head on the probe surface has a sheath thermocouple and acts as a calorimeter. Thus the probe can be used as not only conventional multi-channel Langmuir probe but also heat flux probe, so is called "hybrid probe". In this paper, the construction of the hybrid probe and two-dimensional probe drive are presented in section 2, experimental results of the probe measurement in section 3, and summary in section 4.

2. Hybrid Probe

Hybrid probe has been designed to measure both local plasma parameters by conventional Langmuir probe method and local heat flux. The probe is made of oxygen free high conductivity copper (40mm in diameter) with a water cooling system. There are ten probe heads (4mm in diameter) on the probe surface, and each head has a sheath thermocouple in order to estimate the local heat flux in a peripheral plasma (see fig. 1(a)). The probe is electrically isolated by CHS vacuum chamber, so keeps floating potential in plasmas. The voltage of each probe head is same and is able to be swept by a power supply.

Another feature of this measurement is to obtain the spatial distribution of some plasma parameters using a two-dimensional probe drive. The probe is inserted by a linear drive (750mm travel), of which insertion angle can be changed from -4 degrees to 20 degrees in the major radius direction. Thus a probe is able to scan in R-z space in wide region of horizontally elongated cross-section (see Fig. 1(b)). However, the insertion angle of the hybrid probe is

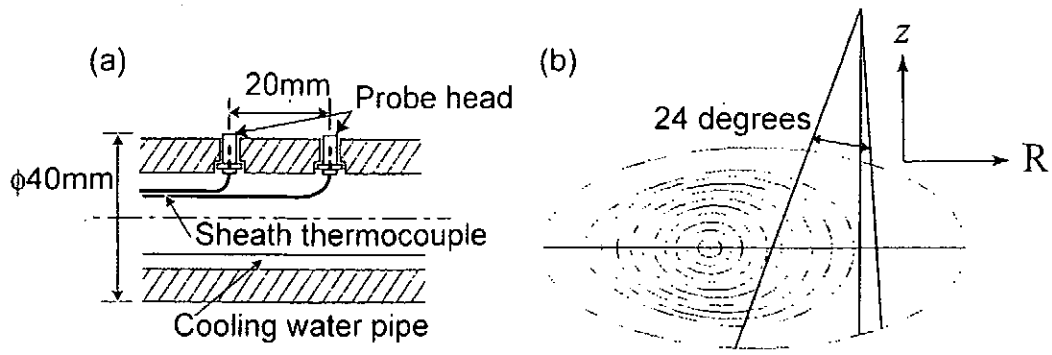

Figure 1. (a) Schematic of hybrid probe. (b) Cross-section of CHS plasma at Rax=0.921m and scannable area by the two-dimensional probe drive.

limited from -4 degrees to 4 degrees because of the size of the probe. A narrow probe less than 10mm in diameter is able to scan without the dimensional limitation.

3. Experimental Results

3-1 ETB formation The investigation of peripheral plasma with ETB using the hybrid probe has been performed in CHS. The ion saturation currents of ETB plasma were measured and the increase of ion current at R=1172mm (about 10mm inside of LCFS) with the reduction of H_α intensity was observed, while no clear change was observed at R=1207mm (about 25mm outside of LCFS), which are shown in Fig. 2 (a). The profiles of ion current were measured on z=0 line in the horizontally elongated cross-section. In Fig.2 (b), the four radial profiles of ion saturation currents in CHS plasmas (S.N.:114200-114211) are shown; case A (65msec): without ETB before the H_α reduction, case B (~72msec): onset of H_α reduction, case C (~77msec): the end of H_α reduction, and case D (85msec): with well-developed ETB. The electron temperature was also measured by sweeping the probe bias and was 8-20 eV in

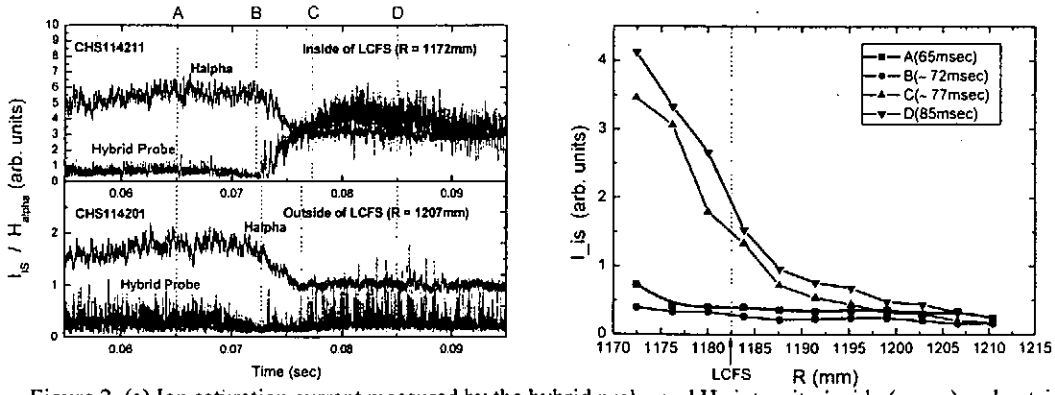

Figure 2. (a) Ion saturation current measured by the hybrid probe and H_α intensity inside (upper) and outside (lower) of LCFS. (b) Ion current profiles measured by the hybrid probe in different four times; A: 65msec, B: onset of H_α reduction, C: end of H_α reduction, and D: 85msec (with ETB).

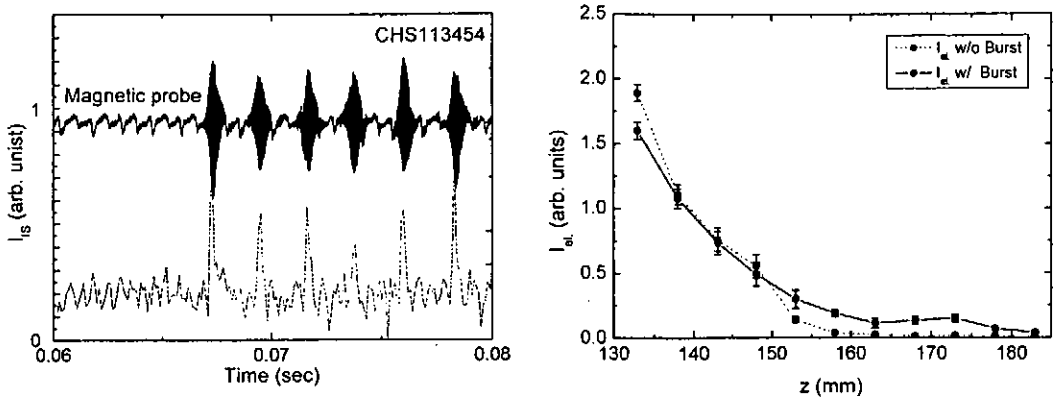

Figure 3. (a) Ion saturation current measured by the hybrid probe and signal of a magnetic probe. (b) Ion current profiles with and without the excitation of MHD burst.

the region 1180mm < z < 1195mm. There is little change between with or without ETB. In general, the ion saturation current is proportional to the plasma density and the square root of sum of electron and ion temperature, so the change of ion saturation current is considered to be mainly attributable to the change of plasma density. Thus it is concluded that the plasma density drastically increases at R<1200mm, and a steep density gradient is formed after H_α intensity reduction. Another characteristic of this transition is the slight decrease of the density just before H_α reduction in wide region near LCFS (case B in Fig. 2 (b)). However the clear decrease of flux is not observed in peripheral plasma in ETB phase, which is often observed in H-mode discharges in many devices. In standard configuration in CHS (Rax = 0.921m), LCFS touches the inboard wall of CHS vacuum chamber, that is, limiter configuration. It is considered as the most significant reason why the property of the peripheral plasma with ETB differs from that of H-mode discharges in other devices.

It is very important to focus on fluctuation characteristics before and after the formation of ETB. The significant decrease of density fluctuation was observed just before the onset of the H_α reduction, but it is not observed in ETB phase. It seems to be unique characteristics of the formation of ETB in CHS, and further study is necessary to understand these phenomena.

3-2 MHD burst In CHS, beam driven MHD bursts with mode number of m/n = 3/2 at Rax = 0.974m and m/n = 2/1 at Rax = 0.921m are excited, and loss of high energy particle related to the MHD bursts has been observed by lost ion probe measurement at only Rax = 0.974m [2,3]. The difference of the high energy particle loss between at Rax = 0.974m and Rax = 0.921m is understood by the difference of position of the MHD mode resonance, that is, the resonance position of m/n = 3/2 at Rax = 0.974m exists outside ($\rho \sim 0.8$), while that of m/n

= 2/1 at Rax = 0.921m relatively inside ($\rho \sim 0.6$). Thus the loss of high energy particle is clearly observed at Rax = 0.974m. The response of hybrid probe signal to the MHD burst was also observed at Rax = 0.974m, and it is shown in Fig. 3. At Rax =0.921m, that is not clear, and these results are consistent to those of measurement using the lost ion probe. The synchronized signal with the MHD burst was observed in not only ion current but also electron current of the probe, which implies that the response of the plasma synchronized with the MHD burst excitation is observed by the hybrid probe. The decreases of probe current with excitation of MHD burst were also observed near LCFS, and the spatial dependence of the response to the MHD burst was investigated, which is shown in Fig. 3(b). The plasma expands outward from near LCFS in synchronization with excitation of the MHD burst, that is, the plasma is also lost with MHD bursts at Rax = 0.974m in CHS.

4. Conclusions

The multipurpose probe (hybrid probe) was installed with two-dimensional probe drive in CHS. The changes of peripheral plasma characteristics with ETB formation and MHD bursts have been observed using this probe. The most advantage of this system is ability of spatial scan using two-dimensional probe drive and local measurement of plasma parameters without any line integration. The more detailed measurements in order to understand underlying physics of interesting phenomena and the measurement of heat flux in plasmas are next step of our study.

Acknowledgement

One of the authors (K.N.) would like to thank to Dr. S. Masuzaki for fruitful discussions, and to NBI group for their experimental support. This work is supported in part by a Grant-in-Aid for basic science of the Sumitomo Foundation and also by a Grant-in-Aid for Scientific Research from the Ministry of Education, Science and Culture of Japan.

References

[1] Okamura S. *et al.*, J. Plasma Fusion Res. **79**, (2003) 977-979.

[2] K. Toi, M. Takechi, *et al.*, Nucl. Fusion **39** (1999) 1929.

[3] T. Kondo, M. Isobe, *et al.*, Nucl. Fusion **40** (2000) 1575.

Local and Multi - Chord Neutral Particle Diagnostics of Complex 3D Shaped LHD Plasma

P.R.Goncharov[1], T.Ozaki[1], J.F.Lyon[2], S.Sudo[1], N.Tamura[1], V.Yu.Sergeev[3], D.S.Nikandrov[3], M.Sasao[4], A.Krasilnikov[5], M.Isobe[1], T.Saida[4], TESPEL Group[1] and LHD Experimental Group[1]

1. National Institute for Fusion Science, Toki, Gifu 509-5292, Japan
2. Oak Ridge National Laboratory, Oak Ridge, TN 37831-8072, USA
3. St.Petersburg Polytechnical University, St.Petersburg, 195251, Russia
4. Tohoku University, Sendai, 980-8577, Japan
5. Troitsk Institute for Innovation and Fusion Research, Troitsk, 142092, Russia

1. Introduction. This paper is a brief overview of neutral particle diagnostics on LHD including the multidirectional passive measurements [1, 2] and the active probing with an impurity pellet injection [2, 3]. Neutral particle analysis (NPA) technique is used on LHD for studies of suprathermal ion tail formation from NBI and ICH, fast ion confinement properties, and also for routine T_i measurements. Spatial and angular resolution is required due to the variety of particle orbit classes and complex 3D field geometry of LHD and many of the modern magnetic plasma confinement devices. The correct NPA data interpretation for a toroidally non-axisymmetrical plasma is considered together with the spatial information retrieval from line-integrated naturally occurring neutral flux observed by a scanning milti-chord passive diagnostic. The development of the active local pellet charge exchange (PCX) diagnostic is described with the emphasis on the most feasible particle energy analyzer type from the viewpoint of the high operating speed requirement. The application of the unique Compact Neutral Particle Analyzer (CNPA) [4] is discussed.

2. Passive NPA in an arbitrary magnetic configuration. A general formulation of neutral particle fluxes from non-axisymmetrical plasma has been proposed for an arbitrary shape of isolines in the diagnostic cross-section [5]. All the relevant plasma parameters are assumed to be functions of the magnetic surface. The flux coordinate $\rho(l) = (\Psi/\Psi_{LCMS})^{1/2}$ along the diagnostic sight line calculated by an MHD equilibrium code such as VMEC determines the kernel of the integral expressing the experimentally obtained energy resolved atomic flux $\Gamma(E) = dN/dE\,dt$ [erg^{-1}s^{-1}] via the sought local atomic birth rate $g(E)$ [erg^{-1}cm^{-3}s^{-1}] within the plasma, which is proportional to the local ion distribution function. The atomic flux attenuation due to secondary charge exchange and ion impact ionization is accounted for. The resultant general working equation is as follows:

$$\Gamma(E,\zeta)=e^{\int_{\rho_{\min}}^{1} Q^{-}(\tilde{\rho},\zeta)\lambda_{mfp}^{-1}(E,\tilde{\rho})d\tilde{\rho}}\int_{\rho_{\min}}^{1}\tilde{g}(E,\rho)\times\left[Q^{+}(\rho,\zeta)e^{-\int_{\rho_{\min}}^{\rho} Q^{+}(\tilde{\rho},\zeta)\lambda_{mfp}^{-1}(E,\tilde{\rho})d\tilde{\rho}}-\right.$$
$$\left.-Q^{-}(\rho,\zeta)e^{-\int_{\rho_{\min}}^{\rho} Q^{-}(\tilde{\rho},\zeta)\lambda_{mfp}^{-1}(E,\tilde{\rho})d\tilde{\rho}}\right]d\rho, \qquad (1)$$

where parameter ζ is the vertical plasma scan angle, λ_{mfp} is the mean free path of atoms with respect to ionizing collisions, and $Q^{\pm}(\rho,\zeta)=dl/d\rho$ on the two sight line intervals between the deepest observable point $\rho=\rho_{\min}$ and the LCMS $\rho=1$. The function $\tilde{g}(E,\rho(l))=(\Omega S_a/4\pi)g(E,\rho(l))$ incorporates the geometrical factor depending on the viewing solid angle Ω and the aperture area S_a of the neutral particle analyzer.

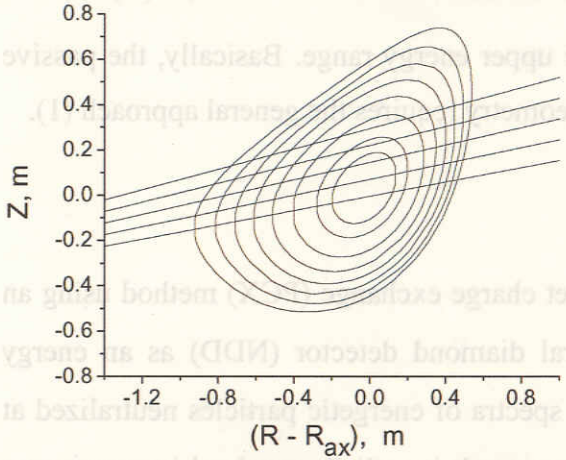

Fig. 1. Magnetic surface structure in one of the vertical cross-sectional planes (#2) and the sight lines at different scan angles (passive NPA).

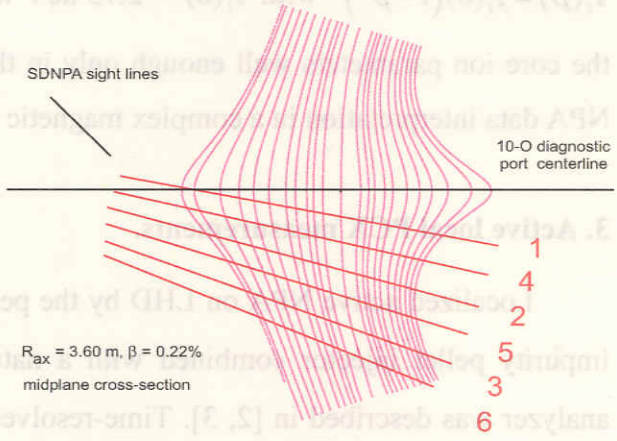

Fig. 2. Horizontal midplane projections of six passive diagnostic sightlines.

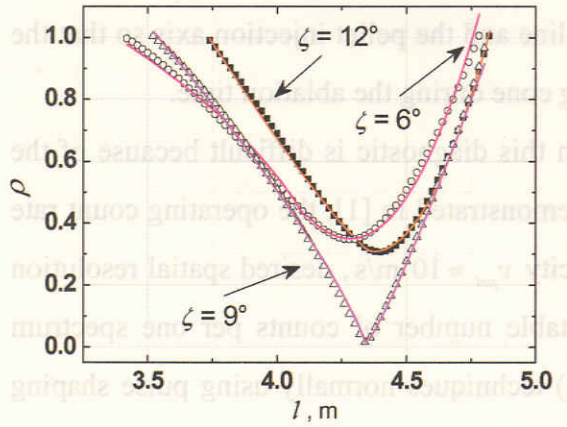

Fig. 3. VMEC data points and uniform polynomial fits $\rho(l)$ (sight line #3).

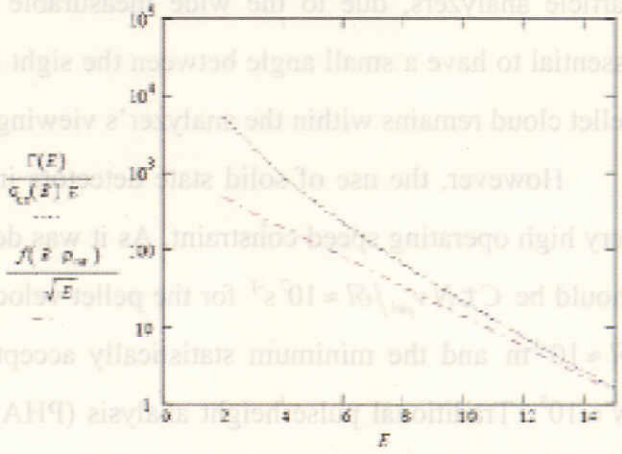

Fig. 4. Measurable (blue) and sought (red) functions of energy numerically simulated for Maxwellian ion distribution function.

Fig. 1 shows an example of the isoline structure in one of the six vertical cross-sectional planes corresponding to the sight lines (Fig. 2) of the multidirectional passive NPA on LHD. The $\rho(l)$ curves obtained from the MHD equilibrium data are shown in Fig. 3 along with uniform minimax polynomial approximations which are more suitable for computations using (1). Possible approaches to the data interpretation based on this formula were discussed in [5], i.e. kinetic modeling and iterative joining of the numerical model and experimental results by variation of unknown free parameters, such as the ion temperature profile. Fig. 4 illustrates the numerically simulated energy dependence of the experimentally observable σE - corrected atomic flux $\Gamma(E)$ and the Maxwellian exponential factor of the model ion distribution function. In this calculation T_i profile in the form $T_i(\rho) = T_i(0)\left(1-\rho^2\right)^2$ with $T_i(0)$ = 2.75 keV was assumed. As it can be seen, $\Gamma(E)$ reflects the core ion parameters well enough only in the upper energy range. Basically, the passive NPA data interpretation in a complex magnetic geometry requires the general approach (1).

3. Active local PCX measurements.

Localized active NPA on LHD by the pellet charge exchange (PCX) method using an impurity pellet injector combined with a natural diamond detector (NDD) as an energy analyzer was described in [2, 3]. Time-resolved spectra of energetic particles neutralized at the pellet ablation cloud moving across the plasma result in radially resolved ion parameter measurements. A solid state detector is an attractive solution, compared to traditional neutral particle analyzers, due to the wide measurable energy range and compactness, which is essential to have a small angle between the sight line and the pellet injection axis so that the pellet cloud remains within the analyzer's viewing cone during the ablation time.

However, the use of solid state detectors in this diagnostic is difficult because of the very high operating speed constraint. As it was demonstrated in [1], the operating count rate should be $C \approx N v_{pel}/\delta l \approx 10^7 \mathrm{s}^{-1}$ for the pellet velocity $v_{pel} \approx 10^3 \mathrm{m/s}$, desired spatial resolution $\delta l \approx 10^{-1} \mathrm{m}$ and the minimum statistically acceptable number of counts per one spectrum $N \approx 10^3$. Traditional pulse height analysis (PHA) techniques normally using pulse shaping amplifiers, peak detecting ADCs and digital histogramming modules cannot provide the operating speed high enough for a good spatial resolution in PCX diagnostics. An alternative approach based on the analysis of digitized preamplifier signals directly without limiting the

overall system throughput by subsequent electronics was discussed in [6]. The signals are treated as a piecewise smooth functions of time due to the fast voltage rise following every incoming particle. The spectra are obtained by regularized detection-estimation of signal increments at discontinuity points proportional to the incoming particles' energies. It was shown that the NDD system may be suitable for the uppermost energies above 100 keV.

For the lower part of the energy range of interest a conventional (i.e. with ion separation) compact (169x302x326 mm) neutral particle analyzer (CNPA) is planned [4]. CNPA is a unique charge exchange spectrometer to be used on LHD for the energies in the range 1 - 170 keV for H_0. A high-field-strength (1 T) NdFeB permanent magnet is employed in this analyzer instead of traditional electromagnets and a thin 100 Å diamond-like carbon stripping foil instead of a gas stripping cell. For PCX measurements CNPA appears to be the most suitable energy analyzer type from the viewpoint of the high operating speed and measurement geometry. Its viewing cone allows to use it simultaneously with NDD, which can be located in the CNPA inlet duct. Thus, the possible measurable energies extend from CNPA upper limit to the MeV range.

An array of channel electron multipliers (CEMs) is used for particle detection. The requirement of a high operating speed necessitates the use of CEMs not only in the counting mode but also in the current mode to be able to work with high fluxes and avoid counting statistics difficulties. This implies the application of special measuring electronics and data acquisition. This analyzer can be used in both ways, i.e. in PCX measurements and also as a passive non-perturbing diagnostic. Comparisons and modeling of complementary measurement results from this diagnostic and the multidirectional passive NPA are planned. CNPA is also planned to be used in a combination with the upgraded cryogenic pellet injection system afterwards. In future experiments this analyzer can also be used for active measurements with a diagnostic neutral beam on LHD.

References

[1] J.F. Lyon, P.R. Goncharov et al., Rev. Sci. Instrum., **74**, 1873 (2003)

[2] P.R. Goncharov, J.F. Lyon et al., J. Plasma Fusion Res. Series, **5**, 159 (2001)

[3] P.R. Goncharov, T. Saida et al., Rev. Sci. Instrum., **74**, 1869 (2003)

[4] F.V. Chernyshev et al., Proc. 30th EPS Conf. on Contr. Fus. and Pl. Phys., *Vol. 27A, P-4.71*

[5] P.R. Goncharov, J.F. Lyon et al., J. Plasma Fusion Res. Series, **6** (2003), to be published.

[6] P.R. Goncharov, T. Ozaki et al., Rev. Sci. Instrum., **76**, to be published.

Magnetic Diagnostics of Non-Rotating Magnetic Island in LHD

Y. Narushima[1], N. Ohyabu[1], S. Sakakibara[1], K.Y. Watanabe[1], T. Yamaguchi[2], H. Yamada[1], K.Narihara[1], I.Yamada[1], T.Morisaki[1], S.Inagaki[1], Y.Nagayama[1], A.Komori[1] and LHD exp. group[1]
W.A.Cooper[3]

[1] *National Institute for Fusion Science, Toki, Gifu 509-5292, Japan*

[2] *Dep. of Fusion Science, Graduate Univ. for Advanced Studies, Toki, Gifu 509-5292, Japan*

[3] *CRPP Association Euratom / Confederartion Suisse, EPFL, 1015 Lausanne, Switzerland*

1.Introduction

Magnetic islands sometimes play key roles in toroidal plasma confinement from the viewpoint of Magneto-Hydro Dynamics (MHD) stability. In Tokamaks, for example, a seed island triggers a neoclassical tearing mode, and its growth leads to serious deterioration of the confinement. On the other hand, it is possible that the island flattens the pressure profile at the resonance surface, contributing to the stabilization of the pressure-driven resonant MHD mode. In the Large Helical Device (LHD), the perturbed field $\tilde{b}_0$ produced by the external perturbed coils [1] can produce a magnetic island in the vacuum field. The seed island grows or reduces without rotation during the plasma discharge. The width, w, of the island is indicated by the flattening of the electron temperature profile measured by Thomson scattering. In LHD the profile only can be obtained at one toroidal position and therefore gives limited knowledge of the structure of the island.

The width w is related to the perturbed field [2]

$$w^2=C(\tilde{b}_0+\tilde{b}_1)/B_t \qquad (1)$$

here C, $\tilde{b}_1$ and B_t are a constant, perturbed field during the plasma discharge and the toroidal field, respectively. For $\tilde{b}_1=0$ and $\tilde{b}_0\neq0$, the width w is equal to that of the vacuum island ($w=w_{vac}$). The magnetic diagnostics measuring the profile of $\tilde{b}_1$ is an effective method to find the structure of the magnetic island.

2.Experimental setup

The toroidal array of magnetic flux loops is set at the outer ports in LHD as shown in Fig.1. Each flux loop has N=10 turns wound at the ports whose cross-sections are around $S\approx1.2m^2$ and have a total cross-section of about $NS=12m^2$,which leads to enough electromotive force voltage to detect the slow (few 100ms) and weak (few Gauss) change of the magnetic field.

The shapes of the flux loops at the toroidal angles $\phi=-162, -54, 54, 90$, and 162 are planar (coloured line in Fig.1) that we use here and the other ones are 3-dimensinal (dotted line in Fig.1). During a plasma discharge these loops can detect the perturbed magnetic flux Φ^R which originates from the growth and reduction of the width of the island. The detected magnetic fluxes Φ^Rs are normalized by the total cross section NS to $\tilde{b}_1$ whose component is in the major radial direction. The 4-pairs of perturbation coils placed at the top and bottom of LHD around $\phi=\pm 90$[deg] (solid line in Fig.1) produce the static perturbation field $\tilde{b}_0$ having an $m/n=1/1$ mode which produces a seed island whose O(X)-point stays at the outer board side at $\phi=90(-90)$[deg] in this study. A Thomson scattering system measures the T_e profile at $\phi=-18$[deg]. The w is estimated as the inner flattening width of the T_e profile as shown in Fig3(a)(c).

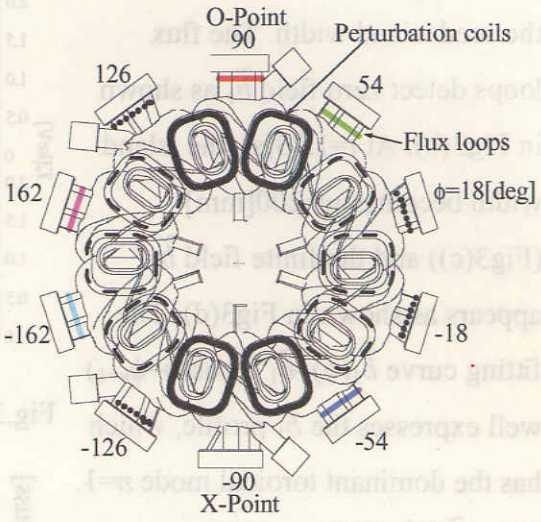

Fig.1 Top view of the vacuum vessel of LHD Toroidal angle ϕ is defined $-180<\phi<180$[deg]

3. Experimental results and discussion

The typical discharge with a seed island ($w_{vac}\approx 150$[mm]) produced by the perturbed field $\tilde{b}_0$ is shown in Fig.2, in which the island width w grows from 150 to 200[mm] as shown in Fig.2(d). The magnetic field $\tilde{b}_1$ varies with time (Fig.2 (e)). Each colour corresponds to that of the flux loops in Fig.1. The $\tilde{b}_1$ at $\phi=-162$ and 162[deg] reduces to $\tilde{b}_1\approx -0.8$[Gauss]. On the other hand, the $\tilde{b}_1$ at $\phi=54$[deg] increases to $\tilde{b}_1\approx 0.8$[Gauss].

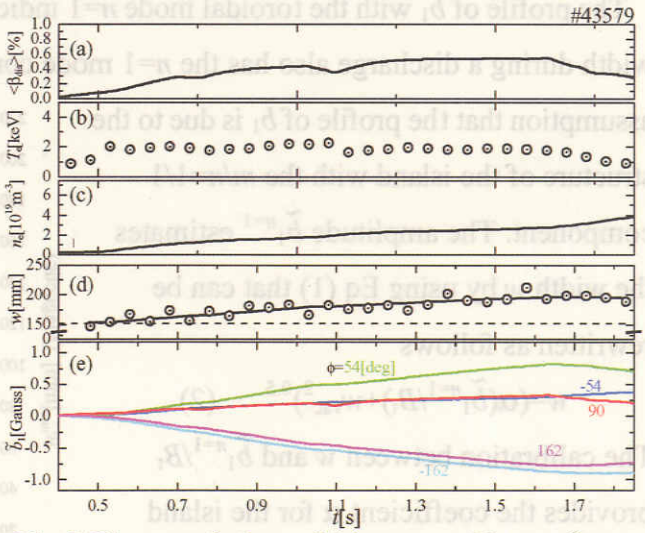

Fig.2 Time evolution of (a)averaged beta $<\beta>_{dia}$ (b)electron temperature at centre T_e (c)averaged electron density n_e (d)island width w (e)perturbed field $\tilde{b}_1$

The T_e and $\tilde{b}_1$ profiles at $t=0.48$ and 1.73[s] are shown in Fig.3. At $t=0.48$[s], Fig3(a) shows that the island width does

not change and is almost same as the seed island width. The flux loops detect zero field $\tilde{b}_1$ as shown in Fig3(b). At t=1.73[s], the island width becomes w=200[mm] (Fig3(c)) and the finite field $\tilde{b}_1$ appears as shown in Fig3(d). The fitting curve $\tilde{b}_1(\phi)=\tilde{b}_1{}^{n=1}\cos(\phi-\phi_{n=1})$ well expresses the $\tilde{b}_1$ profile, which has the dominant toroidal mode n=1. Here, $\tilde{b}_1{}^{n=1}$ and $\phi_{n=1}$ are the maximum amplitude and its toroidal angle respectively. Figure4 shows the time trace of the $\tilde{b}_1{}^{n=1}$ and $\phi_{n=1}$. The amplitude increases from $\tilde{b}_1{}^{n=1}$=0 to 0.9[Gauss] (Fig.4(a)) and the angle does not change from around $\phi_{n=1}$=0 during the plasma discharge(Fig.4(b)). These results mean that the magnetic island width increases with time and does not rotate, and the position of O(X)-point stays at inner (outer) board side at $\phi=-90$[deg].

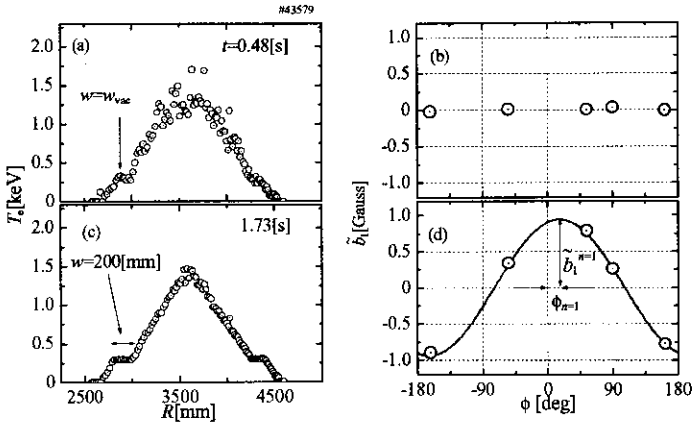

Fig.3 T_e and $\tilde{b}_1$ profile at (a)(b) t=0.48[s], (c)(d) 1.73[s]

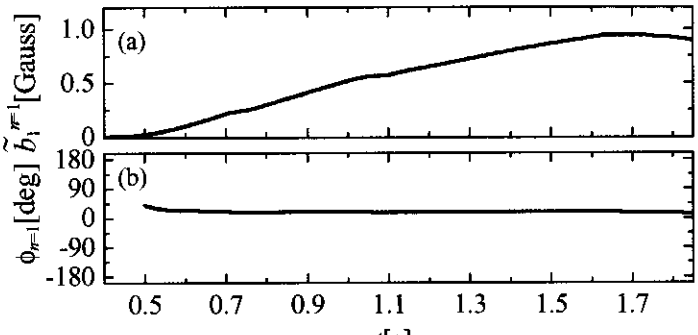

Fig.4 Time trace of (a) $\tilde{b}_1{}^{n=1}$ and (b) $\phi_{n=1}$

The profile of $\tilde{b}_1$ with the toroidal mode n=1 indicates that the change of the magnetic island width during a discharge also has the n=1 mode component. These results depend on the assumption that the profile of $\tilde{b}_1$ is due to the structure of the island with the m/n=1/1 component. The amplitude $\tilde{b}_1{}^{n=1}$ estimates the width w by using Eq (1) that can be rewritten as follows

$$w=(\alpha(\tilde{b}_1{}^{n=1}/B_t)+w_{vac}{}^2)^{0.5} \quad (2)$$

The calibration between w and $\tilde{b}_1{}^{n=1}/B_t$ provides the coefficient α for the island enlargement cases ($w \geqq w_{vac}$). As a result, the magnetic diagnostics can estimate the island

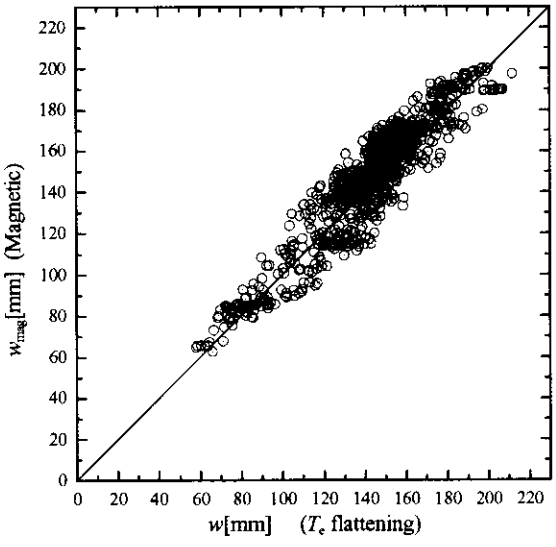

Fig.5 Relationship between w_{mag} and w

width w_{mag}. Figure5 shows the relationship between w and w_{mag}. The solid line in Fig2(d) is the time trace of w_{mag} derived from $\tilde{b}_1$, which can fit the w. These results show that this magnetic loop with large NS can be used to estimate the structure of the non-rotating magnetic island.

For the island reduction or disappearance ($0<w<w_{vac}$, in other words, healing [3,4]), finite $\tilde{b}_1$ can be detected even though a seed island exists. Figure 6 shows the T_e and $\tilde{b}_1$ profiles for the island disappearance case with w_{vac}=114[mm]. The flattening does not appear (Fig6(a)) and finite $\tilde{b}_1^{n=1}$ is indicated and $\phi_{n=1}$ shifts by 180[deg] from the increasing case shown in Fig3(d).

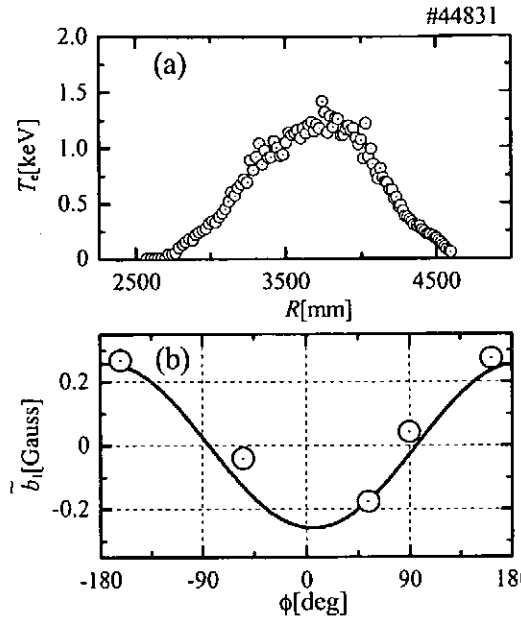

Fig.6 T_e and $\tilde{b}_1$ profile for the island reduction plasma

This result means that some kinds of current layer inside plasma produce $\tilde{b}_1$ that suppresses the seed island in the LHD. We are studying what kind of structure the current layer has.

4. Summary

We carry out the magnetic diagnostics of non-rotational magnetic island in LHD. The finite magnetic field appears with a change of the magnetic island width. Magnetic diagnostics can estimate the structure of an island. Even in the disappearance of a magnetic island, a finite magnetic field appears. Further study is intended to reveal the formation mechanism of the current layer producing $\tilde{b}_1$ which affects the behaviour of the magnetic island.

Acknowledgement

This study was supported by a Grant-in-Aid for Young Scientists (B)(No.15760627) from the Ministry of Education, Culture, Sports, Science and Technology of Japan.

References

[1] T. Morisaki et al., Fusion Engineering and Design. **65**, 475 (2003)

[2] A. H. Boozer, Phys. Fluids **27**, 2055 (1984)

[3] K. Narihara et al., Physical Review Letter **87**, 135002 (2001)

[4] N. Ohyabu et al., Physical Review Letter **88**, 055005 (2002)

Microwave Reflectometer for Density Profile and Fluctuation Measurements on LHD

T. Tokuzawa[1], T. Kaneba[2], K. Kawahata[1], K. Tanaka[1], S. Sakakibara[1], S. Inagaki[1], N. Tamura[1], Y. Nagayama[1] and LHD Experimental Group[1]

[1] *National Institute for Fusion Science, Toki 509-5292, Japan*
[2] *Dep. of Fusion Science, Graduate Univ. for Advanced Studies, Hayama 240-0193, Japan*

1. Introduction

For measuring the density profile and plasma fluctuation in the Large Helical Device (LHD), several types of microwave reflectometer have been installed [1, 2]. Recently we have been developing a new type of reflectometer which is used an ultrashort sub cycle pulse. It is called as an ultrashort pulsed radar reflectometer. An ultrashort pulse has broad band frequency components in a Fourier space. It means one ultrashort pulse can take the place of a broad band microwave source. Also this ultrashort pulsed radar reflectometer is categorized in the type of a time-of-flight (TOF) measurement system. This TOF measurement has an advantage which we can easily distinguish between the ordinary polarized wave and the extraordinary polarized wave involving the reflected wave from the plasma, because each cut-off position in the plasma is separated. Currently this ultrashort pulsed radar reflectometer operates on six channels using a filter bank and a super heterodyne detection system for measuring the edge density profile and slow plasma oscillation. However the measurable frequency range of this ultrashort pulsed radar reflectometer system is lower than about 50 kHz, because the repetition rate of the incident pulse and the memory size of the data acquisition are limited. For higher fluctuation measurement we have been developing the three channel heterodyne fixed frequency reflectometer. This system uses a conventional reflectometer technique and measures the density and magnetic fluctuation in the plasma core region. In this paper we present these two reflectometer systems and obtained some results such as low-n Magnet-Hydro Dynamics (MHD) mode fluctuation.

2. Ultrashort pulsed radar reflectometer

The schematic of ultrashort pulsed radar reflectometer is shown in Fig. 1. An impulse of -2.2 V, 23 ps full-width half-maximum is used as a source. To extract the desired probing

range of the frequency, we utilize an R-band rectangular waveguide. When the impulse is launched into the waveguide, it is transformed to the chirped wave including a broad frequency spectrum that changes from high to low. It is caused by the dispersion effect of the electromagnetic wave in the waveguide. The lowest frequency is determined with the waveguide aperture size. The output chirped wave from the waveguide is amplified by a power amplifier and then is launched into the plasma. The incident wave reflects from the cut off layers corresponding to each frequency component. The reflected wave is mixed with 42 GHz continuous wave of the local oscillator. The output from the mixer is amplified by the intermediate frequency (IF) amplifier (2 – 18 GHz) and then divided to six. Each IF signal is filtered by band pass filters which the centre frequencies are 3, 5, 7, 11, 13 GHz and they correspond to 39, 37, 35, 33, 31, 29 GHz, respectively, in the incident frequency components. Each 3dB band width is 1.0 GHz. The six signals are detected by the Schottky barrier diode detectors to obtain the reflected signal pulses. The reflected pulses are amplified by pulse amplifiers and leaded to constant fraction discriminators (CFD). A part of the incident wave is extracted with a directional coupler and is detected to obtain the reference pulse. Both the reference pulse as the start signal and the reflected pulse as the stop signal are leaded to the time-to-amplitude converter (TAC). The output voltage of TAC is proportional to the time difference between the start and the stop signal. The spatial ambiguity estimated from the TAC output has been tested and defined lower than 6 mm.

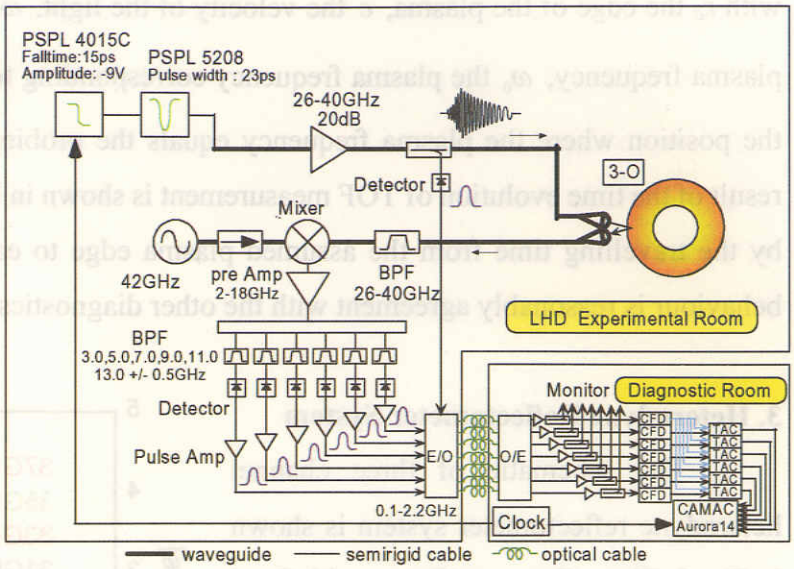

Figure 1 Schematic of ultrashort pulsed radar reflectometer

By using the ordinary wave the measured flight time of each frequency pulse reflected from the plasma has been described by

$$\tau_p(\omega_0)=\left(\frac{\delta\phi(\omega)}{\delta\omega}\right)_{\omega=\omega_0}=\frac{2}{c}\int_{r_a}^{r_c(\omega_0)}\frac{1}{\sqrt{1-\frac{\omega_{pe}^2(x)}{\omega_0^2}}}dx\,,$$

with r_a the edge of the plasma, c the velocity of the light, ω the probing frequency, ω_{pe} the plasma frequency, ω_0 the plasma frequency corresponding to the critical density, and $r_c(\omega_0)$ the position where the plasma frequency equals the probing frequency, respectively. The result of the time evolution of TOF measurement is shown in Fig. 2. The delay time is defined by the travelling time from the assumed plasma edge to each cut off layer. And the TOF behaviour is reasonably agreement with the other diagnostics such as interferometer.

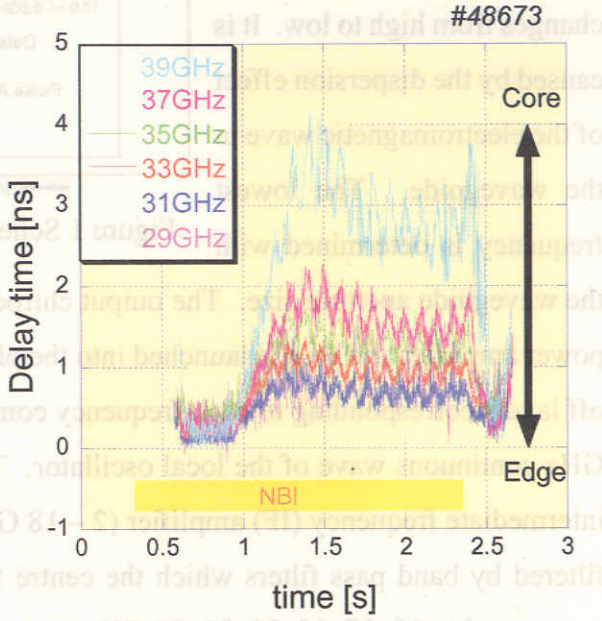

Figure 2 Time evolution of Time-of-flight of six frequency reflected signals

3. Heterodyne Reflectometer System

The schematic of three channel heterodyne reflectometer system is shown in Fig. 3. Three Gunn oscillators with fixed frequencies of 78, 72, 65 GHz are used as sources. Power combined microwaves are travelling to/from the LHD using a corrugated waveguide for avoiding the transmission loss. Receiver system is used the super heterodyne detection technique. By using the extraordinary polarized wave, we can measure the combined fluctuation with the electron density and the magnetic field. In Fig. 4 the temporal behaviour of the reflectometer signal of 78 GHz and its power spectrum are shown. After t=1.45s, the fluctuation appears with the frequency of ~ 1 kHz and its doubler. This mode is identified the m/n=2/1 mode by the magnetic probe analysis. The fluctuation of m/n=2/1 mode is expected to excite in the core region. The reflectometric direct core plasma measurement is utilized to understand the configuration of the fluctuation. Another example of the fast phenomenon in the plasma is shown in Fig. 5. In this shot at $t = t_0$ TESPEL [3] injects into the plasma. Just after TESPEL injection, the electron temperature in the core region rises rapidly in response to the edge cooling. This phenomenon can not be interpreted

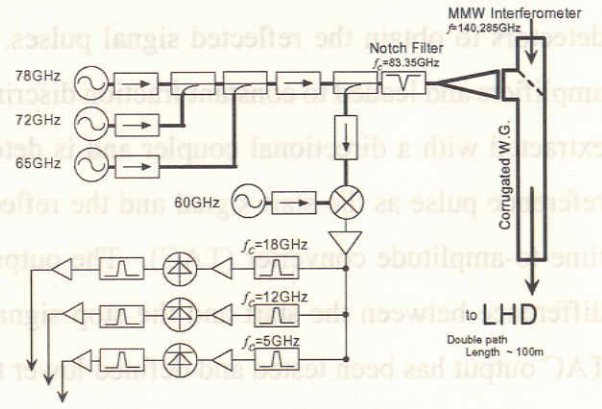

Figure 3 Schematic of three channel fixed frequency CW heterodyne reflectometer

by the conventional transport theory and has not been identified now. At that time in the core region the reduction of the reflectometer signal power is observed. This rapid reduction might trigger the change of the transport. On the other hand in the edge region the decrease is not clear and also low frequency oscillation starts slightly late. The reduction of the reflectometer signal is not caused by the refractive effect in passing. Therefore understanding more detail of this interesting phenomenon, we need to upgrade the reflectometer system and compare with other diagnostics.

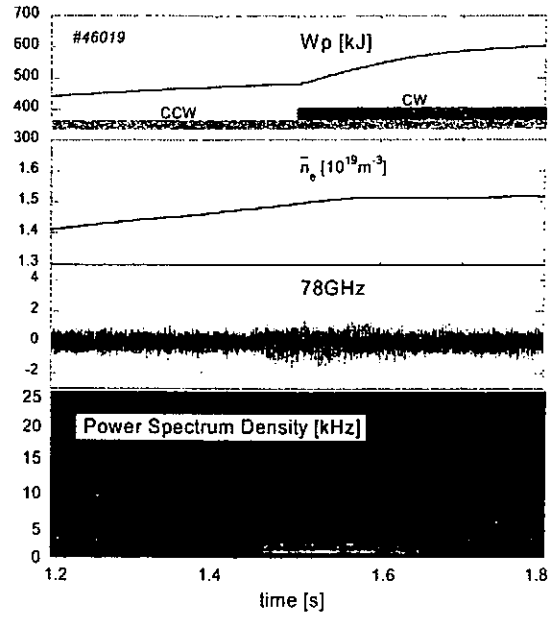

Figure 4 Temporal changes of plasma parameters in low-*n* mode fluctuated discharge

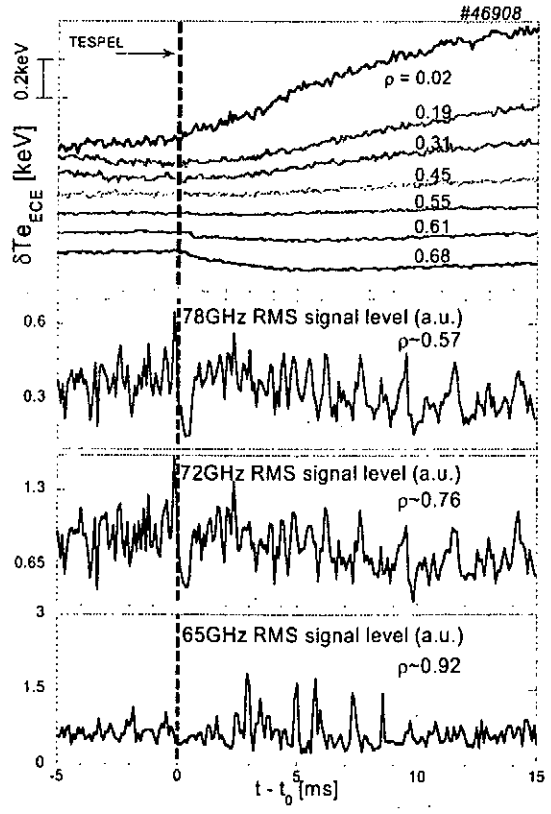

Figure 5 Temporal behaviour of the deference of the electron temperature and each reflectometer signal power

Acknowledgements

This work was partially supported by a Grand-in-Aid for Young Scientists (B) (No.15760625, 2003) from the Japan Society for the Promotion of Science to one of the authors (TT).

References

[1] T. Tokuzawa *et al.*, Rev. Sci. Instrum. **74**, 1506 (2003)

[2] K. Tanaka *et al.*, NIFS-PROC-49, 88 (2001)

[3] S. Sudo *et al.*, Plasma Phys. Control. Fusion **45**, A425 (2003)

Shafranov Shift Measurement Using Soft X-ray CCD Camera on Large Helical Device

T. Kobuchi[1], K. Ida[1], M. Yoshinuma[1], K.Y. Watanabe[1], S. Sakakibara[1], H. Yamada[1], K. Tanaka[1], K. Kawahata[1] and LHD Experimental Group

1. National Institute for Fusion Science, 322-6 Oroshi-Cho, Toki-City, 509-5292 Japan

1. Introduction

High beta operation with good confinement of high energy particles has been a critical issues for helical fusion reactor design. To measure position of the magnetic axis is the most important to determine the beta limit of the plasma. To reduce the magnetic axis shift (Shafranov shift) due to vertical field created by Pfirsch-Schluer currents is useful technique to achieve high beta of plasma. The reduction of the magnetic axis shift can be realized by elongate plasma vertically or driving a current in the direction anti-parallel to equivalent plasma current. Oblate magnetic configuration and neutral beam current drive (NBCD) experiment are carried out to test the usefulness of these techniques.

It is important to investigate the effect of the magnetic axis shift on confinement properties. A net toroidal current affects the MHD stability in heliotron/torsatron configurations. The effect of direction of the net toroidal currents on the local ideal MHD stability or Mercier criterion for plasma in the heliotron/torsatron configuration of the LHD [1] have been investigated by Ichiguchi et al. In this calculation, the toroidal current in the direction opposite to equivalent plasma current is expected to cause the inward magnetic axis shifts in low beta value.

In this paper, the effects of oblate magnetic configuration and net toroidal current on the reduction of magnetic axis shift are investigated. The magnetic axis shifts measured with the soft x-ray CCD camera are compared with those calculated with an equilibrium code.

2. Shafranov shift measurement with soft x-ray CCD camera in LHD

The Large Helical Device (LHD) is a heliotron/torsatron device, which has superconducting coil with polarity $l = 2$ and the toroidal field period $m = 10$ and major radius $R = 3.9$ m and minor radius $a = 0.65$ m [2]. The major radius of vacuum magnetic axis, R_{ax}^{v} and the toroidal averaged ellipticity of cross-section of flux surface, κ, are set by controlling the vertical field and quadrupole field produced by helical coils using the vertical field produced by outer vertical coils and quadrupole field produced by the axisymmetric poloidal coils, respectively. B_Q is the rate which canceled the quadrupole field produced by helical coils in the quadrupole field produced by the axisymmetric poloidal coils at the center of vacuum vessel. When $B_Q = 100$ % at $R_{ax}^{v} = 3.90$m, the average cross-section of flux surface over one field pitch length becomes circular. The magnetic configuration with $\kappa = 1.02$ at $R_{ax}^{v} = 3.60$ m is referred as the 'standard configuration'. The cross-section averaged over one field pitch length becomes vertically (horizontally) elongated when B_Q decreases (increases).

The magnetic axis is derived from the tangential soft x-ray image measured with the soft x-ray CCD camera system in LHD. The soft x-ray CCD detector camera system consists of pinholes, Be filters, shutter and a soft x-ray sensitive CCD detector, which has been installed to the tangential port on LHD to measure the shape of the magnetic flux surfaces [3]. By choosing the appropriate combinations of pinhole size and thickness of Be filters, the x-ray image can be measured for the plasma in a wide range of electron temperature and density.

The position of the magnetic axis, R_{ax}, is derived from the magnetic flux surface in a database, which give the best fit to the two-dimensional x-ray profile measured. The database consists of the magnetic flux surface files about 200 files for one magnetic flux configuration with pressure profile of 4 types,

$(1-\rho^2)^2$, $(1-\rho^8)(1-\rho^2)$, $(1-\rho^8)(1-\rho^4)$, $(1-\rho^8)^2$, volume averaged beta, $<\beta> = 0 \sim 3.7$ % and net toroidal currents from –100 kA/T to 100 kA/T, in LHD, which has been calculated with three-dimensional free boundary equilibrium code, VMEC [4]. The Shafranov shift is the migration length of magnetic axis from vacuum magnetic axis R_{ax}^{v} due to plasma pressure.

The effect of plasma ellipticity on the Shafranov shift is studies in the NBI heated plasma with vacuum magnetic axis $R_{ax}^{v} = 3.60$ m and various quadrupole components; $B_Q =$ 200 % ($\kappa = 0.8$, prolate configuration), $B_Q =$ 100 % ($\kappa = 1.02$, standard configuration) and $B_Q = 0$ % ($\kappa = 1.4$, oblate configuration).

Figure 1 (a) - (f) show the poloidal cross-sections of vacuum flux surfaces calculated with the VMEC code and the tangential images of soft x-ray intensity measured with a soft x-ray CCD camera for the experiment with magnetic configurations of $\kappa = 0.8$, 1.02 and 1.4 at $R_{ax}^{v} = 3.60$ m. The flux surfaces in Fig. 1 (a)-(c) correspond to the cross-sections horizontally and vertically elongated. As shown in Fig 1 (d)-(f), the prolate and oblate images of soft x-ray intensity were measured with a soft x-ray CCD camera.

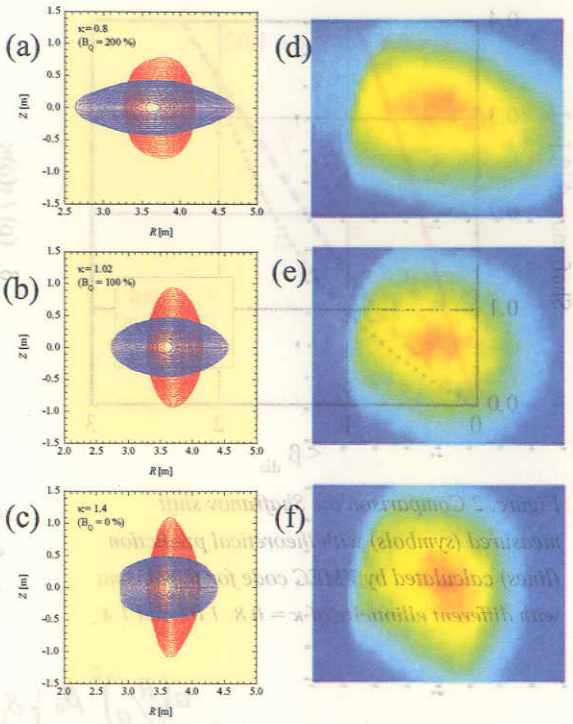

Fig. 1 (a)-(c) cross-sections of vacuum magnetic flux horizontally and vertically elongated calculated with the VMEC Code for the prolate and oblate configurations with k = 0.8, 1.02 and 1.4. (d)-(f) tangential images of soft x-ray intensity measured with the soft x-ray CCD camera for three configurations.

3. The effect of the elongated configurations for Shafranov shift

Figure 2 shows the Shafranov shifts measured with the soft x-ray CCD camera as a function of volume averaged beta estimated with diamagnetic loop, $<\beta_{dia}>$, for plasma with $\kappa = 0.8$, 1.02 and 1.4 at $R_{ax}^{v} = 3.60$ m during NB injection. The figure shows that the Shafranov shifts measured increase linearly as $<\beta_{dia}>$ for all κ, and the shift of magnetic axis in the prolate configuration ($\kappa = 0.8$) is larger than that in the standard configuration ($\kappa = 1.02$) and the shift in oblate configuration ($\kappa = 1.4$) is smaller than that in the standard configuration. The reduction of the Shafranov shift due to the vertical elongation is clearly demonstrated in this experiment.

The Shafranov shifts are calculated from pressure profile using the 3-D equilibrium code, VMEC for three experiments. The electron density and temperature profiles used in this calculation are $n_e \sim n_0(1-\rho^8)$ and $T_e \sim T_0(1-\rho^2)$, that are consistent with measurements with FIR interferometer and YAG Thomson. These magnetic axes are shifted greatly as averaged beta increase. The shift of the magnetic axis for the plasma with the prolate configuration ($\kappa = 0.8$) is much larger than that in oblate configuration ($\kappa = 1.4$) by a factor of 5 at $<\beta_{dia}> = 0.5$ %. Although the Shafranov shift has a difference quantitatively between the measured and calculated results, it is qualitatively in agreement.

The Shafranov shift of magnetic axis due to the Pfirsch-Schluter current for the low β limit can be expressed as

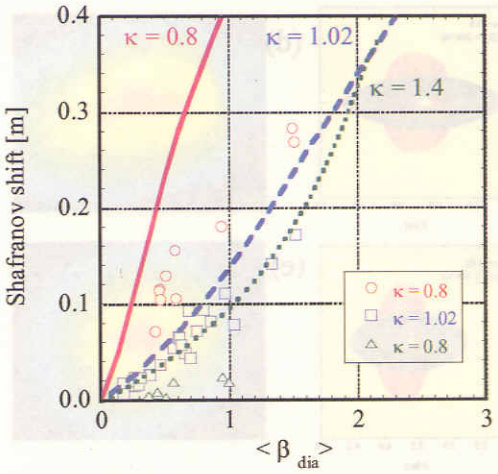

Figure. 2 Comparison the Shafranov shift measured (symbols) with theoretical prediction (lines) calculated by VMEC code for the plasma with different ellipticity of κ = 0.8, 1.02 and 1.4.

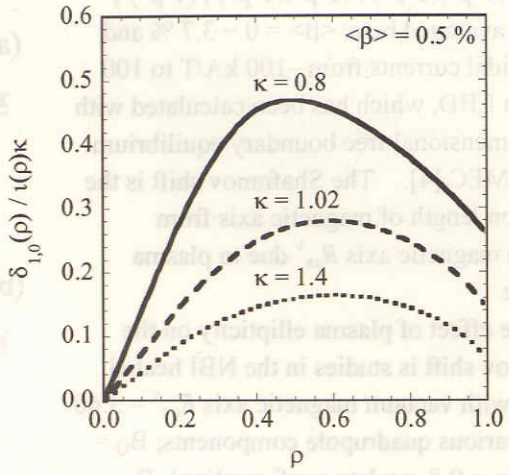

Figure. 3 Radial profiles of $\delta_{1,0}/\kappa\iota$ for plasma with different magnetic elongated configurations, κ=0.8, 1.02 and 1.4.

$$\Delta \cong \frac{a\left(R/a\right)^2 \beta_0}{\iota(1)} \int_0^1 \frac{\delta_{1,0}(\rho)}{\iota(\rho)\kappa} d\rho, \qquad (1)$$

where β_0 is the central β, $\iota(\rho)$ is the rotational transform, and $\delta_{m,n}$ is Fourier component of $1/B^2$ given as

$$\frac{1}{B^2} = \frac{1}{\overline{B}^2}\left(1 + \sum_{m,n} \delta_{m,n}(\rho)\cos(m\theta - n\zeta)\right) \qquad (2)$$

with m (n) and θ (ζ) being the poloidal (toroidal) mode number and angle, respectively [5, 6]. Here ρ is the square root of the normalized toroidal magnetic flux used as the radial co-ordinate. The Pfirsch-Schluter current is generated by (m, n) = (1, 0) component of magnetic field.

Figure 3 shows radial profile of $\delta_{1,0}/\iota\kappa$ for plasma with finite beta, <β> = 0.5 %, and different magnetic configurations of κ = 0.8, 1.02 and 1.4, respectively, in LHD. The value of $\delta_{1,0}$ represent the magnitude of the toroidal effect. As seen in Eq. (1), the Shafranov shift is proportional to the integration of $\delta_{1,0}/\iota\kappa$ and $a(R/a)^2\beta_0/\iota(1)$ changes only few percent in this experiment. The ratio of integration of $\delta_{1,0}/\iota\kappa$ (= S_κ) changes by a factor of three in this experiment; $S_{0.8}/S_{1.02} = 1.7$ and $S_{1.4}/S_{1.02} = 0.59$. The contribution of $\delta_{1,0}/\iota\kappa$ on the magnetic axis shift has been confirmed in the plasma with the prolate and oblate configurations in LHD.

4. The effect of net toroidal current for Shafranov shift

It has been known that, in low beta, current decreasing (increasing) the rotational transform causes the magnetic axis shift to the outward (inward) at the $R_{ax}^{v} = 3.60$ m [7]. In LHD, the vertical field is constant regardless of the toroidal plasma current, apart from the operation in Tokamak. Therefore, the magnetic axis shifts outward (or inward) by hoop force when there is a toroidal plasma current in the co (or counter) direction. Then the toroidal plasma current in the counter direction contributes the reduction of magnetic axis. However, this toroidal plasma current decreases rotational transform and hence increase Shafranov shift. Therefore, the effect of net toroidal current on magnetic axis shift is not straight forward and the direction of magnetic axis shift (inward or outward) depends on current profile and β profile. When the current profile is peaked the increase of Shafranov shift due to lower the rotational transform overcomes the inward shift of magnetic axis due to lower hoop force. In order to investigate

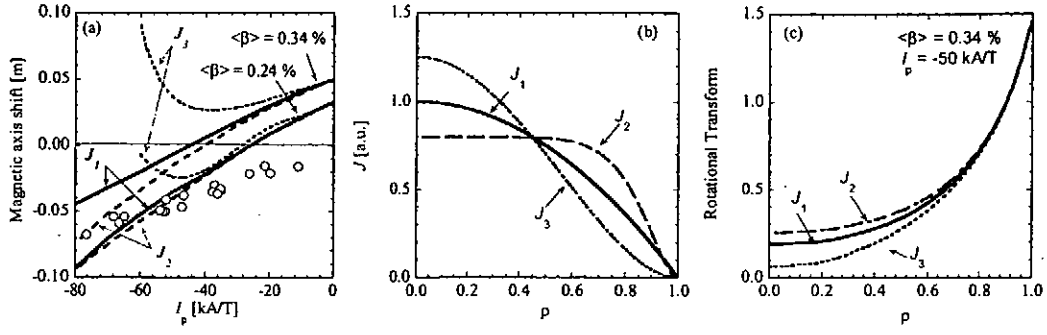

Figure. 4 (a) The shifts of magnetic axis measured by soft x-ray CCD camera (symbols) and calculated with VMEC code (lines) for three type of net current profiles in finite beta as a function of the net toroidal current, (b) net toroidal current profiles using theoretical calculation (c) radial profiles of rotational transform for typical ($J_1 \sim (1-\rho^2)$), broad ($J_2 \sim (1-\rho^8)^2$) and peaked ($J_3 \sim (1-\rho^2)^2$) current profiles with I_p = -50 kA/T in $\langle\beta\rangle$ = 0.34 %.

the effect of toroidal current on magnetic axis shifts, NBCD experiment was carried out with H_2 and neon puff, the vacuum magnetic axis of R_{ax}^{v} = 3.60 m, the toroidal field of B_t = 1.5 T and the magnetic configuration of κ = 1.02. The NB drives net current of -110 kA in the direction to anti-parallel to equilibrium plasma current. The central electron density, $n_e(0)$, measured by FIR interferometer and the stored energy, W_p, estimated by diamagnetic loops increase up to 5×10^{19} m^{-3} and 310 kJ, respectively.

Figure 4 (a) shows the magnetic axis shift measured in this experiment, which is plotted as a function of net toroidal current. Figure shows that the magnetic axis shifts inward from position of the magnetic axis in vacuum magnetic flux surface at R_{ax}^{v} = 3.60 m as the magnitude of toroidal plasma current increase in counter direction. The plasma for this experiment is in the line averaged electron density $\langle n_e \rangle$ range of 0.3-0.8 $\times 10^{19}$ m^{-3} and W_p range of 70-180 kJ.

In order to compare the experimental results with equilibrium calculation, the magnetic axis shifts are calculated with VMEC code in finite beta, $\langle\beta\rangle$ = 0.24 % and 0.34 % for different profiles of toroidal plasma current as seen in Fig. 4 (b). The electron density and temperature profiles used in this calculation are $n_e \sim (1-\rho^8)$ and $T_e \sim (1-\rho^2)$, respectively. In LHD the typical current profile is expected to be $J_1 \sim (1-\rho^2)$ by current diffusion calculation. When the net toroidal current profile is J_1 and J_2 profile, the magnetic axis keep shifting inward as the magnitude of toroidal current is increased. This trend is consistent with the measurements. On the other hand, in J_3 profile, the magnetic axis start to shift outward at large toroidal current in the region $I_p \leqq$ -40 kA/T due to lower the rotational transform as seen in Fig. 4 (c).

The NBCD experiment demonstrates that the magnetic axis shift can be reduced by driving the toroidal plasma current in the direction anti-parallel to equivalent plasma current (counter injection) without increase of the Shafranov shift due to lower the rotational transform.

References

[1] K. Ichiguchi et al. Nucl. Fusion **33** (1993) 481
[2] A Iiyoshi *el al* Fusion Technol. **17** (1990) 169
[3] Y Liang *el al* Rev. Sci. Instrum **72** (2001) 717
[4] S.P. Hirshman, Phys. Fluids **26** (1983) 3553
[5] L.S. Solovev and V.D. Shafranov Rev. Plasma Phys. **5** (1970) 1
[6] M. Yokoyama *et al*, Nucl. Fusion **40** (2000)1909
[7] K. Ichiguchi *et al*, Nucl. Fusion **42** (2002) 557

Analysis of first PCX measurements in LHD

V.Yu. Sergeev, D.S. Nikandrov, P.R. Goncharov[1)], N. Tamura[1)], A. Krasilnikov[2)], O.A. Bakhareva, V.M. Timokhin, D.V. Kalinina[3)], B.V. Kuteev[4)], M. Isobe[3)], T. Ozaki[1)], M. Sasao[5)], S. Sudo[1)] and LHD experimental group

State Polytechnical University, St. Petersburg, Russia e-mail: sergeev@phtf.stu.neva.ru
[1)]National Institute for Fusion Science, Oroshi-cho, Japan
[2)]TRINITI. Troitsk, Moscow region, Russia
[3)]Graduate University for Advanced Studies, Hayama, Japan
[4)]NFI of RRC "Kurchatov Institute", Russia
[5)] Tohoku University, Japan

Introduction. The behavior of fast ions, alphas and ICR-driven minorities is a key problem of the controlled fusion research. Among a few diagnostics capable to measure the energy distribution of the confined fast ions, the Pellet Charge eXchange (PCX) approach using the Neutral Particle Analyzer (NPA) as a detector of helium atoms emitted by pellet clouds has been successfully applied in D-T and ICR-driven minority experiments in TFTR [1]. First results of a new PCX scheme with the Natural Diamond Detector (NDD) have been recently reported in Ref. [2]. In this paper we present and discuss new algorithms developed to derive the energy distribution function from the NDD signal.

Experiment. A tracer-encapsulated solid pellet technique (TESPEL) is widely used nowadays [3,4]. A pellet made of polystyrene polymer (-CH (C_6H_5) CH_2-) with outer shell (typically, 0.7-0.9 mm in diameter) was used to investigate the behavior of fast NBI (E_{NBI} = 150 keV) ions. Being injected in the core direction of plasma heated by 3.4 MW NBI, the pellet makes a dense enough (neutrals and ions of H, C) target responsible for charge exchange between plasma ions and cloud atoms. NDD has been utilized to as an energy analyzer for neutral fluxes emerging the cloud. Details of this experimental set-up were published elsewhere [2].

A calibration of the whole receiving channel of NDD has been done using the ^{241}Am (5.5 MeV) source by placing it into the vacuum vessel. The calibration signal $F_{NDD}(t)$ (Fig. 1a) is lasting a time interval comparable with the total pellet ablation time t_{abl} of about 1 ms. A typical NDD signal for NBI heated LHD shot #37771 together with the pellet ablation light are shown in Fig. 1b and c. Odd negative NDD pulses, especially when pellet ablation is over, will be explained using simulations presented below.

Modeling and discussion. The measured $U_{NDD}(t)$ signal of NDD was simulated as follows

$$U_{NDD}(t) = \sum_{i=1}^{N} A(E_i) F_{NDD}(t - t_i),\ t_i = \sum_{j=1}^{i} \Delta t_i\ , \qquad (1)$$

where $A(?_i)$ is a signal amplitude that is proportional to energy E_i of "i"-particle that arrives to the detector at t_i time, Δt_i is the delay time between arrivals of "i" and "$i+1$"particles, N is the number of measured particles during t_{abl}. In simulations, the energy distribution function

$$f_{NBI} \propto \begin{cases} E^{1/2} / \left(E^{3/2} + E_c^{3/2}\right), for\ E \le E_{NBI} \\ 0 \qquad\qquad\qquad\qquad , otherwise \end{cases} \qquad (2)$$

was used with the critical energy $E_c \cong 45$ keV evaluated according to the simple slowing down model [6]. The Δt_i time depends on the NDD aperture. In the simulations it was assumed to be uniformly distributed within 0.5-2.5 μs time interval. Simulated signals $U_{NDD}(t)$ with an experimental noise added and without it are shown in Fig. 1d,e correspondingly. One can see from Fig. 1c that NDD signal has a 0.2 ms delay relative to the start of pellet ablation. Therefore, it was assumed that fast plasma particles start to expose NDD detector with this delay as well. One can see that the simulations reproduce main features of the experimental signal shown in Fig. 1c. Negative values of signals occur due to the shape of the $F_{NDD}(t)$. We should note that the realized detection scheme had a limitation on the detector load. NDD signal saturated when the detector aperture was increased.

To restore the energy distribution function of fast neutrals from the $U_{NDD}(t)$ time evolution the following algorithm based on Fourier analysis has been developed. One can show that the following V transformation

$$V\left(U_{NDD}\right)\Big|_{\xi = t} = F^{-1}\left(\frac{F\left(U_{NDD}\right)}{F\left(F_{NDD}\right)}\right) \qquad (3)$$

applied to $U_{NDD}(t)$ in form (1) gives the following expression

$$U_{NDD}(t) = \sum_{i=1}^{N} A(E_i) \times \delta[t - t_i] \qquad (4)$$

which is more appropriate for subsequent Pulse Height Analysis (PHA) and derivation of the $f_{PCX}(E)$ energy distribution function of particles measured by NDD. Here, F and F^{-1} are the Fourier and reversed Fourier transforms correspondingly.

The developed algorithm has been tested using the modeled signal with experimental noise shown in Fig. 1d. In Fig. 2a the $f_{NBI}(E)$ ion energy distribution function used for simulation and histogram of the restored $f_{PCX}(E)$ distribution function are shown correspondingly. One can see that the algorithm gives appropriate results for the energies above the noise level.

NDD *principally* operates with the room-temperature noise level so that the experimental noise level was comparable with the maximal energy of plasma particles. Therefore, the following procedure of processing the NDD signal was developed. Briefly, U_{NDD} and F_{NDD} signals were smoothed so that to keep the initial rising part of the $F_{NDD}(t)$ signal with duration of about 0.05 μs. Then, a $S_{NDD}(t')$ initial part of the $F_{NDD}(t)$ signal lasting $\Delta t' = 0.25$ μs was chosen for calculating the following parameter

$$\Delta U_{NDD}(t) = \int_{\Delta t'} \left(U_{NDD}(t) - A(E_i) S_{NDD}(t - t')\right)^2 dt'$$

Here, $A(?_i)$ was varied so that to determine minimums of the ΔU_{NDD}(t) parameter in time. Then, times of minimums and the corresponding $?_i$ values were assumed to be the arrival time t_i of "i"-particle and its energy. The evaluated histogram of the $f_{PCX}(E)$ ion distribution is shown in Fig. 2b together with function (2) calculated for E_{NBI} = 150 keV. The $f_{NPA}(E)$ function measured using the central NPA channel in shot #39970 is shown as well. One can see that the measured function has a lack of fast particles. Maximal energy values of about 40 keV measured by PCX diagnostics is in agreement with data of the LHD passive CX diagnostics.

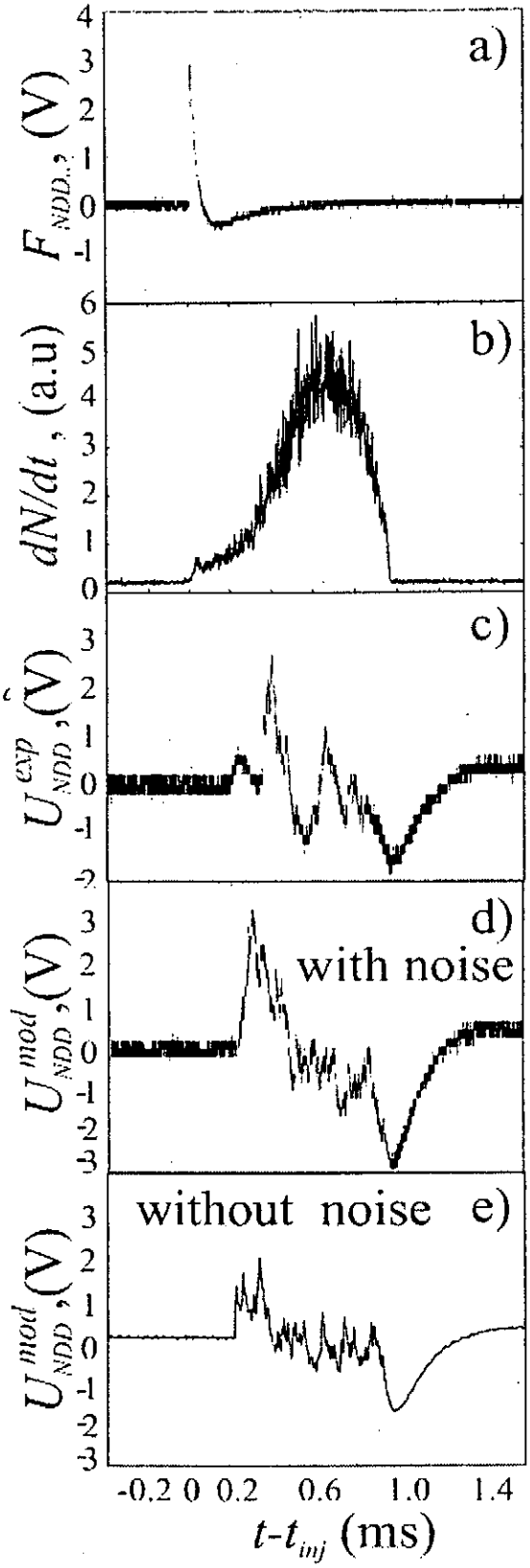

Fig. 1

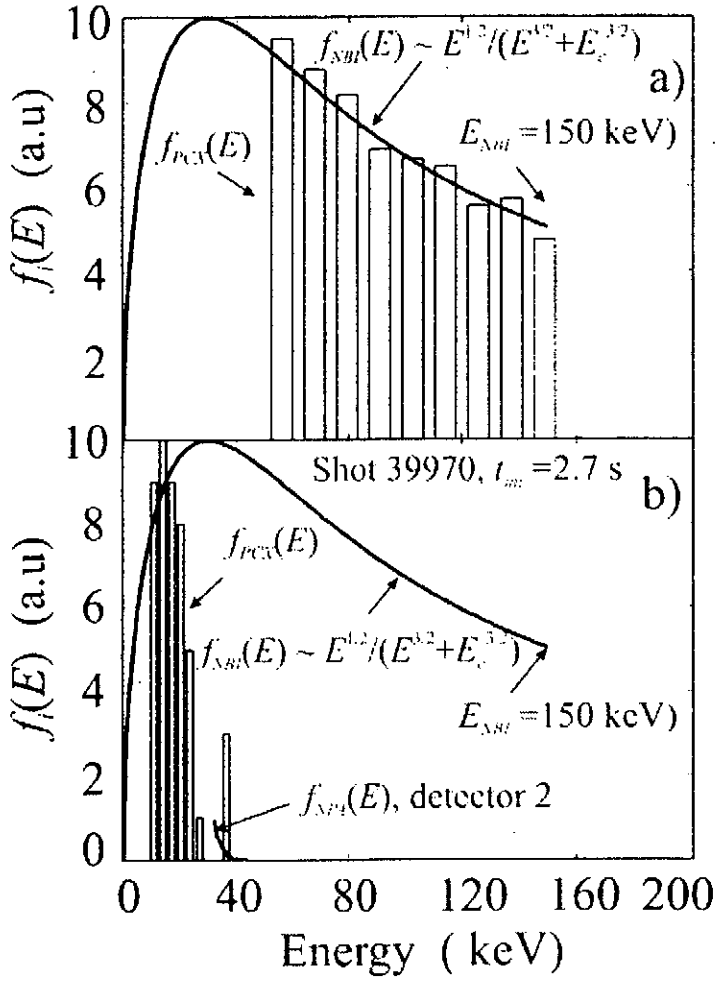

Fig. 2

It is clear from Fig. 2 b that for further studies, the noise level of receiving detector should be reduced to 8-10 keV. For instance, a cooled semiconductor detector and/or cooling the NDD pre-amplifier could be considered. One reason of the lack of detected neutrals was operation with too low detector aperture to exclude a saturation of the NDD signal in the used amplifier scheme. The scheme could be improved by means of the fast switcher that restores a working point of the amplifier within a few microseconds which is much shorter than a pellet ablation time.

Summary. Algorithms for restoring the energy distribution of fast neutrals emerging the pellet cloud in LHD PCX experiments were developed. The maximal neutrals values of about 45 keV measured using PCX diagnostics are in agreement with data of the passive CX diagnostics of LHD. An improvement of the measuring scheme for further studies of fast ions in PHA regimes is offered.

Acknowledgment. Work is supported by RFBR grant 02-02-1755 and RF President's grant NS-2216.2003.2.

References

[1] J.M. McChesney, P.B. Parks, R.K. Fisher *et al.*, Phys. Plasmas **4** (1997) p. 381

[2] P.R. Goncharov *et al.*, Rev. Sci. Instrum **74** (2003) p. 1869

[3] V.Yu. Sergeev *et al.*, Europh. Conf. Abstracts **26?** (2002) P.-2.120

[4] Sudo S. *et al.*, Plasma Phys. Control. Fusion **44** (2002) 129

[5] Tamura N. *et al.*, Plasma Phys. Control. Fusion **45** (2003) 27

[6] Post, D.E. *et al.* Journal of Fusion Energy **1** (1981) p. 1.

Study of fast tangentially beam-injected ion behavior in LHD using natural diamond detectors

A.V.Krasilnikov[2], M.Isobe[1], T.Saida[1], S.Murakami[3], M.Nishiura[1], M.Osakabe[1], M.Sasao[4], K.Toi[1], F.Watanabe[5], V.N.Amosov[2]

[1]*National Institute for Fusion Science, 322-6 Oroshi-cho, Toki 509-5292, Japan*
[2]*Troitsk Institute for Innovating and Fusion Research, Troitsk, Moscow region, Russia*
[3]*Kyoto University, Kyoto, Japan*
[4]*Tohoku University, Sendai, Japan*
[5]*Nagoya University, Nagoya, Japan*

1. Introduction

Due to ripple structure, q profile and topology of fast ions trajectories the issue of fast ion confinement is more crucial in stellarator based fusion reactor. Experiments on LHD [1] with neutral beam injection (NBI) are providing the possibility to study the fast ion behaviour in the largest stellarator plasma. Diagnostic complex of LHD is providing not only the data about spatial distributions of the number of LHD plasma characteristics important for this studies, but in particular the possibility to measure the time evolution of the perpendicular and tangential confined fast ion energy distributions. The purpose of our work was to study the efficiency of confinement of fast tangential and perpendicular ions in relatively MHD-quiescent hydrogen plasma of LHD and under influence of some MHD instabilities.

2. Experimental arrangement

The behavior of fast protons was studied using charge exchange (CX) atom spectrometers based on natural diamond detectors (NDD) viewing tangentially at R=3.65m in equatorial plane and vertically at R=3.67m [2,3]. Fast ions were tangentially co- and counter-injected with energy of 150 keV. To provide both spectrometry and flux dynamic studies of tangential and perpendicular CX atoms, measurements were performed during experimental program with stationary and modulated (200ms–on/200ms–off) co- and counter-injected beam blips [1]. Applied NDDs were developed for fast (E > 25keV) CX atom spectrometry [3]. Tangential NDD placed at distance 6.8m from the plasma center has input window with diameter of 2mm and additional aperture with diameter of 1 mm installed at distance 285mm from it. So this NDD has plane angle of its cone of view ~0.30°, and sees the plasma region with diameter of ~6 cm at the axis. NDD integrates from its cone of view the CX atom flux created by fast ions having pitch angles 140-175° with respect to co-clockwise direction of B_t. Measurements were performed in plasma configurations with magnetic axis at R_{ax} = 3.75, 3.6 and 3.53 m and magnetic fields B_t = 2.5, 1.5, 0.75 (co-clockwise) and -2.5 T.

3. Results fast ion confinement studies

3.1. CX atom spectrum and flux measurements in MHD-quiescent plasma of LHD

To study the difference in confinement of co- and counter-moving tangential and perpendicular ions in a number of LHD plasma configurations the most of CX atom spectra measurements were performed in MHD-quiescent plasmas with similar parameters ($n_e \sim (0.75 \div 1) \times 10^{19}$ m^{-3}, $T_e \sim 1.8 \div 2$ keV).

Another way to study the efficiency of fast ion confinement is connected with fast ($E >$ 25 keV) CX atom flux (figs.1,2) decay time measurements after beam-end in experiments with modulated NBI and their comparison with calculated: 30°scattered times for tangential measurements and slowing down time for perpendicular ones. It could be seen in figs.1,2 that perpendicular CX atom flux exists longer then tangential one. This indicates that tangential NDD measured atom flux from more periphery region than perpendicular one. As shown in fig.2, perpendicular CX atom flux is increasing and time delay of its maximum is diminishing with plasma density (in shown discharge with R_{ax}=3.53m n_e changed from 0.8 to 1.2×10^{19}m^{-3} during time interval 0.85–2.2s). Such relative behavior of tangential and perpendicular fast CX atom fluxes is in good agreement with pitch angle scattering by Coulomb collisions.

In B_t=2.5T experiments the tangential spectra of co-moving CX atoms for R_{ax}=3.53 & 3.6m plasmas and counter-moving atoms for R_{ax}=3.6m plasma were very similar to each other and a bit lower in energy range 20-85keV than also similar co- and counter-moving atom spectra for R_{ax}=3.75m plasmas. This shows the absence of difference in confinement of co- and counter moving ions with energies up to 140keV in these LHD plasma configurations. Measured decay times of co- and counter-moving CX atom flux were higher in R_{ax}= 3.75m plasma than in R_{ax}=3.6 or 3.53m (fig.3) ones. These results could be treated as illustration of slightly better orbit confinement of measured by NDD both co- and counter- moving fast ions in the case of R_{ax}=3.75m (when NBI deposition is more central and NDD sees plasma closer to the axis) than in R_{ax}=3.6 and 3.53m. Very low values of measured co-moving CX atom flux decay times in R_{ax}=3.53m plasma configuration could be partly explained by CX loss.

Tangential counter-moving CX atom spectra (fig.4) are slightly diminishing with B_t change from 2.5 T to 1.5 T and essentially diminishing for B_t = 0.75 T in plasmas with Rax = 3.6 m. The measured fast CX atom flux decay times (see fig.5) in these experiments were slightly (B_t = 1.5 T) or essentially (B_t = 0.75 T) shorter than calculated 30° scattering time. These spectrometry and decay time data could be treated as illustration of some degradation of the confinement of counter-moving ions in plasma with diminished B_t, especially at B_t = 0.75

T. Measured results could be also assigned lower T_e at lower B_t and to wider fast ion trajectory excursions to plasma periphery and so lower slowing down time and higher CX loss there.

Perpendicular CX atom spectra, $T_{eff,\perp}$ and fast CX atom flux decay time (see fig.6 & 7) were lower in R_{ax}=3.75 m configuration than in R_{ax}=3.6 and 3.53 m. All this illustrates better confinement of helically trapped ions in inward shifted configurations than in R_{ax}=3.75m one.

3.2. CX atom flux measurements in LHD plasma with MHD activity.

Sharp increases of co-moving CX atom fluxes were measured in experiments with 200ms co-beam blip injection in R_{ax}=3.53m and not so clear but also in R_{ax}=3.6 m plasma configuration during the second part of the beam time (see fig.1). Essential MHD activity was developed in these experiments with inward shifted LHD plasma and modulated co-NBI. Development of MHD activity in LHD discharge with R_{ax} =3.53 m, which CX atom fluxes presented in figs. 1 and 2 is shown in fig.8. Measured sharp increases of CX atom fluxes correlate with appearance in plasma 50-60 kHz MHD instabilities. This effect was almost not seen in R_{ax}=3.75m plasma configuration. Instant beginning of co-CX atom flux decay after co-NBI termination and delay with decay of counter-CX atom flux after counter-NBI termination were also measured. Increase of co-moving ion transport from plasma center to periphery by 50-60 kHz energetic particle modes in R_{ax}=3.53 and 3.6 m plasma configurations could be discussed as the reason for measured increase of fast CX atom flux.

[1] M.Osakabe, *et. al.* 20th IAEA Fusion Energy conference paper. Vilamoura, Portugal
[2] M.Isobe, *et.al.*, Rev. Sci. Instrum., **72**, 611 (2001).
[3] A.V.Krasilnikov, *et.al.*, Nuclear Fusion, **42**, 759-767 (2002).

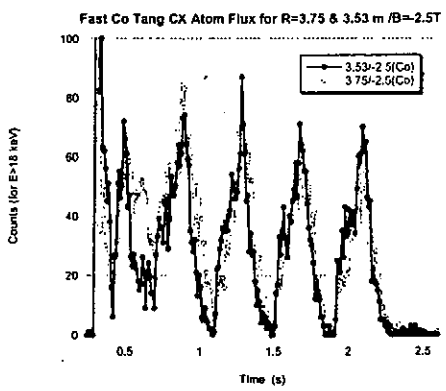

Fig.1 Tang. co-CX atom flux during 200ms beam blips turned-off at 0.9, 1.3, 1.7, 2.1 s.

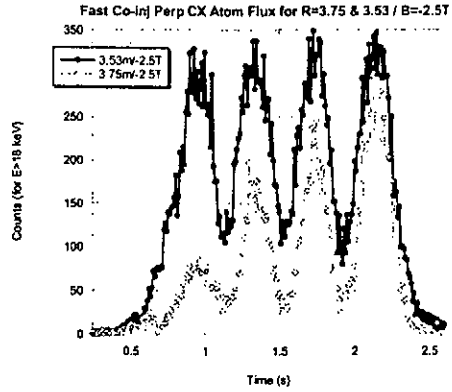

Fig.2. Perp. CX atom flux during 200ms beam blips turned-off at 0.9, 1.3, 1.7, 2.1 s.

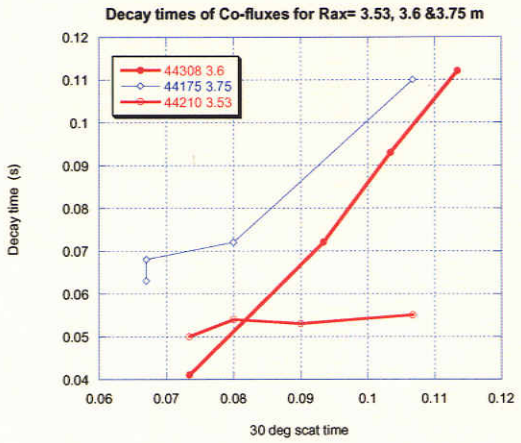

Fig.3.Co-CX atom fluxes decay times upon R_{ax}.

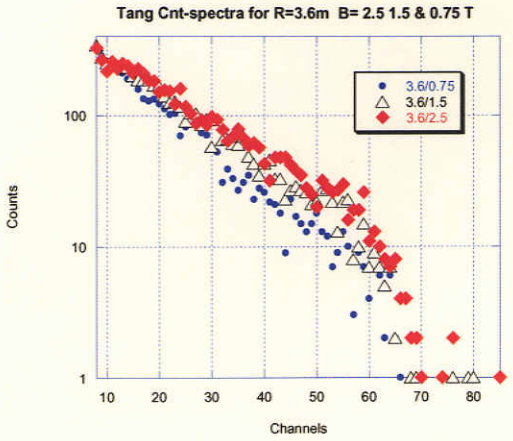

Fig.4.Cnt-CX atom spectra at different B_t.

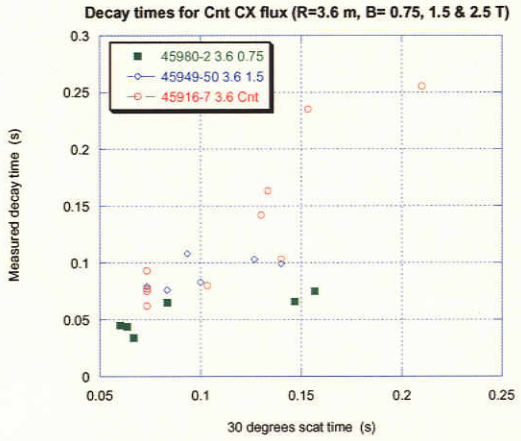

Fig.5.Cnt-CX atom flux decay time upon B_t.

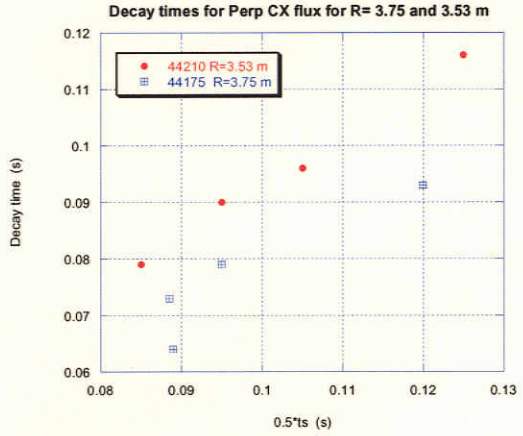

Fig.6.Perp.CX atom flux decay time upon R_{ax}.

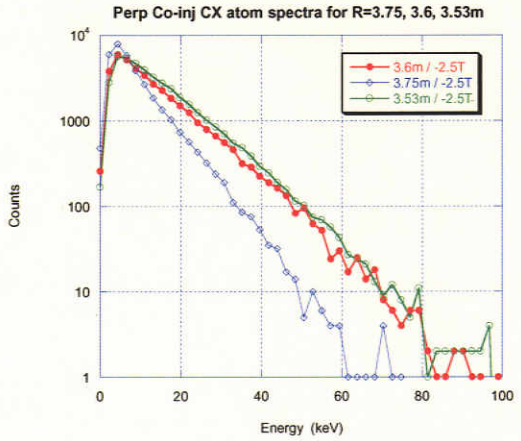

Fig.7. Perp.CX atom spectra at different R_{ax}.

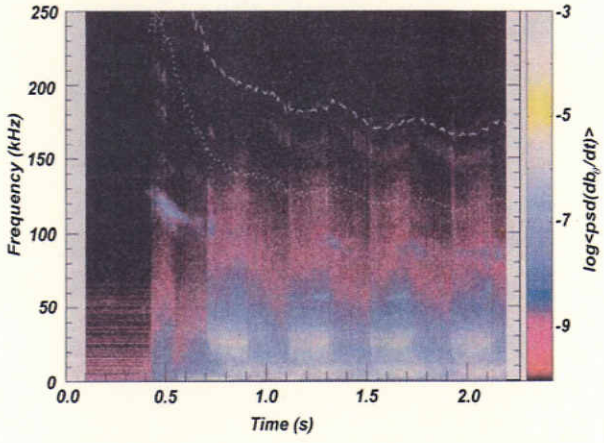

Fig.8. MHD activity during co-beam blips.

Recent Issues of NIFS Series

NIFS-779 Oleg I. Tolstikhin and C. Namba
CTBC A Program to Solve the Collinear Three-Body Coulomb Problem: Bound States and Scattering Below the Three-Body Disintegration Threshold
Aug. 2003

NIFS-780 Contributions to 30th European Physical Society Conference on Controlled Fusion and Plasma Physics (St.Petersburg, Russia, 7-11 July 2003) from NIFS
Aug. 2003

NIFS-781 Ya. I. Kolesnichenko, K. Yamazaki, S. Yamamoto, V.V. Lutsenko, N. Nakajima, Y. Narushima, K. Toi, Yu. V. Yakovenko
Interplay of Energetic Ions and Alfvén Modes in Helical Plasmas
Aug. 2003

NIFS-782 S.-I. Itoh, K. Itoh and M. Yagi
Turbulence Trigger for Neoclassical Tearing Modes in Tokamaks
Sep. 2003

NIFS-783 F. Spineanu, M. Vlad, K. Itoh, H. Sanuki and S.-I. Itoh
Pole Dynamics for the Flierl-Petviashvili Equation and Zonal Flow
Sep. 2003

NIFS-784 R. Smirnov, Y. Tomita, T. Takizuka, A. Takayama, Yu. Chutov
Particle Simulation Study of Dust Particle Dynamics in Sheaths
Oct. 2003

NIFS-785 T.-H. Watanabe and H. Sugama
Kinetic Simulation of Steady States of Ion Temperature Gradient Driven Turbulence with Weak Collisionality
Nov. 2003

NIFS-786 K. Itoh, K. Hallatschek, S. Toda, H. Sanuki and S.-I. Itoh
Coherent Structure of Zonal Flow and Nonlinear Saturation
Dec. 2003

NIFS-787 S.I. Itoh, K. Itoh, M. Yagi and S. Toda
Statistical Theory for Transition and Long-time Sustainment of Improved Confinement State
Dec. 2003

NIFS-788 A. Yoshizawa, S.-I. Itoh, K. Itoh and N. Yokoi
Dynamos and MHD Theory of Turbulence Suppression
Dec. 2003

NIFS-789 V.D. Pustovitov
Pressure-induced Shift of the Plasma in a Helical System with Ideally Conducting Wall
Jan. 2004

NIFS-790 S. Koikari
Rooted Tree Analysis of Runge-Kutta Methods with Exact Treatment of Linear Terms
Jan. 2004

NIFS-791 T. Takahashi, K. Inoue, N. Iwasawa, T. Ishizuka and Y. Kondoh
Losses of Neutral Beam Injected Fast Ions Due to Adiabaticity Breaking Processes in a Field-Reversed Configuration
Feb. 2004

NIFS-792 T.-H. Watanabe and H. Sugama
Vlasov and Drift Kinetic Simulation Methods Based on the Symplectic Integrator
Feb. 2004

NIFS-793 H. Sugama and T.-H. Watanabe
Electromagnetic Microinstabilities in Helical Systems
Feb. 2004

NIFS-794 S.I. Kononenko, O.V.Kalantaryan, V.I. Muratov and C. Namba
Spectral and Angular Characteristics of Fast Proton-Induced Luminescence of Quartz
Mar. 2004

NIFS-795 K. Itoh, K. Hallatschek and S.-I. Itoh
Excitation of Geodesic Acoustic Mode in Toroidal Plasmas
Mar. 2004

NIFS-796 A. Shimizu, A. Fujisawa, S. Ohshima and H. Nakano
Consideration of Magnetic Field Fluctuation Measurements in a Torus Plasma with Heavy Ion Beam Probe
Mar. 2004

NIFS-797 M.I. Mikhailov, K. Yamazaki
Fast Particles Confinement in Stellarators with Both Poloidal-Pseudo-Symmetry and Quasi-Isodynamicity
Apr. 2004

NIFS-798 T. Takahashi, T. Kato, N. Iwasawa and Y. Kondoh
Power Deposition by Neutral Beam Injected Fast Ions in Field-Reversed Configurations
Apr. 2004

NIFS-799 V.S. Voitsenya, D.I. Naidenkova, Y. Kubota, S. Masuzaki, A. Sagara, K. Yamazaki
On the Possibility to Increase Efficiency of Conditioning of Vacuum Surfaces by Using a Discharge in a Hydrogen-noble Gas Mixture
Apr. 2004

NIFS-800 S.-I. Itoh, K. Itoh, A. Yoshizawa and N. Yokoi
Periodic Change of Solar Differential Rotation
May 2004

NIFS-801 V.S. Voitsenya, A. Sagara, A.I. Belyaeva
Effect of Exposure inside the LHD Vessel on Optical Properties of Stainless Steel Mirrors
Jun 2004

NIFS-802 T.J. Dolan and K. Yamazaki
Upgrade and Benchmarking of the NIFS Physics-Engineering-Cost Code
July 2004

NIFS-803 Contributions to 31st European Physical Society Conference on Plasma Physics (London, UK, 28 June to 2 July, 2004) from NIFS
Aug. 2004